ENERGY APPROACH TO THE FAILURE OF CONCRETE AND CONCRETE MEMBERS(Dissertation_全文)

AUTHOR(S):

Rokugo, Keitetsu

ENERGY APPROACH TO THE FAILURE OF CONCRETE AND CONCRETE MEMBERS

November 1979

KEITETSU ROKUGO

ENERGY APPROACH TO THE FAILURE OF CONCRETE AND CONCRETE MEMBERS

November 1979

KEITETSU ROKUGO

ACKNOWLEDGMENT

This thesis consists of four investigations. The investigations in Chapters 2, 4, and 5 were performed at Kyoto University under the direction of Kiyoshi Okada, Professor of Civil Engineering at Kyoto University, and Wataru Koyanagi, Professor of Civil Engineering at Gifu University. The investigation in Chapter 3 was carried out at the University of Illinois at Urbana-Champaign under the direction of Clyde E. Kesler, Professor of Civil Engineering, and Theoretical and Applied Mechanics, and Frederick V. Lawrence, Professor of Civil Engineering and Metallurgy. The author wishes to thank them for their valuable guidance and discussions throughout the investigation.

The author is indebted to Kazuo Kobayashi, Assistant Professor of Civil Engineering at Kyoto University, who offered helpful advice, and whose gracious allowance of time enabled me to write this thesis. Thanks are also due to Kiyoshi Yamura, Assistant Professor of Civil Engineering at Tottori University, and to Toyoaki Miyagawa, Assistant at Kyoto University, for their discussions and experimental assistance. A debt of gratitude is expressed to Masayasu Otsu, Assistant at Kyoto University, and to Mr. Keiji Omori for the detection of acoustic emissions. Thanks are also due to Toshihide Toyofuku, Assistant at Kagawa University, Mr. Muhammad A. Azimi, Mr. Kenji Otani, and Mr. Shiro Fujii for their help in experiments.

The assistance in the investigation in Chapter 3 by Mr. John L. Carrato and Mr. Robert C. Andren at the University of Illinois is appreciated.

Finally, the author wishes to thank his wife, Akemi, for her typing and encouragement.

TABLE OF CONTENTS

CHAPTER		Page
1.	INTRODUCTION	1
	1.1 General	1
	1.2 Studies on Fracture of Concrete	3
	1.3 Scope	16
2.	FRACTURE PROCESS OF CONCRETE IN FLEXURE	21
	2.1 Introduction	21
	2.2 Experimental Procedures	22
	2.3 Load-Displacement Diagram	26
	2.4 Energy-Displacement Relationship	28
	2.5 Fracture Process Under Flexure and Under Compression	29
	2.6 Dissipated Energy and Crack Growth	31
	2.7 Detection of Cracking with Acoustic Emission	32
	2.8 Conclusion	35
3.	EVALUATION OF FRACTURE TOUGHNESS PARAMETERS OF CONCRETE	57
	3.1 Introduction	57
	3.2 Experimental Procedures	59
	3.3 Test Results and Scatter	64
	3.4 Load-Displacement Diagram	67
	3.5 Best Technique for Evaluating J_c	69
	3.6 Other Fracture Toughness Parameters	71
	3.7 Conclusion	73
4.	FRACTURE PROCESS OF CONCRETE IN COMPRESSION	103
	4.1 Introduction	103
	4.2 Experimental Procedures	103
	4.3 Energy-Displacement Relationship	106
	4.4 Effect of Concrete Qualities	107
	4.5 Effect of Loading Rate	108
	4.6 Effect of Moisture Content	108
	4.7 Effect of Specimen Size	110
	4.8 Conclusion	112
5.	FLEXURAL FAILURE PROCESS OF REINFORCED CONCRETE BEAMS	129

5.1 Introduction ---------- 129
5.2 Experimental Procedures ---------- 130
5.3 Load-Displacement Diagram of RC Beams ---- 134
5.4 Deformation and Energy Dissipation in Concrete and Reinforcement ---------- 137
5.5 Neutral Axis and Curvature ---------- 141
5.6 Acoustic Emissions in RC Beams ---------- 144
5.7 Plastic Rotation Capacity ---------- 145
5.8 Conclusion ---------- 148

6. CONCLUSION ---------- 171

LIST OF REFERENCES

LIST OF SYMBOLS

a = crack depth or notch depth. Chapters 1 and 3

A_n = area representing W_n on load-displacement diagram. Chapter 3

A_t = total area representing W_t on load-displacement diagram. Chapter 3

A_u = $A_t - A_n$. Chapter 3

b = length of unnotched ligament. Chapter 3

B = specimen width. Chapters 1 and 3

$2c$ = crack length in infinite plate. Chapter 1

$\bar{c}$ = path of integration taken counterclockwise around crack tip. Chapter 1

d = effective depth of RC beam. Chapter 5

D = load-point displacement, that is, deflection for beam specimens and deformation for cylindrical specimens. Chapters 2, 3, 4, and 5

D_c = center-point displacement, 6 mm from center line of beam specimens. Chapter 3

D_{cc} = center-point displacement, at center line. Chapter 3

D_{cp} = D_c at peak load. Chapter 3

D_f = load-point displacement at rupture. Chapter 3

D_{m1} = predetermined displacement in virgin load-displacement diagram of cylindrical specimen in comprssion. Chapter 4

D_{m2} = D_{m1} + 0.04 mm. Chapter 4

D_n = load-point displacement component due to notch or crack. Chapter 3

D_p = load-point displacement at peak load. Chapters 2, 3, 4, and 5

D_{si} = plastic deformation in reinforcing bar. Chapter 5

D_u = load-point displacement component due to unnotched portion of beam. Chapter 3

D_1 = load-point displacement component due to rotation in shear spans, L_1, in RC beam. Chapter 5

D_2 = load-point displacement component due to rotation in moment span, L_2, in RC beam. Chapter 5

e_v = volumetric strain of cylindrical specimen (= e_1 + $2e_2$). Chapter 1

e_1 = lateral strain. Chapter 1

e_2 = longitudinal strain. Chapter 1

E = modulus of elasticity. Chapters 1, 3, and 5

EI = flexural stiffness. Chapter 5

f = uniform tensile stress. Chapter 1

f_c = compressive strength of concrete. Chapters 2, 3, 4, and 5

f_m = critical tensile stress. Chapter 3

f_{su} = tensile strength of reinforcing bar. Chapter 5

f_{sy} = yield strength of reinforcing bar. Chapter 5

F = stress intensity coefficient. Chapters 1 and 3

G = energy release rate,or crack driving force. Chapter 1

G_c = critical energy release rate, or crack resistance force. Chapters 1 and 3

H = specimen height or depth. Chapters 2, 3, and 4

I = moment of inertia of section. Chapter 5

J = J-integral. Chapters 1 and 3

J_c = critical J evaluated at peak load. Chapters 1 and 3

J_{cb} = J_c evaluated by method proposed by Begley and Landes. Chapter 3

J_{cr} = J_c evaluated by method proposed by Rice, Paris and Merkle. Chapter 3

K = stress intensity factor. Chapters 1 and 3

K_c = critical stress intensity factor. Chapters 1 and 3

L = span length. Chapters 1 and 3

M = moment. Chapters 1, 3, and 5

M_p = peak moment. Chapters 1 and 5

M_y = yield moment of RC beam. Chapter 5

M_{yc} = calculated M_y. Chapter 5

M_{ym} = measured M_y. Chapter 5

p = reinforcement ratio. Chapter 5

P = load. Chapters 2, 3, 4, and 5

P_p = peak load. Chapters 2, 3, 4, and 5

P_{max} = maximum load (corresponds to D_{ml}) for repeated loading and sustained loading. Chapter 4

P_{sy} = yield load of reinforcing bar in tension. Chapter 5

P_y = yield load of RC beam in flexure. Chapter 5

(r, α) = polar coordinates. Chapter 1

s = arc length along path. Chapter 1

S = nominal unit dissipated energy. Chapters 1 and 3

T = arrival time difference of AE waves. Chapter 2

$\tilde{T}$ = traction vector defined by outward normal vector along path. Chapter 1

$\tilde{u}$ = displacement vector. Chapter 1

V = propagation velocity of AE wave. Chapter 2

w = strain energy density. Chapter 1

W = energy. Chapters 1, 2, 3, 4, and 5

W_a = elastic strain energy release due to crack. Chapter 1

W_i = irreversible dissipated energy. Chapters 2, 4, and 5

W_{ic} = energy dissipated in concrete. Chapter 5

W_{icr} = energy dissipated by crack formation. Chapter 4

W_{ifr} = energy dissipated by viscous friction. Chapter 4

W_{ip} = W_i at peak load. Chapters 2 and 4

W_{is} = energy dissipated in steel reinforcing bar. Chapter 5

W_{il} = W_i at first loading repetition. Chapter 4

W_n = component of potential energy due to presence of crack or notch. Chapters 1 and 3

W_o = elastic energy of uncracked plate. Chapter 1

W_r = reversible strain energy. Chapters 2, 3, and 5

W_{rp} = W_r at peak load. Chapters 2 and 4

W_s = surface energy exerted by formation of new crack surfaces. Chapter 1

W_t = total potential energy, or work done of the system. Chapters 1, 2, 3, 4, and 5

W_{tf} = W_t at rupture. Chapter 3

W_{tp} = W_t at peak load. Chapters 2, 3, and 4

(X,Y,Z) = rectangular coordinates. Chapters 1 and 2

γ = unit surface energy. Chpater 1

γ_p = unit energy dissipated in plastic work. Chapter 1

θ_n = rotation due to notch or crack. Chapters 1 and 3

θ_p = plastic rotation of RC beam (= $\Phi_p \cdot d$). Chapter 5

ν = Poisson's ratio, = 0.18 for concrete. Chapter 3

τ_{xy} = stress component in vicinity of crack tip. Chapter 1

ϕ = diameter. Chapters 2, 3, 4, and 5

Φ = averaged curvature in moment span. Chapters 3 and 5

Φ_p = plastic curvature of RC beam. Chapter 5

Φ_{pc} = calculated plastic curvature. Chapter 5

Φ_{pm} = measured plastic curvature. Chapter 5

CHAPTER 1. INTRODUCTION

1.1 GENERAL

One of the main purposes of the design of structures is to defend human life and wealth from the failure of structures. For this purpose, both the magnitude of external loads acting on the structure and the strength of the structure should be known exactly or at least statistically. Moreover, in order to control sufficiently the failure phenomena of the structure, we should know not only the strength of the structure but also the failure manner, the failure location in the structure, etc.

Concrete structures generally consist of members such as beams, columns, slabs, walls, etc. Each member is made from smaller elements such as concrete and reinforcement. Moreover, concrete consists of aggregates and cementitious matrix.

In general, to theoretically explain physical phenomena, they should be considered from a view point which is one level smaller than the phenomena. Therefore, to understand the macroscopic failure phenomena of concrete, which are usually recorded in the load-displacement relations, they should be related to the phenomena in the smaller elements. In the case of members such as beams and columns, the failure of the member should be related to the failure behavior of the elements, namely, concrete and reinforcement.

Concrete is a multi-phase material, in which aggregates are bonded by a hydrated cement matrix. The fracture of concrete has been studied from microscopic view point, but in spite of these research efforts, the fracture of concrete has not been sufficiently explained. The elastic modulus of aggregates is very different from that of the matrix, and the shape of aggregates is very complicated. Therefore, even if

stress is macroscopically uniform, the microscopic distributions of stresses and strains are far from uniform, as shown by Dantu [1]. Moreover, when cracks occur in the concrete structure, the system becomes discontinuous. In such a case, it is quite difficult to discuss the fracture of concrete in terms of microscopic stress and strain. For the above reasons, the approach in terms of energy, which is calculated from the macroscopically averaged stresses and strains or from the measured loads and displacements, is considered to be very efficient to describe the fracture of concrete.

As an example, let us consider a concrete specimen which is subjected to a load. One portion of the work done to the specimen would be stored as strain energy in the specimen, and the other portion would be dissipated within the specimen. Hereafter, the latter is designated as the dissipated energy. The fracture in the specimen may be directly related to the dissipated energy. Therefore, new knowledge could be obtained by quantitatively investigating the energy transfer process during the fracture process of the specimen.

The first objective of this investigation is to propose and develop a new method, the so-called energy approach, for studying the failure process of concrete and concrete members. The second objective is to obtain new knowledge of the failure phenomena of concrete and concrete members using this proposed method.

In order to avoid confusion, definitions of several technical terms used in this thesis are given herein. The term "failure" is used in its general meaning, and therefore implies yield, strength failure, fracture and rupture. The term "yield" means that the material behavior changes from elastic to plastic. At "strength failure", the load carrying

capacity of the system begins to decrease or disappears. The term "fracture" is the failure due to crack formation and propagation. The "rupture" means that the system disintegrates into two or more pieces.

In this thesis, the term "fracture process" is used for concrete specimens and "failure process" for reinforced concrete beams (RC beams), because concrete specimens seem to fail due to internal cracks, but RC beams fail due to yield in the steel and fracture in the concrete.

1.2 STUDIES ON FRACTURE OF CONCRETE

1.2.1 Introduction

The fracture of concrete has been studied by numerous investigators with various intentions using many kinds of methods. Thus, there would be many classifications of these studies.

Here, they are classified into two categories, namely, studies on the fracture process and studies on the fracture point. The fracture point, such as a strength failure point on the load-displacement diagrams, is considered to be a particular point in the fracture process, which is characterized by an initial region, a fracture point, a post-fracture region, etc.

The fracture process of concrete has been related to the changing process of the internal microscopic structure of concrete, or to mechanical responses of concrete due to the fracture of the system. A review of the studies on the fracture process of concrete is presented in Section 1.2.4.

The fracture point of concrete under various kinds of conditions, has been given by fracture criteria such as the fracture surfaces expressed in the stress space [49- 50], the

fracture toughness parameters in fracture mechanics, and others. Reviews of fracture mechanics and its application to concrete are given in Sections 1.2.2 and 1.2.3, respectively.

1.2.2 Fracture Mechanics

1.2.2.1 Griffith Theory

The first energy approach to the problem of fracture behavior of bodies containing sharp discontinuities was proposed by Griffith [2]. It is assumed in his proposition that an existing crack propagates catastrophically when the change in total potential energy becomes negative during crack extension. He considered an infinite plate of unit thickness having a through-thickness crack of length 2c under uniform tensile stress, f, applied at infinity. The total potential energy of the system, W_t, can be written as:

$$W_t = W_o - W_a + W_s \tag{1.1}$$

where W_o = elastic energy of the uncracked plate
W_a = elastic strain energy release due to the crack
W_s = surface energy used by the formation of the new crack surfaces

Griffith's proposition can also be expressed in other words, that the crack propagates when the available elastic strain energy release rate ($\partial W_a/\partial c$) exceeds the increase in the surface energy of the crack ($\partial W_s/\partial c$):

$$\partial W_t/\partial c = -\partial W_a/\partial c + \partial W_s/\partial c < 0 \tag{1.2}$$

Using a stress analysis by Inglis [3], the elastic strain energy release, W_a, is given as,

$$W_a = \pi f^2 c^2/E \tag{1.3}$$

E is modusus of elasticity. To simplify, only the equation for

the plane stress condition is considered here. The surface energy, W_s, is equal to the product of the unit surface energy, γ, and the new surface area of the crack, (2 x 2c):

$$W_s = 4c\gamma \tag{1.4}$$

Consequently, the total potential energy of the system, W_t, is

$$W_t = W_o - \pi f^2 c^2/E + 4c\gamma \tag{1.5}$$

By setting the first derivative of W_t with respect to crack length, c, equal to zero, the condition for crack propagation is given as:

$$\pi f^2 c/E = 2\gamma \tag{1.6}$$

This equation can be rewritten in the following forms:

$$c = 2\gamma E/\pi f^2 \tag{1.7}$$

$$f = \sqrt{2\gamma E/\pi c} \tag{1.8}$$

$$f\sqrt{c} = \sqrt{2\gamma E/\pi} \tag{1.9}$$

The left-hand side of Equation (1.6) represents the elastic energy per unit crack surface area that is available for infinitesimal crack extension, and has been called the crack driving force or the energy release rate, G. The right-hand side of Equation (1.6) represents the resistance of the material to crack extension, and is called the crack-resistance force, or the toughness, G_c. Thus, the criterion for the initiation of unstable fracture can be written as:

$$G > G_c \tag{1.10}$$

It is possible to experimentally measure the surface energy, γ, or the toughness, G_c ($=2\gamma$).

For a given stress, f, the critical crack length, c, is calculated from Equation (1.7). And for a given crack length,

c, the fracture stress, f, is given by Equation (1.8).

Because the modulus of elasticity, E, and the surface energy, γ, are material properties, the right-hand side of Equation (1.9) is constant in ideally brittle materials. Therefore, Equation (1.9) indicates that a crack in such materials extends when the product $f\sqrt{c}$ reaches a constant critical value. This critical value can be experimentally determined by measuring the fracture stress for a specimen having a known crack under uniform nominal stress. Equation (1.9) shows a basic concept of fracture mechanics, which is the structural study considering crack extension behavior as a function of applied loads.

1.2.2.2 Linear-Elastic Fracture Mechanics

The basic principle of fracture mechanics is that the stress field ahead of a sharp crack can be characterized by a single parameter, which is a function of the nominal stress and the size of the crack. Fracture mechanics can be divided into two categories: linear-elastic fracture mechanics and elastic-plastic fracture mechanics. The former is well developed, but the latter is still evolving. Linear-elastic fracture mechanics assumes that materials behave in a linear -elastic manner.

By using a method by Westergaard [4], Irwin [5] found that the stress fields in the vicinity of crack tips in Fig. 1.1 are given by:

$$
\begin{aligned}
f_x &= \frac{K}{\sqrt{2\pi r}} \cos\frac{\alpha}{2} \left[1 - \sin\frac{\alpha}{2} \sin\frac{3\alpha}{2}\right] \\
f_y &= \frac{K}{\sqrt{2\pi r}} \cos\frac{\alpha}{2} \left[1 + \sin\frac{\alpha}{2} \sin\frac{3\alpha}{2}\right] \\
\tau_{xy} &= \frac{K}{\sqrt{2\pi r}} \sin\frac{\alpha}{2} \cos\frac{\alpha}{2} \cos\frac{3\alpha}{2}\Big]
\end{aligned}
\qquad (1.11)
$$

when the stress components and the coordinates, r and α are

shown in Fig. 1.1. To save space, only the case of the plane strain and the opening mode (Mode I) is presented here. The three modes of crack surface displacement [6] are shown in Fig. 1.2, namely the opening mode (Mode I), the sliding mode (Mode II) and the tearing mode (Mode III). Equation (1.11) shows that the magnitude of distribution in the vicinity of the crack tip can be described by a parameter, K, which is called the stress intensity factor. The magnitude of the stress intensity factor is related to the magnitude of the applied uniform tensile stress, f, and the square root of the crack length, c. Generally, the stress intensity factor is shown as:

$$K = Ff\sqrt{a} \tag{1.12}$$

where F is a parameter that depends on the specimen and crack geometry.

The stress intensity factor for an infinite plate that contains a through-thickness crack of length 2c and is subjected to a uniform tensile stress, f, is:

$$K = f\sqrt{\pi c} \tag{1.13}$$

K at the onset of the crack propagation is designated as the critical stress intensity factor, K_c. Thus, the fracture criterion can be written as:

$$K > K_c \tag{1.14}$$

Equation (1.14) is derived by considering the stress field in the vicinity of the crack tip, although equation (1.10) is obtained by the energy-balance approach.

$K = f\sqrt{\pi c}$ from Equation (1.13) and $G = \pi f^2 c/E$ from Equation (1.6) for a through-thickness crack of length 2c. Therefore, the following relationship exists between the energy release

rate, G, and the stress intensity factor, K:

$$G = K^2/E \tag{1.15}$$

The stress approach in the derivation of the intensity factor, K, is applicable to the analysis of stable crack extension that occurs under cyclic loading, but the energy-balance approach to crack extension is not applicable to stable crack extension.

1.2.2.3 Elastic-Plastic Fracture Mechanics

For materials that exhibit small scale plastic flow around the crack tip, linear-elastic fracture mechanics is still applicable by modification. In such a case, Equation (1.6) is modified [7] as follows:

$$\pi f^2 c/E = 2(\gamma+\gamma_p) \tag{1.16}$$

where γ_p is the energy dissipated in the plastic work necessary for unstable crack propagation. Therefore, the material resistance to crack extension is given by the sum of the surface energy and the plastic work.

However, when the plastic zone near the crack tip is large compared with the crack length or the structure dimension, the materials show elastic-plastic behavior. For these materials, the toughness has been measured in terms of parameters such as R-curve resistance, J-integral, crack-opening displacement, etc.

The J-integral method seems to be one of the most promising techniques for evaluating the fracture toughness of concrete. The J-integral, a path independent line integral, can be applied to both linear-elastic and nonlinear-elastic materials. Thus the critical J-integral, J_c, can be considered a better parameter to describe the fracture behavior of concrete than the parameters G_c and K_c.

J_c indicates the resistance capacity to initiation of a main crack in the material. It is calculated from the stress strain field near a crack tip just before initiation of the main crack. Rice [8] formulated the J-integral as:

$$J = \int_{\bar{c}} \left(w dY - \tilde{T} \frac{\partial \tilde{u}}{\partial X} ds \right) \tag{1.17}$$

$\tilde{T}$ is traction vector, $\bar{c}$ is path of integral, $\tilde{u}$ is displacement vector, s is length along the path, and w is strain energy dencity. The J-integral may be considered as the potential energy difference between two identically loaded bodies having only minutely differing crack sizes [8]. This can be expressed as:

$$J = - \frac{1}{B} \frac{\partial W_t}{\partial a} \tag{1.18}$$

B is the specimen width and a is the crack depth.

For the linear-elastic case and also for the small yielding case, J is equivalent to G. For a nonlinear-elastic body, J may be interpreted as the energy available for crack extension [9]. For an elastic-plastic body where deformation is not reversible, J loses its physical significance as a crack driving force. For an elastic-plastic material, J is a measure of the characteristic crack tip elastic-plastic field [9]. In elastic-plastic materials, the value of J is equal to $-(1/B)\ \partial W_t / \partial a$ which permits J to be determined experimentally [9]. Begly and Landes [9] used a series of specimens with different initial notch depths to evaluate J according to Equation (1.18).

Rice, Paris and Merkle [10] pointed out that J can be calculated from a single specimen load-displacement curve. For compact tension specimens and beam specimens, it takes

the form:

$$J = \frac{2}{Bb} \int_0^{\theta_n} M d\theta_n \tag{1.19}$$

$$= \frac{2W_n}{Bb} \tag{1.20}$$

M is the applied moment and W_n is the component of W_t due to the notch. This calculation assumes that the rotation due to the notch, θ_n, is a function of M/b^2 for both linear-elastic and nonlinear-elastic materials. For example, M_p/b^2 is equal to $f_{rn}B/L$ for third-point loading in flexure. Therefore, it is assumed that the rotation is a function of tension stress, which is normal to the critical section, and implicitly a function of tension strain if stress is a function of strain.

If the notch is deep enough ($a/H \geq 0.6$), deformation is confined to the unnotched ligament region ahead of the notch. In such a case, the potential energy component of the unnotched body is small, so that Equation (1.20) can be simplified to:

$$J = \frac{2W_t}{Bb} \tag{1.21}$$

where W_t is calculated from the total area under the load-displacement curve of the specimen.

1.2.3 Application of Fracture Mechanics to Concrete

Kaplan [11] first applied the concepts of fracture mechanics to concrete in 1961. The results indicated that the fracture mechanics approach was applicable to concrete, and that the critical energy release rate, G_c, was influenced by specimen dimensions, loading rates, and mix proportions.

Since then the fracture toughness of concrete has been studied in terms of the parameters K_c and G_c by using the numerical method or the compliance method. In the numerical method, K_c (= $\sqrt{G_c/E}$) is calculated from Equation (1.12). In the compliance method, G_c (= K_c^2/E) is obtained from the ultimate load and the corresponding rate of change of compliance with notch depth.

Moavenzadeh and Kuguel [12] used the total-work method to measure γ (= $G_c/2$). Notched beams were loaded in flexure. The unit surface energy, γ, was calculated from the work done and the fracture area, and was comared with G_c and K_c.

The approximate values of K_c and G_c are summarized in Table 1.1 [13].

The calculation of K_c by the numerical method, which is the most popular way in fracture mechanics, assumes a homogeneous, isotropic, linear-elastic material. But these assumptions are not correct for concrete. Kesler, Naus and Lott [14] investigated the applicability of linear-elastic fracture mechanics to concrete, and concluded that the concepts of linear-elastic fracture mechanics do not apply to Portland cement concrete. Thus, a better parameter is needed to describe the fracture behavior of concrete.

The first application of the J-integral to the fracture of concrete was reported by Mindess, Lawrence and Kesler [15] in 1977. They compared J_c with K_c and G_c for cement paste, plain comcrete, and eight different volume fractions (0.25 $\sim$ 2.0 volume %) of steel and glass fiber reinforced concrete. Beam specimens (7.5 x7.5 x38 cm) were grooved at midspan with a carbide saw. Notch depths ranged from 3.8 cm to 5.1 cm. The beams were tested in third-point loading. Deflection was measured adjacent to the notch at midspan of the beam and was

related to the load point deflection. J_c was calculated at the peak load point employing Equation [1.20]. The results indicated that J_c is a more sensitive indicator of the benefits of fiber reinforcement than G_c and K_c, but large scatter was observed in J_c for fiber reinforced concretes.

Halvorsen [16], in his ph.D. thesis, extended the above investigation. Using almost the same experimental procedure as before, the following results were reported. Toughness of steel fiber reinforced concrete increases with fiber content, fiber length, aspect ratio, and end anchorage. The steel fiber reinforced concretes are notch-insensitive and toughness is dependent on specimen dimensions, especially the depth. For flexure, the type of loading (center-point or third-point) may not be significant. For nearly all of the concrete tested, large scatter was observed in the values of measured toughness.

Unstable fracture occurs when the stress intensity factor at the crack tip reaches a critical value, K_c. By knowing the critical value of K at failure for a given material, the designer can determine the critical limit of crack size in the structural members for a given design stress level, or conversely, determine the design stress level for an existing crack. Therefore, fracture mechanics is an important method for controlling brittle fracture and fatigue failures in metallic structures, which are mainly subjected to a tensile load and are likely to fail in a brittle manner.

The mechanical properties of concrete are different from those of metallic materials. The tensile strength of concrete is one order of magnitude lower than the compressive strength. Thus, concrete itself is seldom expected to carry tensile stress, but is usually used under situations of

compression stress. Though, the compressive failure of concrete is caused by numerous cracks initiating and propagating due to local tensile stress near flaws, an individual crack alone does not directly cause the failure of the total system. The fracture criteria proposed in fracture mechanics may give only the conditions for crack initiation in the concrete system. Consequently, it would be difficult to use the fracture toughness parameters, K_c, G_c, and J_c, to control the fracture of the whole concrete structure. But these toughness parameters could be a useful index to compare concrete properties, such as the resistance capacity to crack initiation.

1.2.4 Fracture Process of Concrete

Under a tensile load, a crack from a flaw in the concrete system initiates and propagates within a plane perpendicular to the load axis. If there is no arrester, the whole system may be easily fractured in a catastrophic manner due to the higher concentration of stress near the crack tip with the increase in crack length. However, under other loading conditions except pure tensile load, cracks caused by initial flaws in the concrete are not likely to directly cause the final fracture of the whole system.

For instance, the following five stages in crack propagation were presented by Kenny and Campbell [17],

(a) Initiation of the crack
(b) Slow growth prior to instability
(c) The critical condition
(d) Rapid propagation
(e) Crack arrest

Under a compressive load, a crack from a flaw tends to extend in the direction of the load axis. Therefore, at the

stage of stable crack growth, concentration decreases and thus extension of the crack is interrupted.

The internal structure of the concrete gradually changes during the period between the crack initiation and the strength failure of the system. This change has been designated as the fracture process [18].

It is known that in concrete subjected to a compressive load, cracks initiate at a low stress level which is less than one third of the strength [19]. As seen in the case of fiber reinforced concrete, the load-carrying capacity can be decreased gradually after strength failure by using a stiff testing machine. For the above reasons, the term "fracture process" in this thesis implies not only the crack propagation process up to strength failure, but also the initial region (before crack initiation) and the post-failure region.

The load-displacement relationship (or the stress-strain relationship) would be the most important mechanical response of the system. In order to estimate the degree of fracture of the system or to predict and control the fracture phenomena, the macroscopic mechanical response should be explained from a lower viewpoint. For example, to understand the fracture process of concrete, the phenomena should be correlated to the changing process of the internal structure of concrete.

The changing process of the internal structure of concrete has been studied using the following methods:

(1) Direct Observation of Internal Cracks [19-26]
Internal microcracking was observed by naked eye, a microscope, and X-rays. It is difficult, however, to observe a large area by these methods, and to obtain quantitative information from the observed data. Observation by naked eye or by microscope often requires

much time and effort.

(2) Detection of AE (Acoustic Emissions) [27-32]
The strain energy released by crack propagation is partially transformed into vibration energy which is dispersed as acoustic emissions. The progressive change in the internal structure of concrete can be observed by detecting AE. Also the crack sources can be located by AE. Recently, with the improvement of equipment for detecting AE, studies in this field have been developing. Because of the damping of waves, the size of specimens for AE tests is limited and the quantitative evaluation of the degree of fracture is difficult. The procedure in analyzing the data is relatively easy.

(3) Measurement Change in Physical Properties [33-35]
The change in the electronic resistance, or the ultrasonic pulse velocity has been studied. This method gives only the qualitative information on the internal change in concrete.

(4) Measurement of Volumetric Strain [36-37]
For concrete subjected to a uniaxial compressive load, the volumetric strain, e_v, is calculated from the lateral strain e_2 and the longitudinal strain e_1, as $e_v = e_1 + 2e_2$. There is a critical point, where the volumetric strain stops decreasing and begins to increase due to the increasing number of internal cracks. The stress at the critical volumetric strain has been correlated to the mechanical properties of concrete. However, the stress and strain distribution in concrete is far from uniform. It would be difficult to apply the stress-strain concept to concrete containing numerous discontinuities.

(5) Measurement of Dissipated Energy [38-47]

The degree of fracture in concrete can be quantitatively estimated by measuring the dissipated energy on load-displacement diagrams. This energy approach is the main subject of this thesis. The dissipated energy would be an index of plastic flow in the steel as well as of crack formation in the concrete. Thus, the failure phenomena of RC members can be analyzed by this method. This approach is applicable for large size test specimens.

There are few studies on the failure process of RC members from the view point of their component materials, concrete and steel reinforcement.

1.3 SCOPE

In this investigation, the failure process of concrete specimens and reinforced concrete beams (RC beams) is interpreted in terms of the energy transformation concept. This thesis consists of the following three parts:

1. A study on the fracture process of concrete under flexure
2. A study on the fracture process of concrete under compression
3. A study on the failure process of RC beams under flexure

Chapters 2 and 3 deal with the flexural fracture of concrete. The flexural fracture process is discussed in Chapter 2. The dissipated energy calculated from load-displacement diagrams was correlated to the crack length obtained by dyeing the crack. It was determined that the dissipated energy could be used as a parameter to estimate the degree of fracture in concrete. Cracks propagating in concrete were located by AE. The amount of AE was related to the dissipated energy.

The starting point of the main crack was determined by both the crack dyeing method and the AE detecting method.

Chapter 3 describes fracture toughness parameters, which were evaluated from concrete beam specimens under flexure. The best methods for evaluating the most meaningful and reproducible value of the critical J-integral, J_c, were investigated. The effect of aggregate size and steel fiber reinforcing on J_c was examined. The unit dissipated energy, S, was calculated by dividing the total consumed energy of complete rupture by the net section area. J_c and S were compared with other fracture toughness parameters in linear-elastic fracture mechanics, K_c and G_c.

Chapter 4 presents the application of the energy transformation concept to the fracture process of concrete under compression, which seems more complicated than that under flexure. The dissipated energy was divided into two components: one is consumed by crack formation, and the other is consumed by viscous friction. The effect of moisture content, loading rate, specimen size, and loading type, such as sustained or repeated loading, on the mechanical behavior of concrete was examined using the energy transformation concept. The resistance ability to the strength failure and the energy absorbing capacity of concrete in compression were also discussed.

Chapter 5 describes the study on energy transformation in the flexural failure process of RC beams, which are composite members of concrete and steel reinforcing bars. The role of the reinforcement and concrete in energy dissipation was determined. The amount of AE generations was related to the energy dissipation. The method of evaluating the plastic rotation capacity of RC beams was discussed in relation to

the measured plastic curvature and the dissipated energy in the reinforcement.

Table 1.1. Fracture Parameters [13].

Material	G_c, $\times 10^3$ erg/cm^2*	K_c, $\times 10^7$ dyn·cm$^{-3/2}$**
Cement Paste	2.0	2.0
Mortar	8.0	4.0
Concrete	20.0	6.0

* 10^3 erg/cm^2 $\simeq 10^{-1}$ kg/m

** 10^7 dyn·cm$^{-3/2}$ $\simeq 10^{-2}$ kg·m$^{-3/2}$

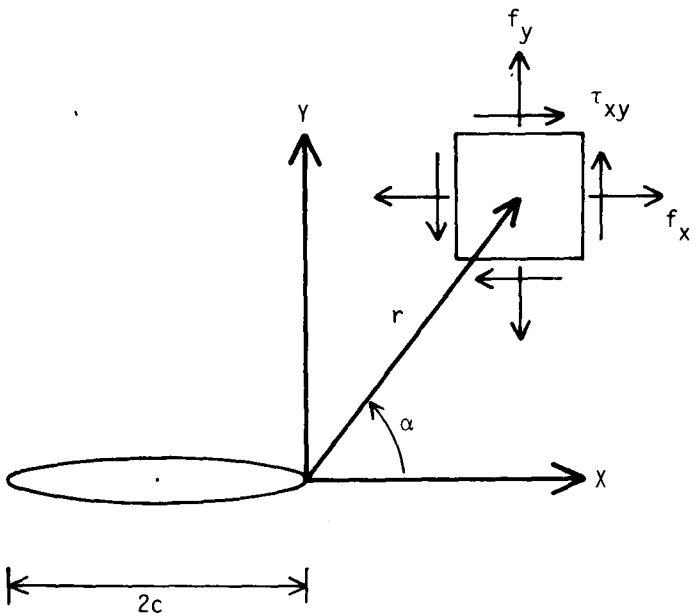

Fig. 1.1. Coordinate System and Stress Components in Vicinity of Crack Tip.

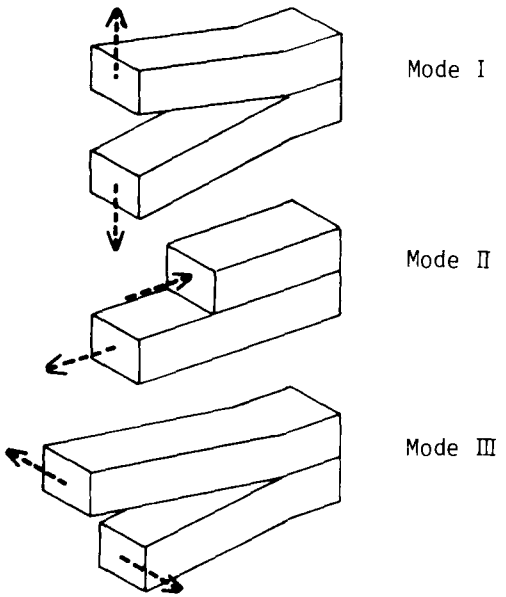

Fig. 1.2. Three Bacic Modes of Crack Surface Displacement.

CHAPTER 2. FRACTURE PROCESS OF CONCRETE IN FLEXURE

2.1 INTRODUCTION

As described in Section 1.1, the energy W_t applied to a concrete specimen by an external load is generally divided into the reversible strain energy W_r and the irreversible dissipated energy W_i. The energy W_r can be taken from the specimen by unloading. The energy W_i seems to be dissipated in crack formation and viscous friction. By examining the energy division and dissipation in concrete, we can study the fracture process of concrete in terms of the energy transfer process.

In this paper, the fracture process of concrete in flexure is investigated by means of the energy transfer concept. The fracture process of concrete in flexure may be closely related to the fracture process in tension. Concrete in flexure is fractured by fewer cracks than in the case of concrete in compression.

Not only in the case of a tensile load, but also in the case of a compressive or shear load, microscopic fracture is initiated by local tensile stress in the vicinity of micro flaws in the concrete. To evaluate the amount of energy dissipation in concrete in compressive or shear fracture, it is important to measure the dissipated energy in tensile fracture. However, the tensile fracture of concrete is more unstable than the compressive fracture. It is generally difficult to control the crack propagation velocity in direct tension tests. Thus, flexure tests, which are more stable than tension tests, were adopted in this investigation.

In flexural tests of ordinary beams, it is not easy to predict the region of crack initiation. When the energy

release rate can not be controlled, the fracture process in flexure is quite unstable, so that the beams for the flexural tests of this study were notched on their tension face in order to define the region of crack initiation and to decrease the energy release rate during concrete fracture.

In this study, complete load-displacement diagrams including the post-failure region were recorded for the concrete test beams, which varied in strength and water content. Reversible strain energy and irreversible dissipated energy in the fracture process were calculated from the load-displacement diagrams. Crack growth from a notch was related to the irreversible dissipated energy. The acoustic emission method [30-31], which has been developed and utilized in the study of rocklike materials, was applied to the fracture process of concrete in flexure. Propagating cracks in beams were located by detection of acoustic emissions (AE). The number of AE was also related to the irreversible dissipated energy.

2.2 EXPERIMENTAL PROCEDURES

2.2.1 Test Program

Five series of tests were conducted with various concrete qualities, moisture contents, and specimen sizes, all of which seem to affect the fracture process of concrete under flexure, as follows:

(I) Load-Displacement Diagram
The influence on load-displacement diagrams was studied with respect to concrete strength, moisture content, and notch presence.

(II) Energy-Displacement Relationship
Strain energy and dissipating energy of concrete

beams under flexure were calculated from load-displacement diagrams. The fracture process of concrete under flexure was interpreted in terms of an energy transformation concept.

(III) Fracture Process under Flexure and under Compression
The fracture process under flexure was compared with that under compression, using the load- and energy-displacement relations.

(IV) Dissipated Energy and Crack Growth
Dissipated energy calculated from load-displacement diagrams was correlated to the crack length obtained by dyeing the crack.

(V) Detection of Cracking with Acoustic Emissions
Cracks propagating in the beams were located by AE. The amount of AE was related to the dissipated energy.

2.2.2 Materials and Mix Proportions of Concrete

Four kinds of concrete A, B, C and D with different mix proportions were used in this study. Low strength concrete B and high strength concrete C were used in contrast to normal strength concrete A. The mix proportions and measured slumps are tabulated in Table 2.1. Ordinary Portland cement was used in concrete A, B and D. High early strength Portland cement and a water-reducing agent were used in concrete C to make it stronger. Toyoura standard sand (specific gravity: 2.63), which is fine, uniformly graded sand, was used in concrete A, B, and C to make it easy to detect cracks by dyeing. River sand (specific gravity: 2.59, fineness modulus: 3.04) was used in concrete D. Crushed coarse aggregate (specific gravity: 2.64, maximum size: 15 mm) was used in each type of concrete. Grading curves of the aggregates are shown in Fig. 2.1.

The relation between the test series and the concrete is

also shown in Table 2.1 by an asterisk.

2.2.3 Specimens and Concrete Strength

Beams (4.7x10x39 cm) had a V-shaped notch with an equilateral triangle section 1 cm in depth, as illustrated in Fig. 2.2. Unnotched beams were also used as a comparison with the notched beams. Two large sized notched beams (10x20x79 cm) were made of concrete D to examine the effect of size on the accuracy of AE detection. Cylindrical specimens (ϕ10x20 cm) were used in the compression tests.

One day after casting, beams were unmolded. They were then cured in 20 °C water. When beams were tested in wet condition, they were taken out from the curing water just before loading and their surfaces were wiped with a dry cloth. When beams were tested in dry condition, they were exposed in the laboratory after a predetermined curing period, and then left until they reached testing age. Cylindrical specimens for compression tests were handled similarly to beam specimens except for a capping procedure. The two large size beams of concrete D for AE detection were stored in the laboratory after unmolding and then one of them was loaded after 60 days and the other at 118 days.

Beam specimens and cylindrical specimens of concrete B were tested in both wet and dry conditions to investigate the effect of drying. The group of specimens of concrete B tested in the wet condition was given the name BW, and the group tested in the dry condition was given the name BD. The loss of water and the percentage of decreased moisture content from the beams of group BD were 82 g and 2.5% respectively. Specimens of concrete A and C were tested in the wet condition; thus, they were designated AW and CW. Specimens of concrete D were tested in dry condition, so they

were named DD. The water curing periods and testing ages of the five groups of concrete specimens, AW, BW, BD, CW and DD, are tabulated in Table 2.2.

More than four specimens were used for each test condition and the test results were expressed as the averages. Compressive strength f_c, modulus of rupture f_{rn} and f_r, which were calculated from beams with and without a notch respectively, and the strength ratios f_c/f_r and f_{rn}/f_r of the five groups are also shown in Table 2.2. The peak flexural loads, from which the moduli of rupture were calculated, are added in Table 2.2.

2.2.4 Loading Apparatus

Two types of loading machine were used. One of them was a stiff testing machine which was automatically controlled with a servo-controller. The other was an improved testing machine, in which a sufficiently high stiffness was obtained by connecting the two lateral frames of the machine with a high strength steel rod of 32 mm in diameter. The improved testing machine for flexural tests is illustrated in Fig. 2.3. The load of any beam was 1/10 $\sim$ 1/20 of that of the steel rod. The load cell indicated as (A) in Fig. 2.3 was attached to the end of the steel rod (C) with part (B).

The stiff testing machine was used for the flexural tests of groups AW and CW and for the compressive tests of all groups. Beam specimens of groups BW, BD and DD were tested in the improved testing machine.

Beam specimens were loaded at the center-point on a span of 33 cm, except in the case of the large size beams, where the overall span was 66 cm.

The loading rate of beams at the loading point in the direction of the load was 0.05 $\sim$ 0.5 mm/min. in displacement.

In the test series (V), where propagating cracks were located by detection of AE, the loading rate of the beams was slower and almost reached zero when AE waves were being registered on the recording paper. Consequently it took about two or three hours to finish loading one beam.

2.2.5 Measurement of Displacement

The load-point displacement (deflection) of the beam specimens was measured by a straingaged cantilever. As shown in Fig. 2.4, the measuring apparatus was directly attached to the beam in order to eliminate the displacement due to deformation at the loading and supporting points. The center fixing point of the apparatus was moved a little from the line of the loading point toward one of the supporting points so as not to disturb crack initiation and propagation. The error in the displacement measurement due to the movement of the center fixing point was considered apart from this study and proved minimal.

The compressive displacement (deformation) of the cylindrical specimens was measured by three differential transformers attached to the specimens.

Load-displacement diagrams for all specimens were recorded on an X-Y recorder.

2.3 LOAD-DISPLACEMENT DIAGRAM

In this study the investigation of energy transformation in the concrete fracture process is based on the load-displacement diagrams. The properties of the load-displacement diagrams of beam specimens and their treatment are discussed in this section.

Notched beams were mainly used in the bending tests in order to define the region of crack initiation. The load

-displacement diagrams of notched and unnotched beams of the low strength concrete group BW are shown in Fig. 2.5 and Fig. 2.6 respectively to show the influence of the notch on the diagram shapes. As shown in those figures, the peak flexural load of the notched beams was lower than that of unnotched beams. The slope of the falling branch curve in the post -failure region of the diagrams for the notched beams was gentler than that for the notch-less beams. This fact means that the energy release rate of notched beams during crack propagation was smaller.

In the case of the other groups which have a greater modulus of rupture than the low strength group BW, the displacement rate in the descending region of the unnotched beam diagrams could not be controlled with the testing machines and they ruptured rapidly, because the slope in the falling branch of the diagrams was steep. Therefore, load-displacement diagrams of notched beams will be used hereafter, when the diagrams of different groups are compared.

The load-displacement diagrams of the BD group are shown in Fig. 2.7 for the purpose of considering the influence of moisture content in the beams on the diagram shapes. It is seen from Figs. 2.5 and 2.7 that the peak flexural load of the dry group BD was greater than that of the wet group BW.

Load-displacement diagrams were treated as follows. As seen from Fig. 2.5, even the load-displacement diagrams obtained from beams under the same conditions are not identical. Diagrams in Figs. 2.6 and 2.7 also have scatter. Therefore, representative diagrams should be used for the purpose of comparing diagrams of different groups. A representative diagram represents a graphical average of all the diagrams in a particular group.

One of the purposes of this study is to investigate the change in dissipated energy and elastic energy during the fracture process in flexure. In the next section, these energies are calculated from the so-called "gradually increased repeated load-displacement diagrams" (abbreviated to GIR-diagrams), in which loading and unloading are repeated several times. Fig. 2.8 is an example of a GIR-diagram. The dotted line in Fig. 2.8 is the envelope curve.

The representative diagram of five envelope curves from the GIR-diagrams of the AW group is shown by a dotted line in Fig. 2.9, and is compared with the representative diagram of the ten "constantly increased load-displacement diagrams" (CI-diagrams) of the same group AW expressed by a solid line. The envelope diagram had a slightly greater displacement than the CI-diagram. But the difference in displacement between them was smaller than the scatter in the diagrams of Figs. 2.5, 2.6 and 2.7, so that we can ignore the difference. Because they can be considered to be identical, we obtain the representative diagram for the group having both CI- and envelope diagrams.

Fig. 2.10 shows the representative diagrams of notched beams in four groups AW, BW, BD and CW. The diagrams show a trend indicating that as the peak flexure load on the concrete increases, the peak slope in the falling branch becomes steeper.

2.4 ENERGY-DISPLACEMENT RELATIONSHIP

The energy W_t applied to a specimen by an external load is converted into strain energy W_r and dissipated energy W_i, that is $W_t = W_r + W_i$.

At point U, one of the unloading points of the GIR-dia-

gram shown in Fig. 2.8, the dissipated energy W_i is indicated by the area OPUR, which is bounded by the displacement axis OR, the unloading curve UR and the envelope curve OPU of the loading curves. On the other hand, the strain energy W_r is indicated by the area RUQ, below the unloading curve UR. The energy division in the fracture process of concrete in flexure may be found by calculating the energies W_t, W_r, and W_i at each unloading point. The energies were determined by measuring the corresponding areas in the GIR-diagrams with a planimeter.

For the three concrete groups AW, BW and BD, the energies W_t and W_r were calculated using two GIR-diagrams from each group, and are related to the displacement in Fig. 2.11. In Fig. 2.11, the energies W_t and W_i are normalized by W_{tp} which is the value of W_t at the peak flexure load, and the displacement D is also normalized by D_p which is the displacement corresponding to the peak load. Such curves as shown in Fig. 2.11 will be referred to as energy-displacement relationships hereafter.

As shown in Fig. 2.11, the strain energy W_r stored in beams was largest at the point of $D/D_p = 1.1 \sim 1.3$, slightly over the peak load point of $D/D_p = 1.0$. The values of W_r and W_r/W_{tp} at the peak load point and the maximum values of W_r and W_r/W_{tp} with the corresponding value of D/D_p are shown in Table 2.3. The values of W_r/W_{tp} in the wet concrete groups AW and BW were less than those of the dry concrete group BD. Before the peak load was reached, the proportion of the dissipated energy W_i to the work done W_t in the wet concrete groups was relatively greater than that in the dry concrete group.

2.5 FRACTURE PROCESS UNDER FLEXURE AND UNDER COMPRESSION

A discussion of the load-displacement diagrams and the

energy-displacement relationships for concrete specimens in the compressive fracture process appears in Chapter 4. The aim of this section is to compare the compressive fracture process with the flexural fracture process by using the energy-displacement relationships.

As an example, the GIR-diagram of a cylindrical specimen from the AW group under a compressive load is shown in Fig. 2.12. We can investigate the difference between the compressive and flexural fracture processes by comparing Fig. 2.12 with Fig. 2.8, which shows the GIR-diagram of a beam specimen from the same AW group. These figures indicate that before the peak load point, the load-displacement diagrams in flexure were straighter than those in compression. Moreover, the ratio of W_i to W_t in flexure was smaller than that in compression.

Energy-displacement relationships of cylindrical specimens of the concrete groups AW and BW are shown in Fig. 2.13. They were obtained by the same method as was used for beam specimens. As seen from Fig. 2.13, the strain energy stored in a specimen in the compressive fracture process became maximum at the peak load ($D/D_p = 1$). The strain energy W_r and energy ratio W_r/W_{tp} at the peak compressive load are added in Table 2.3. Table 2.3 shows that the maximum value of W_{rp}/W_{tp} in flexure was one and a half times as large as that in compression.

In the fracture process of concrete in compression, cracks start at a comparatively low load level before the peak load, but the cracks are likely to be arrested so that a new stable stage appears. On the other hand, in the flexural fracture process, cracks start at a higher load level, and the cracks are apt to cause the collapse of the specimen [18].

Such a distinction between the compressive and flexural fracture processes can be explained by the results of this section, where the load-displacement diagrams and energy-displacement relationships are compared.

2.6 DISSIPATED ENERGY AND CRACK GROWTH

The dissipated energy, which is calculated from the load-displacement diagrams, seems to be consumed mainly as surface energy in crack formation. The value might quantitatively indicate the degree of fracture in concrete. The relationship between dissipated energy and crack depth in beams was examined to prove the physical meaning of the dissipated energy.

The crack surface in each beam due to loading was dyed with a dark brown dye after being unloaded. The dark brown dye, a solution of polycyclic sulfonate type compounds, is an admixture for concrete used as a high-range water reducing agent. After the dye had dried, the beams were reloaded and were broken into two pieces. At the position of the notch the dyed fracture surface was measured to obtain the average crack depth due to the first loading.

Fig. 2.14 shows examples of the dyed fracture surfaces. No branch cracks due to reloading were observed in the vicinity of the first crack tip in each specimen. Therefore, it is likely that the crack due to reloading started from the tip of the dyed crack.

The relationship between the crack depth, measured from the dyed crack surfaces, and the dissipated energy measured from the load-displacement diagrams, is shown in Fig. 2.15 for concrete beams of groups BW, BD and CW. The maximum possible crack depth was 9 cm, because the notch depth was 1 cm and the beam height was 10 cm. Although there is a slight trend in Fig. 2.15 indicating that the ratio of

the crack depth to the dissipated energy is low when the crack depth is less than 4 cm, in general the crack depth is proportional to the dissipated energy. The results prove that the degree of fracture in concrete, that is the amount of cracking, can be represented by the dissipated energy measured from the load-displacement diagrams.

When the level of the first loading was lower than the peak load, dyed crack surfaces could not be found. This fact suggests that in the flexural fracture process of concrete, cracks are few before the peak load is attained and they mainly propagate after the peak load has been reached.

2.7 DETECTION OF CRACKING WITH ACOUSTIC EMISSIONS

Crack sources were located inside a beam (named AE-1) of the concrete group BD and large size beams (AE-2, AE-3) of the concrete group DD. The number of AE's in Beam AE-3 was counted.

The detail and accuracy of the methods used in this experiment to locate crack sources and to count AE's are discussed in the references [30] and [31], so that only an outline of the methods is described here.

AE sources inside the beams were calculated from the differences in the arrival times of AE with a frequency ranging from 10 to 300 kHz. The AE's were detected by four pickups attached to each beam as shown in Figs. 2.16, 2.17 and 2.18. The arrival time difference T_i of AE waves was measured as shown in Fig. 2.19. The distance differences were calculated by multiplying T_i by the propagation velocity V, of the waves. The coordinates (x,y,z) of an AE source were calculated from the following equation:

$$\sqrt{(x-a_i)^2+(y-b_i)^2+(z-c_i)^2} - \sqrt{x^2+y^2+z^2} = T_i \cdot V \quad (i = 1,2,3) \qquad (2.1)$$

Pickup-1 is the origin and (a_i, b_i, c_i) are the coordinates of the other three pickups.

The propagation velocity of AE waves in Beam AE-1 was measured before the loading test. After every ten instances of AE recording, the velocities in Beams AE-2 and AE-3 were measured during the loading test by the use of electrically enduced pulse wave from pickup-5.

The number of AE generations in Beam AE-3 was counted with pickup-1. The AE's detected by a discriminator were those which had a frequency of from 20 to 300 kHz, were amplified to 60 dB, and were over 100 mV. The counted AE number was automatically recorded every ten seconds.

Calculated AE sources inside the beams are shown in Figs. 2.20, 2.21 and 2.22. The order of AE generations is plotted on the load-displacement diagrams in Figs.2.23, 2.24 and 2.25. In these figures, the circles mean that it was possible to calculate the AE sources, and the black points mean it was not. Figs. 2.26, 2.27 and 2.28 show the relationship between the location of each AE source and the order of the AE generation expressed in terms of the beam displacement.

The source locations of 78 values out of 150 AE's recorded for Beam AE-1, 46 values out of 102 for Beam AE-2, and 50 out of 124 for Beam AE-3 could be calculated. In cases where the wave shapes were not clear or were disturbed by noises, AE sources could not be calculated.

As shown in Figs. 2.20, 2.21, and 2.22, AE sources are located within a length of 3 to 4 cm in the span direction

(Y-direction). Because the accuracy of the method is about 1 cm [31] and fracture surfaces have variations of 1 to 2 cm, it might be reasonable to consider that the locations of AE sources agree reasonably with the observed fracture surfaces. AE generations are due to crack extension [30-31], which is related to energy dissipation in the fracture process. Therefore, considering the accuracy of the method, it is reasonable to conclude that the energy dissipated in the fracture of specimens was used in the neighborhood of the observed fracture surfaces.

It is seen from Figs. 2.23 through 2.28, that only a few AE generations are recorded before the peak load, and that they would be due to the crushing under the center loading point. As the beam displacement increases, the locations of AE sources move as a rule from the bottom of the beam to the top with scattering also in the direction perpendicular to the face of the beam.

The relationship between the counted AE number in Beam AE-3 and the beam displacement is shown in Fig. 2.29. As shown in Fig. 2.29, the counted AE number was relatively small before the peak load point, where the displacement is 0.25 mm, but remarkably increased after the peak load point. This means that cracks propagate mainly after the peak load. The observation agrees with the results previously obtained by the observation of dyed crack surfaces and the measurement of the dissipated energy from load-displacement diagrams.

Under the GIR-loading as shown in Fig. 2.29, AE's occur mainly on the envelope curve and relatively few are found on the unloading-loading curves. A phenomenon like the so-called Kaiser effect [30, 48] was also recognized after peak load.

Five repetitions of loading-unloading were performed on

Beam AE-3, as shown in Fig. 2.25. The relation between the AE number and the dissipated energy calculated for each repetition is shown in Fig. 2.30. According to Fig. 2.30, the dissipated energy constantly increases as the AE number increases. Consequently, it would be possible to evaluate the degree of fracture of the concrete by the AE number, if the loading conditions are constant.

Results obtained from AE should be considered as quantitative scales to investigate the fracture process of the system, rather than as absolute values, because the AE detection depends on pickup properties, discrimination levels, etc. The relationship between cracks and AE will be made clearer by further studies on the AE number, the source location, and the frequency range.

2.8 CONCLUSION

The flexural fracture process of concrete was investigated in regard to the energy transfer process. The results can be summarized as follows:

(1) The load-displacement diagrams including the region after the peak load were obtained for notched beam specimens by using stiff testing machines. There was a tendency that the higher the concrete strength, the greater the maximum negative slope after the peak load on the load-displacement diagram.

(2) Elastic strain energy, W_r, stored in beam specimens reached maximum at the point of $D/D_p = 1.1 \sim 1.3$, which was slightly over the peak load point of $D/D_p = 1.0$. Before the peak load point, the proportion of the dissipated energy W_i to the work done W_t in the saturated concrete beams was relatively greater than that in the dried con-

crete beams.

(3) Before the peak load point, the load-displacement diagrams in flexure were straighter than those in compression. Moreover, the ratio of W_{ip} to W_{tp} in flexure was smaller than that in compression. These results can explain the fact that cracks during the flexural fracture process initiate at a relatively higher load level, and they are more likely to cause the final failure of the whole system than in the case of the compressive fracture process.

(4) The crack depth observed by dyeing the fracture surface was proportional to the dissipated energy, which was calculated from the load-displacement diagrams. Consequently, it is possible to estimate the fracture in concrete by the dissipated energy calculated from the load-displacement diagrams.

(5) The cracks during the flexural fracture process of concrete propagated remarkably after peak load. This is supported by the experimental results obtained by calculation of the dissipated energy, observation of the dyed fracture surfaces, and detection of AE.

(6) Locations of crack sources obtained by AE detection coincided well with the observed fracture surface. This means that the dissipated energy during the fracture of beams was consumed in the neighborhood of the observed fracture surface.

(7) Under the GIR-loading, AE's occured mainly on the envelope curve in the load-displacement diagram with relatively few on the unloading-loading curves. A phenomenon like the so-called Kaiser effect was recognized even after peak load.

Table 2.1. Mix Proportions.

Mix	Water-Cement Ratio	Sand-Aggr. Ratio	Mix Materials, kg/m^3				Slump cm	Test Series				
			Water	Cement	Sand	Gravel 5∿15mm		I	II	III	IV	V
A	0.64	0.40	219	343	696	1053	15	*	*	*	-	-
B	0.65	0.40	162	250	788	1186	9	*	*	*	*	*
C	0.49	0.38	200	410	658	1082	5	*	-	-	*	-
D	0.63	0.57	240	380	950	725	20	-	-	-	-	*

Table 2.2. Test Conditions and Concrete Strength.

Group	Test Conditions: Curing in water days	Testing Age days: Flex.	Testing Age days: Comp.	Comp. Strength f_c, kg/cm^2	Modulus of Rupture: Notched f_{rn}, kg/cm^2	Modulus of Rupture: Unnotched f_r, kg/cm^2	Peak Load P_p, kg: Notched	Peak Load P_p, kg: Unnotched	$\frac{f_c}{f_r}$	$\frac{f_{rn}}{f_r}$
AW	13∿16	14∿16	17	254	43.7	48.7	339	464	5.2	0.90
BW	42∿48	43 ∿ 49		135	28.0	31.9	215	304	4.2	0.88
BD	13	43 ∿ 49		162	34.0	-	262	-	-	-
CW	13∿16	17	14	591	67.9	82.6	526	787	7.2	0.82
DD	0	84	-	-	35.5	-	273	-	-	-

Table 2.3. Elastic Strain Energy W_r.

Group	Beam Specimens in Flexure: At Peak Load $D/D_p=1$		Beam Specimens in Flexure: At Maximum W_r			Cylindrical Specimens in Compression	
	W_{rp}, kg·cm	$\frac{W_{rp}}{W_{tp}}$	W_r, kg·cm	$\frac{W_r}{W_{tp}}$	$\frac{D}{D_p}$	W_{rp}, kg·cm	$\frac{W_{rp}}{W_{tp}}$
AW	0.86	0.59	0.92	0.63	1.2	172	0.40
BW	0.37	0.59	0.41	0.65	1.3	115	0.31
BW	0.52	0.73	0.53	0.75	1.1	-	-

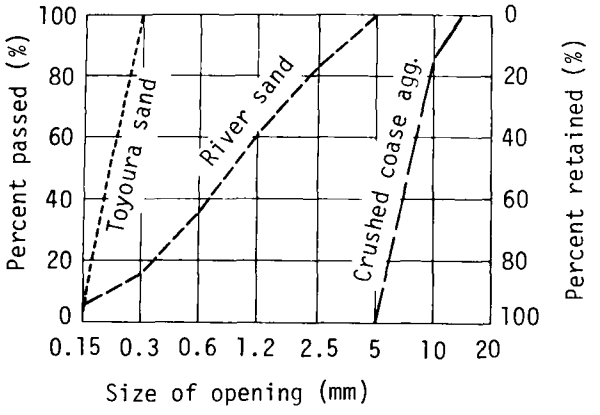

Fig. 2.1. Gradation of Aggregates.

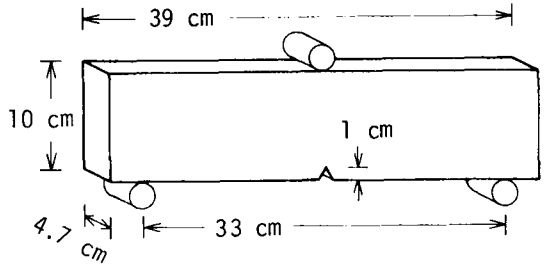

Fig. 2.2. Beam Specimen Geometry.

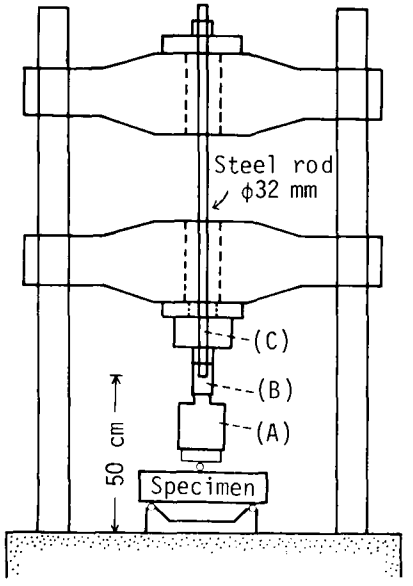

Fig. 2.3. Improved Testing Machine.

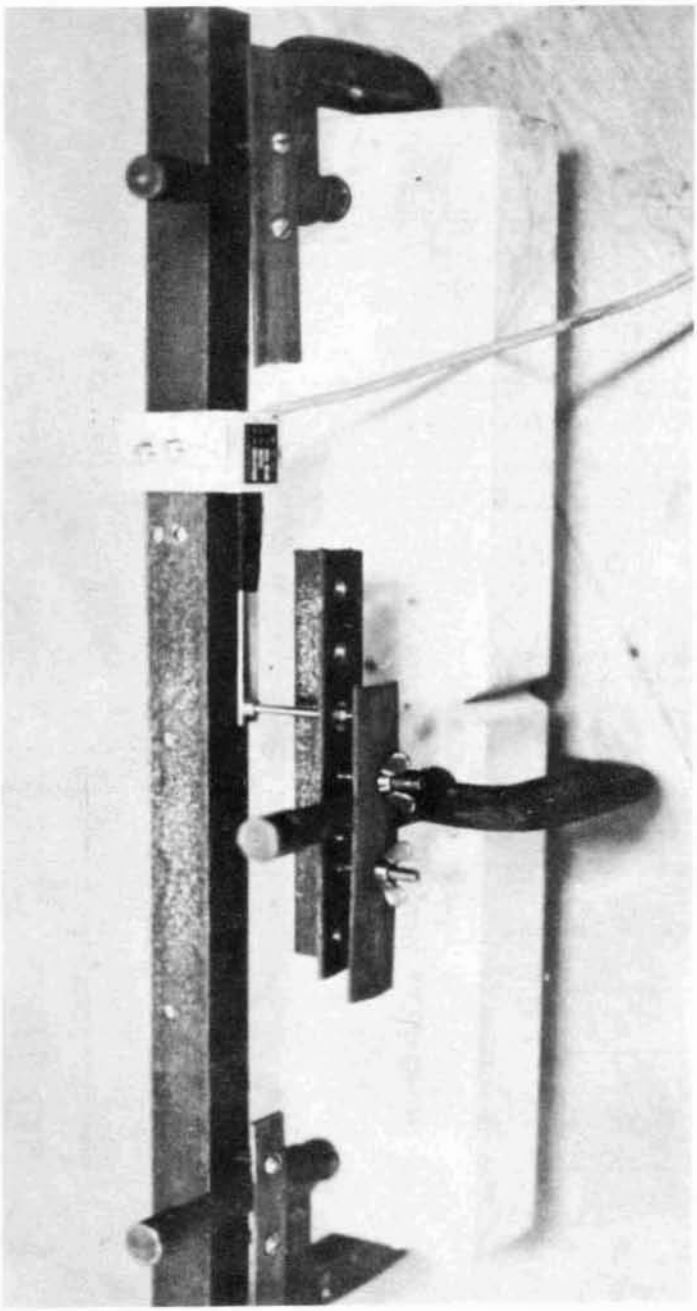

Fig. 2.4. Displacement Measurement Equipment.

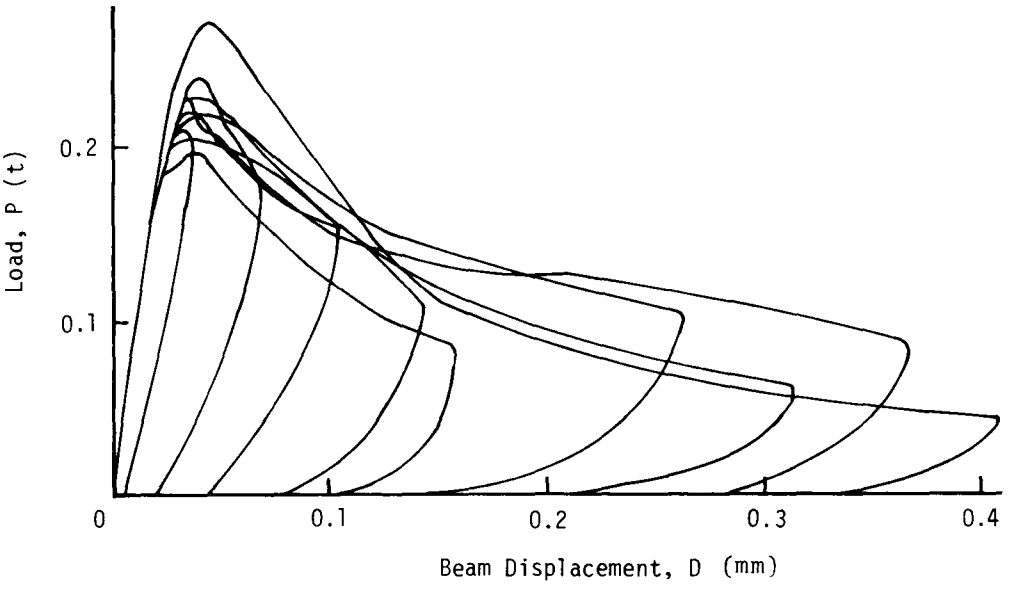

Fig. 2.5. Load-Displacement Diagrams of Wet Notched Beams (BW).

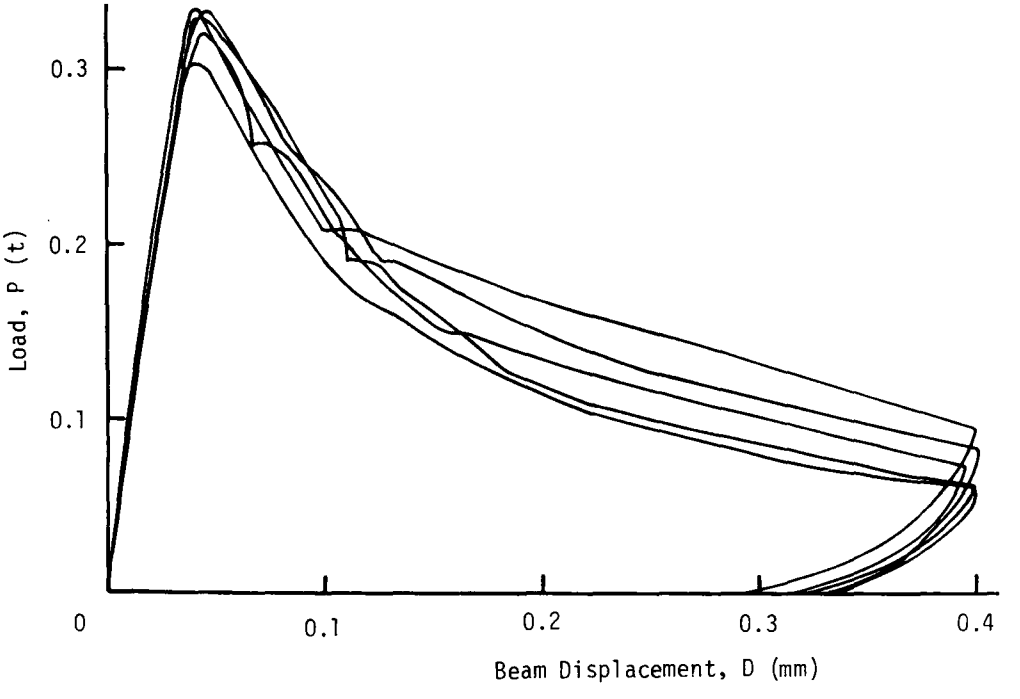

Fig. 2.6. Load-Displacement Diagrams of Wet Unnotched Beams (BW).

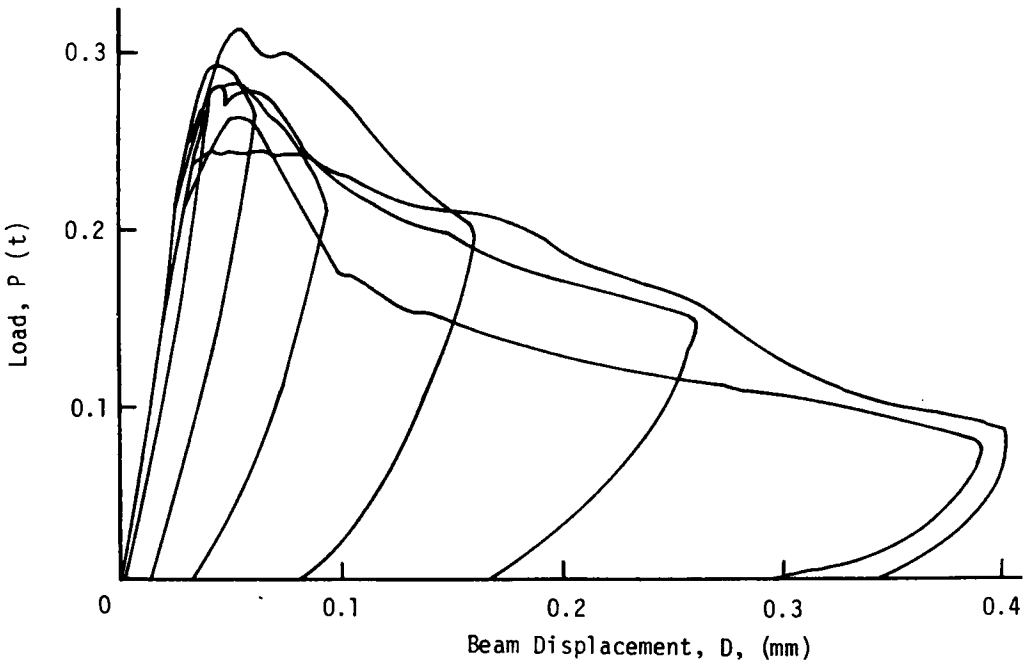

Fig. 2.7. Load-Displacement Diagrams of Dry Notched Beams (BD).

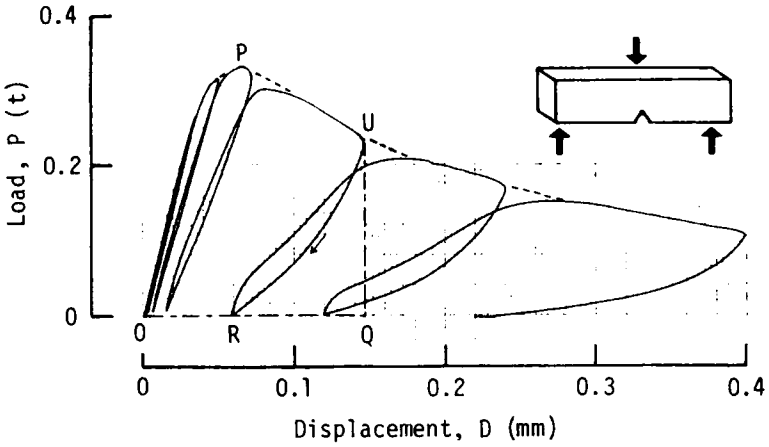

Fig. 2.8. GIR-Diagram of Beam Specimen.

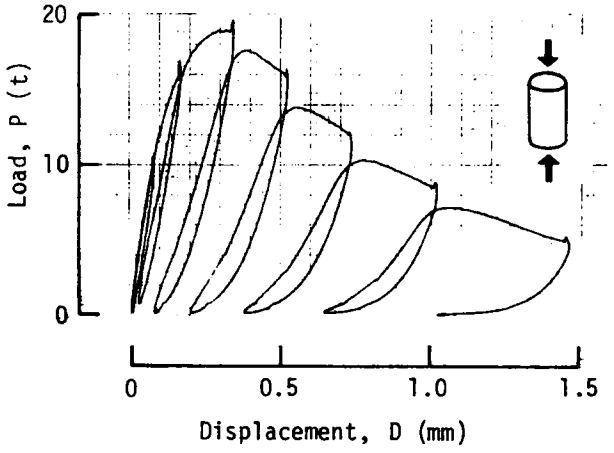

Fig. 2.12. GIR-Diagram of Cylindrical Specimen.

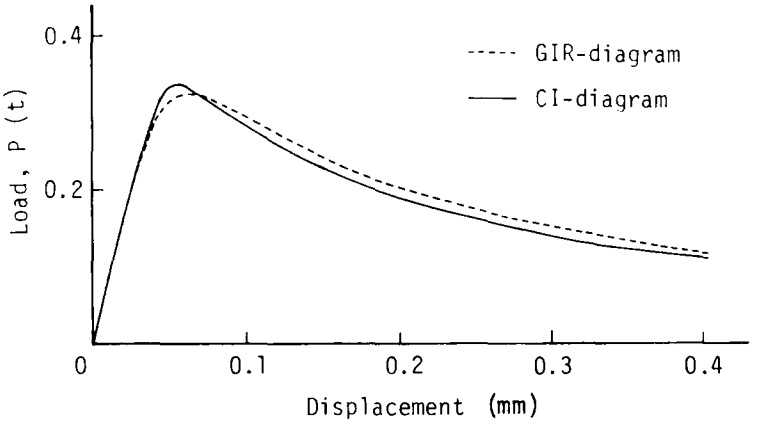

Fig. 2.9. CI-Diagram and Envelope of GIR-Diagram.

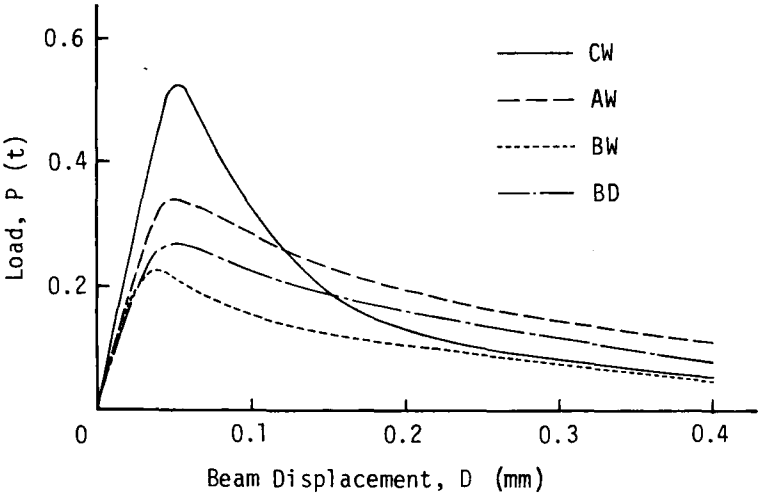

Fig. 2.10. Representative Load-Displacement Diagrams.

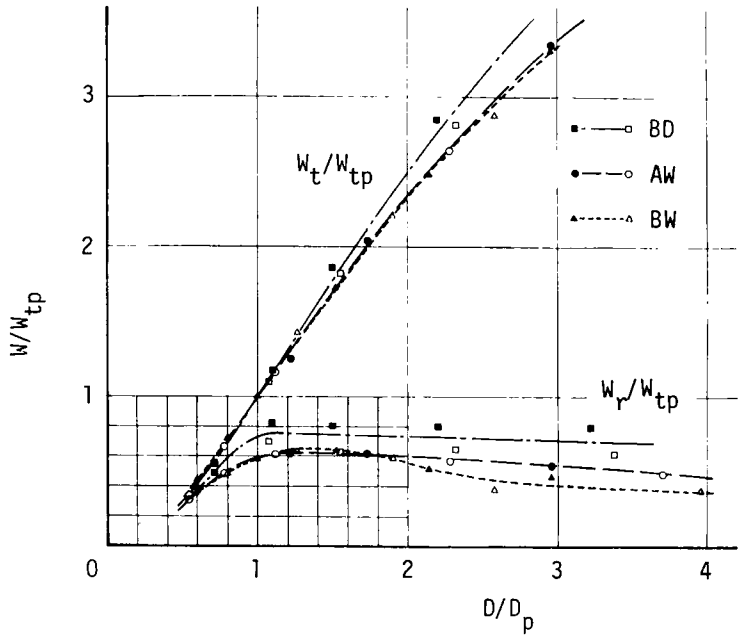

Fig. 2.11. Energy-Displacement Relationship under Flexure.

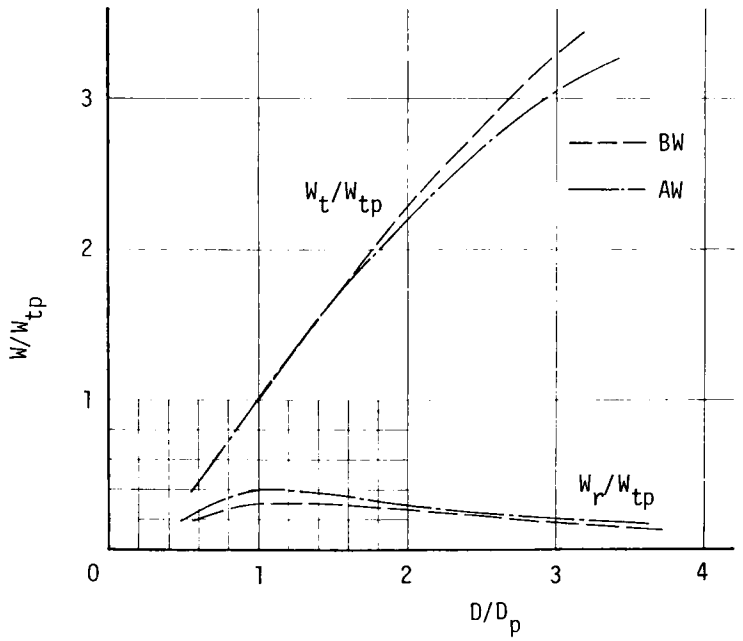

Fig. 2.13. Energy-Displacement Relationship under Compression.

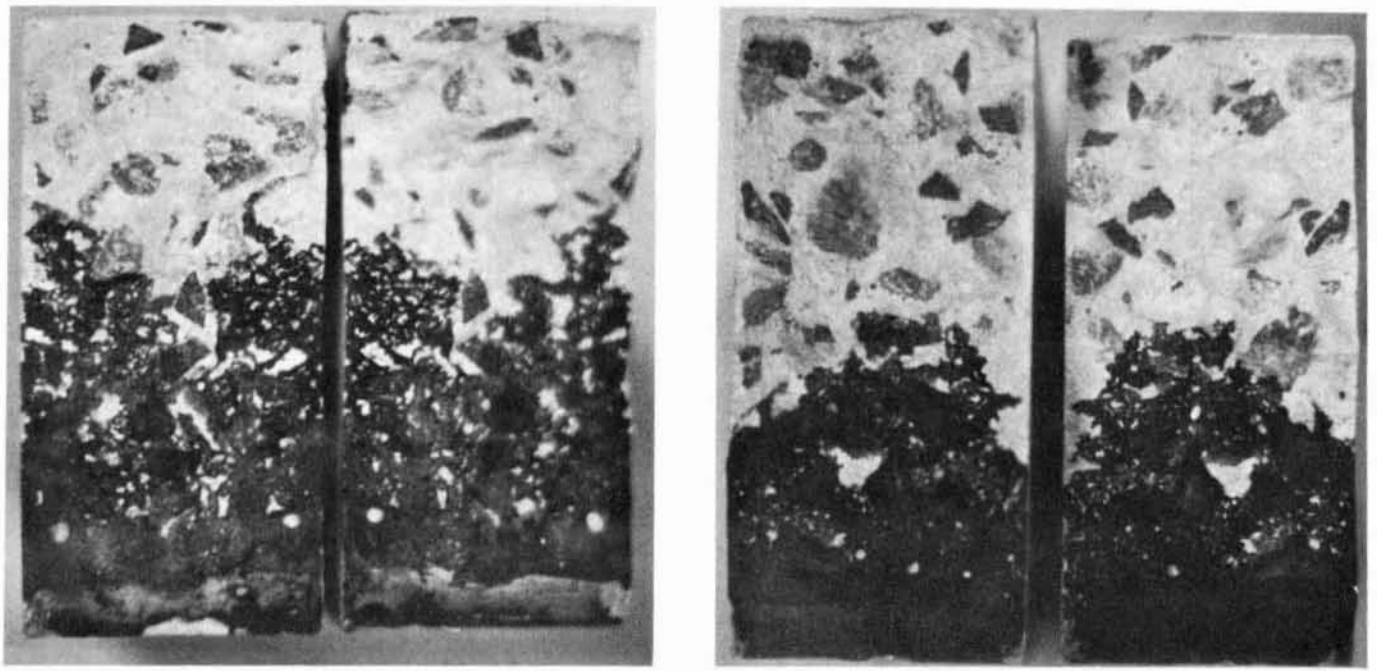

Fig. 2.14. Dyed Fracture Surfaces.

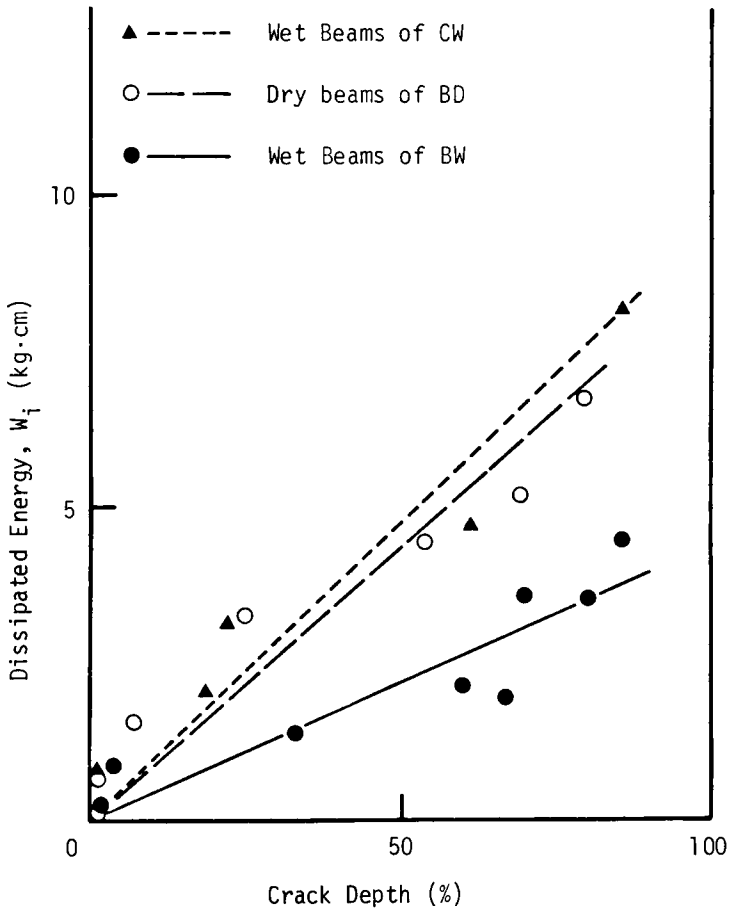

Fig. 2.15. Crack Depth and Energy Dissipation.

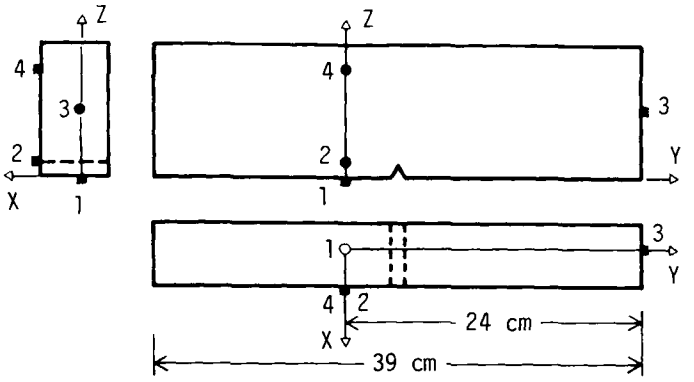

Fig. 2.16. Position of Pick-ups on Beam AE-1.

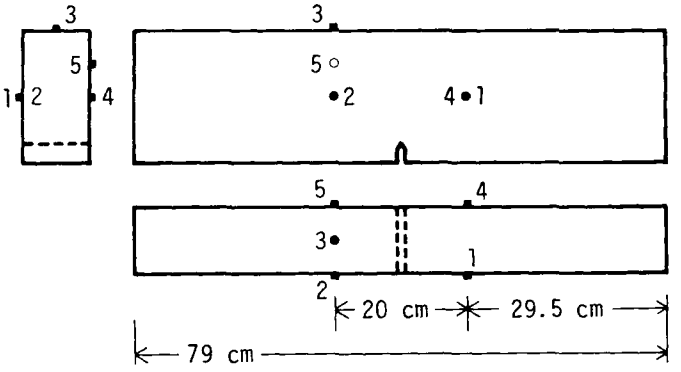

Fig. 2.17. Position of Pick-ups on Beam AE-2.

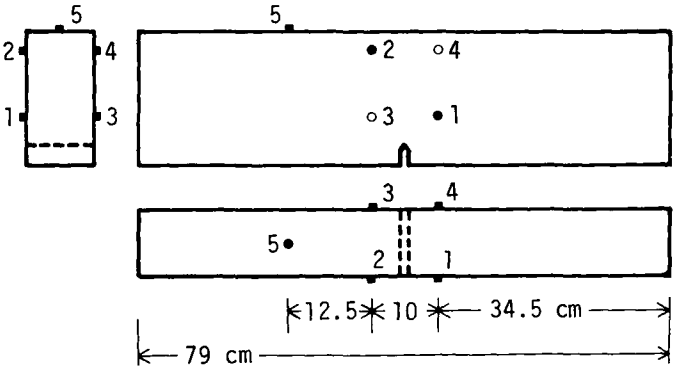

Fig. 2.18. Position of Pick-ups on Beam AE-3.

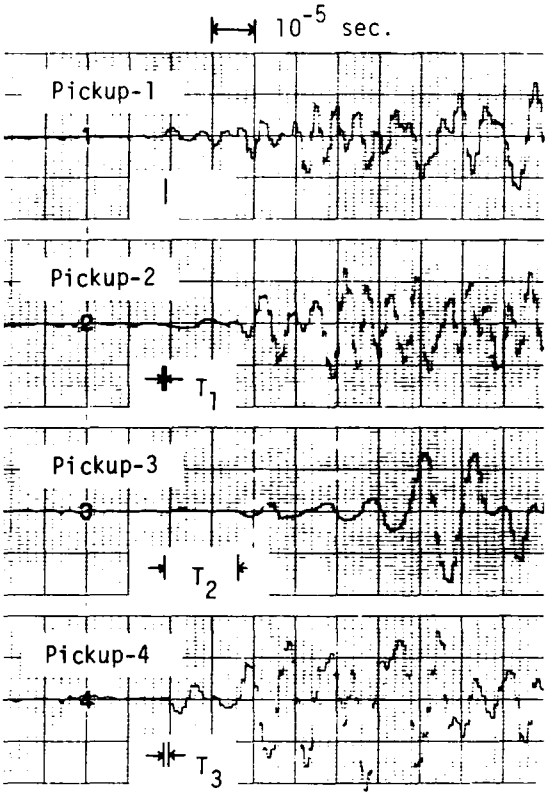

Fig. 2.19. Example of Recorded AE Waves.

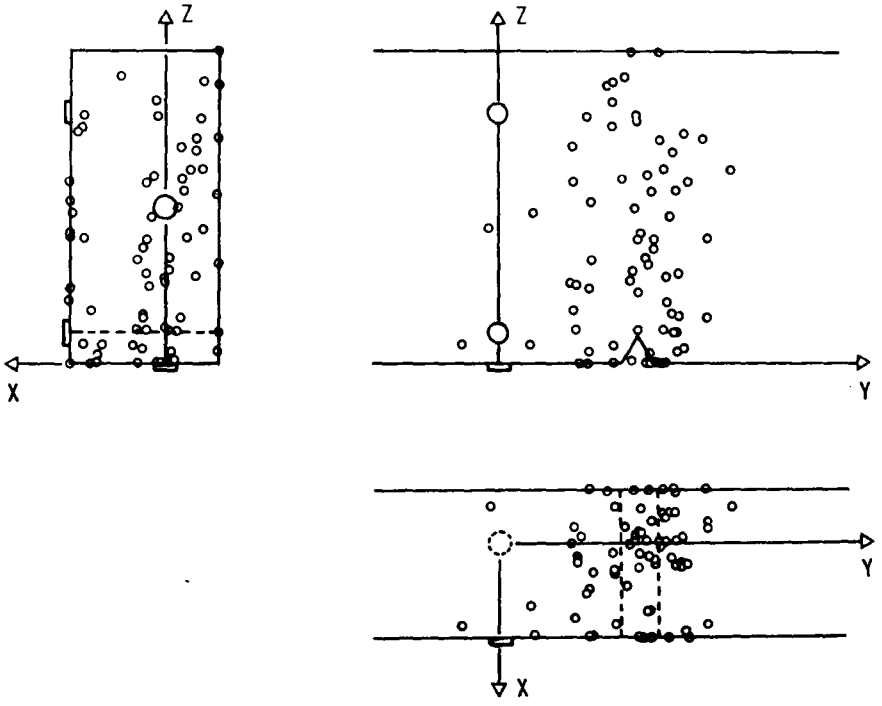

Fig. 2.20. AE Sources in Beam AE-1.

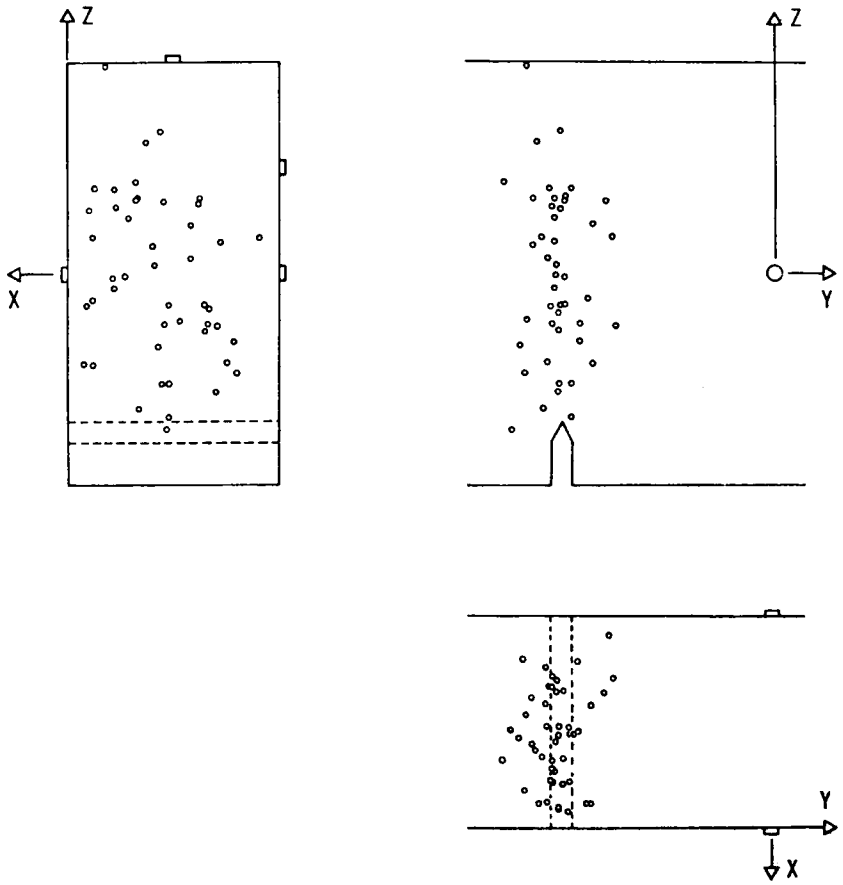

Fig. 2.21. AE Sources in Beam AE-2.

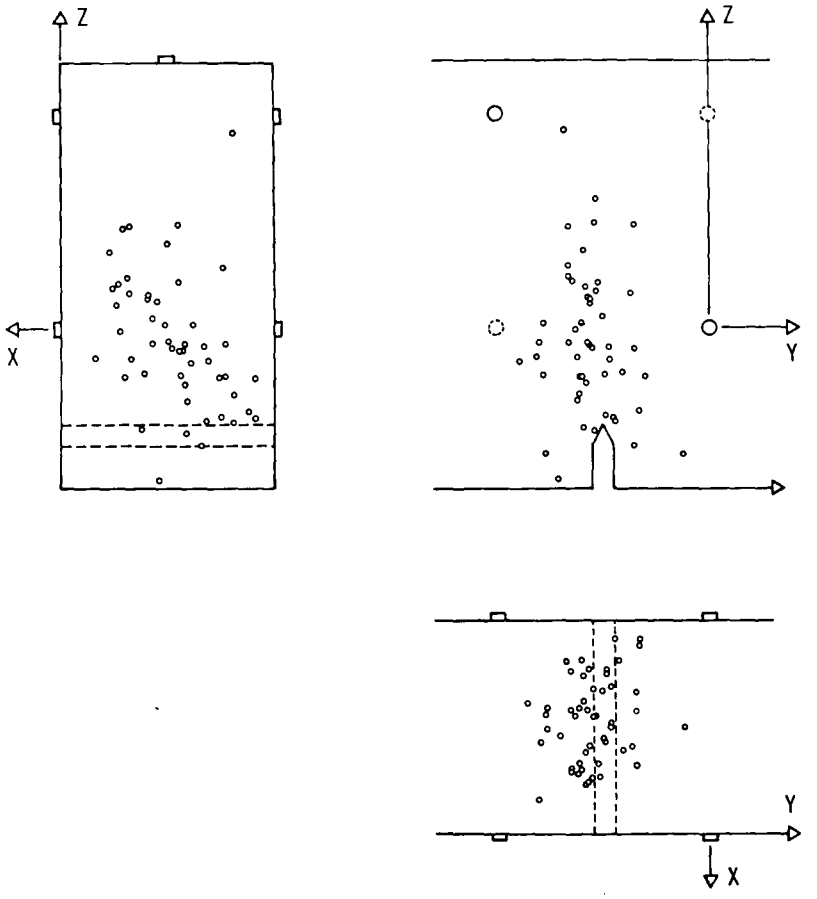

Fig. 2.22. AE Sources in Beam AE-3.

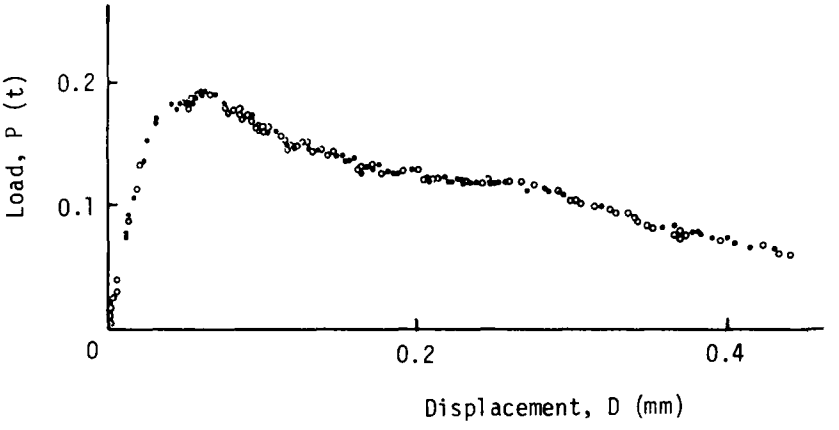

Fig. 2.23. Order of AE Generation in Beam AE-1.

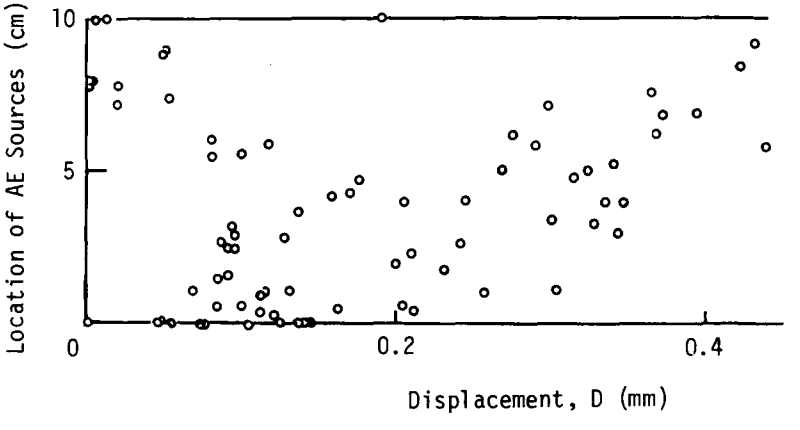

Fig. 2.26. Beam Displacement and Location of AE Sources in Beam AE-1.

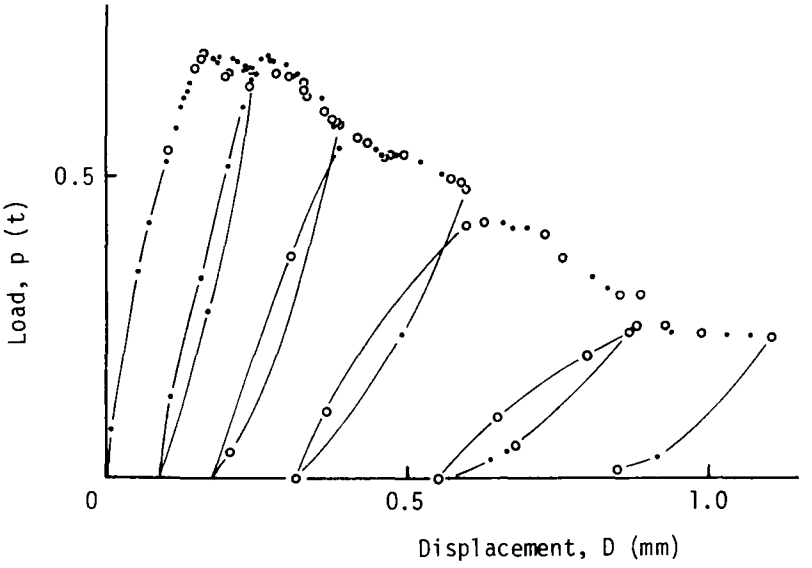

Fig. 2.24. Order of AE Generation in Beam AE-2.

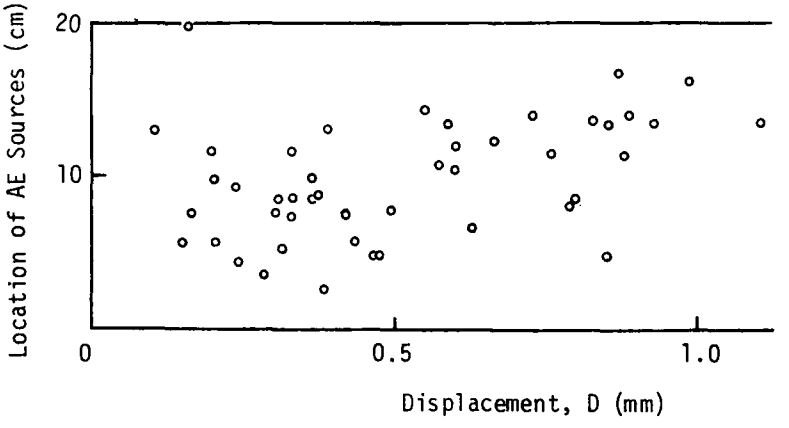

Fig. 2.27. Beam Displacement and Location of AE Sources in Beam AE-2.

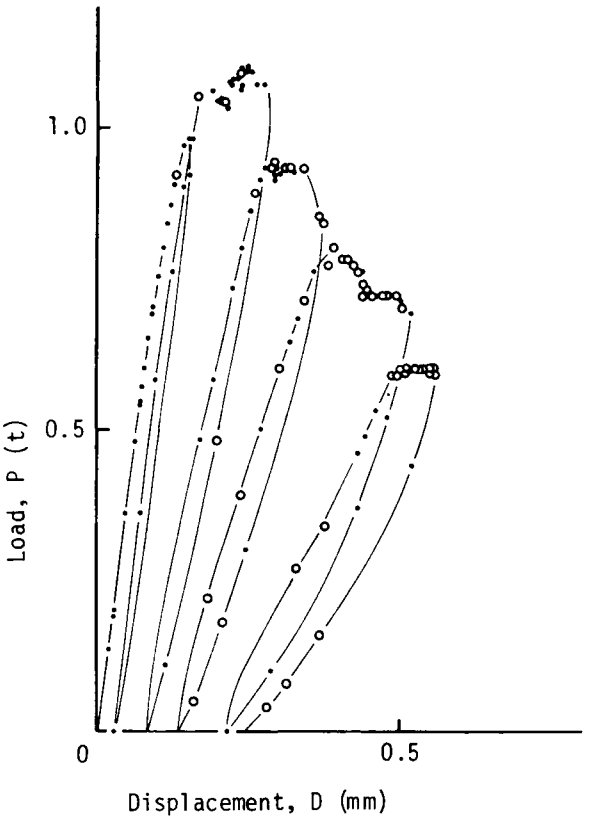

Fig. 2.25. Order of AE Generation in Beam AE-3.

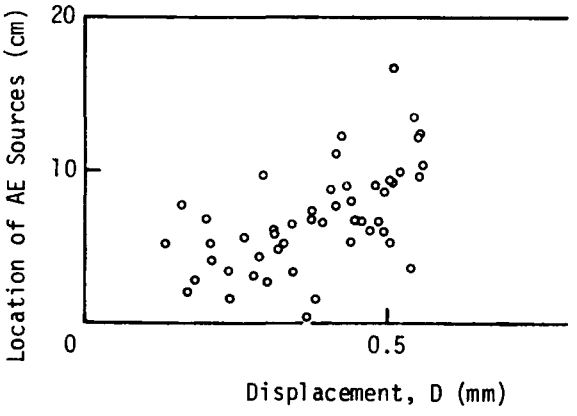

Fig. 2.28. Beam Displacement and Location of AE sources in Beam AE-3.

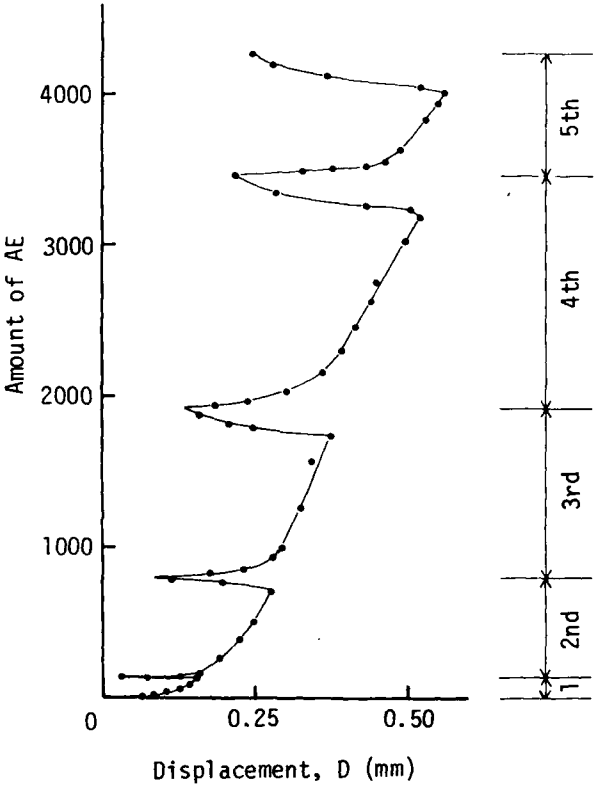

Fig. 2.29. Amount of AE and Displacement of Beam AE-3.

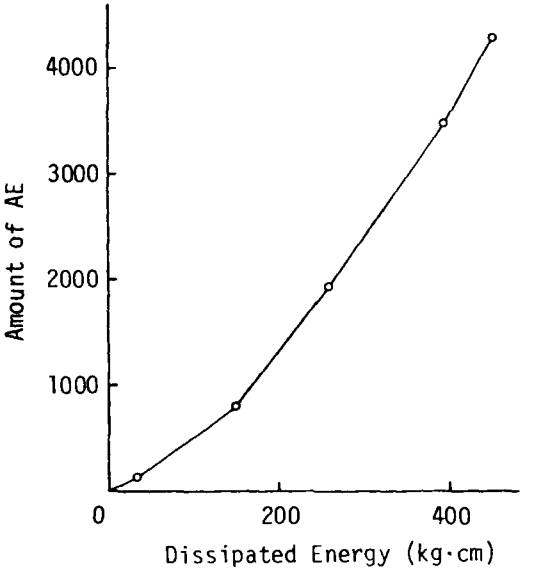

Fig. 2.30. Amount of AE and Dissipated Energy.

CHAPTER 3. EVALUATION OF FRACTURE TOUGHNESS PARAMETERS OF CONCRETE

3.1 INTRODUCTION

The fracture of concrete is generally due to the growth of internal cracks. To explain or to compare the properties of various kinds of concrete in wear, impact resistance, and cracking, a suitable criterion for the resistance capacity to crack initiation is required.

The critical stress intensity factor, K_c, and the corresponding critical energy release rate, G_c ($= K_c^2/E$), are the fracture toughness parameters used in linear-elastic fracture mechanics. They assume that the material is homogeneous, isotropic, and linear-elastic. Therefore, it is difficult to apply them to concrete, which is neither homogeneous nor linear-elastic.

The J-integral, a path independent line integral, can be applied to both linear-elastic and nonlinear-elastic materials. Thus the critical J-integral, J_c, may be considered a better parameter to describe the fracture behavior of concrete than the parameters G_c and K_c. Mindess, Lawrence and Kesler have shown that the J-integral may provide a useful quantitative measure of the benefits of fiber reinforcement for concrete [15]. This study is an extension of their preliminary work, because the experimental work was done when the author was studying under Prof. Clyde E. Kesler and Prof. Frederich V. Lawrence at the University of Illinois in U.S.A.

The two main purposes in this chapter are to find the best methods for evaluating the most meaningful and reproducible value of J_c, and to compare J_c with other fracture

toughness parameters like S, the unit dissipated energy, calculated by dividing the total absorbed energy up to rupture by the critical net section area.

It has been shown through previous studies that J_c is a promising fracture criterion for concrete and a good indicator of the effectiveness of fiber additions to concrete [15]. At this time, additional information on J_c is required to determine if the J-integral concept is truly generally applicable to concrete. The following factors regarding J_c were studied:

(1) The best experimental technique to evaluate J_c. Specifically, which technique is most reproducible, the B-method or R-method (defined in Section 3.2.5).

(2) Means of reducing scatter in the data.

(3) The influence of specimen geometry on measured values of J_c, specifically specimen size and notch size relative to aggregate size.

(4) The appropriate load to evaluate J_c, that is, whether or not the main or critical crack starts at the peak load.

To solve problems (1), (2) and (3), three specimen sizes (7.6x7.6x38.1 cm, 7.6x15.2x38.1 cm, and 10.2x15.2x50.8 cm), three notch depths (H/6, H/3 and H/2), three maximum aggregate sizes (5 mm, 10 mm and 20 mm), three concrete strengths (compressive strengths of about 180 kg/cm^2, 320 kg/cm^2, and 440 kg/cm^2), and twelve kinds of concrete including two different fiber reinforced concretes and mortar were used to evaluate J_c in this investigation.

Relative to problem (4), the result in Chapter 2 shows that cracks during the flexural fracture process of concrete propagate remarkably after the peak load. Consequently, this fact assures that J_c can be evaluated at the peak load, at least for plain concrete. In addition, it is suggested by the

result in Chapter 2 that the possibility of the occurance of a large amount of branch cracking may be quite small.

3.2 EXPERIMENTAL PROCEDURES

3.2.1 Test Series

Twelve series of beam specimens were fabricated, tested and analyzed to find the most suitable conditions for evaluating J_c and to compare J_c with other fracture toughness parameters.

Each series is designated by letters and numerals which have the following significance.

The first two letters of each name (BL-POM3) identify the specimen size.

BS --- Small size beam specimens (7.6x7.6x38.1 cm)

BM --- Middle size beam specimens (7.6x15.2x38.1 cm)

BL --- Large size beam specimens (10.2x15.2x50.8 cm)

The second series of the letter and the numeral (BL-POM3) identify the type of mix.

PO --- Plain concrete

MO --- Mortar

F1 --- Steel fiber reinforced concrete, containing 1% fibers (by volume)

F2 --- Steel fiber reinforced concrete, containing 2% fibers (by volume)

The fifth letter (BL-POM3) indicates the compression strength of the mortar and concrete.

L --- Low strength concrete
f_c = 180 kg/cm^2

M --- Middle strength concrete
f_c = 320 kg/cm^2

H --- High strength concrete

$$f_c = 440 \text{ kg/cm}^2$$

The last numeral (BL-POM3) designates the maximum size of coarse aggregate.

3 --- 10 mm (3/8 in.)

6 --- 20 mm (6/8 in.)

0 --- no coarse aggregate

The letters and numerals after the hyphen indicate the character of the concrete mix. Test conditions for each of these series are tabulated in Table 3.1.

3.2.2 Materials and Mix Proportions of Concrete

Ordinary Portland cement was used in all the series except the BM-POH3 series, where high early strength Portland cement was used.

Dry river gravel (specific gravity: 2.60, water absorption: 2.2%) and dry river sand (specific gravity: 2.60, water absorption: 2.0%) were used. The maximum size of coarse aggregate was 20 mm for the series BS-POM6, BM-POM6, BL-POM6, and BM-POH6, and was 10 mm for the rest of the series.

Steel fiber (size: 0.25x0.56x25.4 mm, aspect ratio: 60) was used with a water-reducer (Lubricon 200) and an air -entraining admixture (Amex) in series BM-F1M3 and BM-F2M3.

The mix proportions and measured slumps, and air content are presented in Table 3.2.

3.2.3 Fabrication of Specimens

A two cubic foot mixer was used. For plain concrete and mortar, the dry materials were blended for approximately one minute before water was added. Mixing was then continued for approximately three minutes.

For fiber reinforced concrete, fibers were added in the mixing bowl during dry mixing through a vibrating screen and chute. The water-reducing and air-entraining agents were

each put in different halves of the mix water. The water containing the water-reducer was added first.

Each test series consists of more than four cylindrical specimens and 20 beams, five of which are unnotched beams, and five each of which are H/6* -notched, H/3-notched, and H/2-notched beams. All specimens of each series were cast at one time from several batches of concrete. To make a notch, a steel plate, shown in Fig. 3.1, was attached to the mold wall with instantaneous glue (Cyano-acrylate). Concrete in the mold was compacted by rodding and vibration.

On the day following casting, the specimens were unmolded, and the notch plates were removed. The specimens were cured in water until tested.

3.2.4 Testing Procedures

A screw type loading machine was used for the flexure tests. The beams were tested under third-point loading on a 46.7 cm span for the 10.2x15.2x50.8 cm beams and on a 34.3 cm span for the 7.6x7.6x38.1 cm and 7.6x15.2x38.1 cm beams. The beams were tested so that the tension side (notch side) was on top to reduce the moment due to specimen's weight itself. A picture of the test setup is shown in Fig. 3.2. Specimens were tested while saturated.

The load was measured with a load cell incorporated in the machine head. Load-point displacements and center-point displacements were measured by three linear variable differential transformers (LVDT) as shown in Fig. 3.2. The center-point displacement was measured 6 mm from the specimen's center line. The load-point displacements were measured by

---

* H/6 indicates that the beam was notched 1/6 of its height, H, starting from the tension surface; similarly for H/3 and H/2.

two LVDT and averaged. The displacement measuring apparatus with three LVDT was attached directly to the concrete beam to eliminate seating effects. The fixed points of the apparatus were designed to be rotatable and slidable. Therefore, large deflections up to the complete rupture of the concrete beam could be measured.

A load/load-point displacement diagram and a load/center-point displacement diagram were recorded on X-Y recorders for each beam. The rate of the load-point displacement was approximately 0.5 mm/min. for fiber concrete, and 0.05 mm/min. for other concretes.

Compressive strength was determined from ϕ10x20 cm cylindrical specimens.

3.2.5 Evaluation of Toughness Parameters

In this investigation, J_c, the critical J-intergral, was evaluated by two methods: the R-method, which was proposed by Rice, Paris and Merkle [10], and the B-method, which was proposed by Begley and Landes [9]. J_{cr}, J_c by the R-method, and J_{cb}, J_c by the B-method, were compared with G_c, the critical energy release rate, and S, the nominal unit dissipated energy. The methods for evaluating these toughness parameters are explained in this section.

The critical point for evaluating J_c is assumed to be the peak load point on the load-displacement diagram of a notched beam, based on the result in Chapter 2.

The B-method for calculating J_c from beams is illustrated in Fig. 3.3. For each load-deflection curve, the energy required to deflect the specimen to D_1, D_2, D_3 is determined and plotted against crack length a_1, a_2, a_3 for the different values of displacement. The J-integral is defined as the negative slope of any line in Fig. 3.3 (b). J_c is found at the point where critical displacement occurs, that is, at the

peak load point for concrete.

When the number of different notch depths is small, it is often difficult to find only one curve in W_t-a diagrams like Fig. 3.3 (b). In such sases, the selection of curves causes significant errors. In this study, three different notch depths were used. Therefore, the B-method was modified as illustrated in Fig. 3.4. In Fig. 3.4, J_{cb} from a H/6-depth notched beam is calculated from the line AB, J_{cb} from a H/3-depth notched beam is evaluated from the line parallel with DF, and so on.

In general, the results from concrete specimens have a larger scatter than those from metal specimens. So in this study, five beams were allocated for each test condition and the graphical average of the five load-displacement diagrams was used to evaluate J_c. The procedure of averaging diagrams is described in Section 3.4.

In the R-method, if the elastic energy stored in the beam is not negligible, it must be eliminated from the potential energy. The elastic energy can be determined from the load-deflection curve of the unnotched beam. Zaveri [51] has shown a graphical solution method as illustrated in Fig. 3.5.

K_c, critical stress intensity factor, and G_c, critical energy release rate, are given as:

$$K_c = f_m \, a \, F(a/H) \tag{3.1}$$

$$G_c = K_c^2/E \quad \text{..... for plane stress} \tag{3.2}$$

$$= K_c^2 \, (1 - \nu^2)/E \text{..... for plane strain} \tag{3.3}$$

$$F(a/H) = 1.122 - 1.40(a/H) + 7.33(a/H)^2 - 13.08(a/H)^3 +$$

$14.0(a/H)^4$ ..... for pure bending (3.4)

K_c and G_c are functions of f_m, the critical tensile stress. They are not explicitly affected by the strain distribution.

The nominal unit dissipated energy, S, can be obtained by dividing the total work done at complete rupture by the ligament section area:

$$S = W_{tf}/(Bb) \tag{3.5}$$

For the linear elastic case, S is equivalent to G_c, the critical energy release rate, so that:

$$S = G_c = J_c \tag{3.6}$$

J_c is considered to represent the ability to resist strength failure in flexure, and S the energy absorbing capacity in flexure. For concrete, S includes the energy dissipation due to branch cracking, viscous friction, etc. Therefore, the relation between S and J_c may indicate the degree of brittleness of the concrete during the fracture process.

3.3 TEST RESULTS AND SCATTER

The compressive strength f_c, modulus of rupture f_r, net section modulus of rupture f_{rn}, gross section modulus of rupture f_{rg}, and ratios f_{rn}/f_r and f_{rg}/f_r are tabulated in Table 3.3.

Load-point displacement at the peak load D_p, center-point displacement at the peak load D_{cp}, potential energy at the peak load W_{tp}, total work done at complete rupture W_{tf}, and ratios D_p/D_{cp} and W_{tp}/W_{tf} are presented in Table 3.4.

The results in Tables 3.3 and 3.4 are expressed in sets of average values, with the number of spcimens and the

coefficient of variation (COV) in parentheses.

As seen from Tables 3.3 and 3.4, COV of P_p and D_p decreased with an increase in specimen size and concrete strength, and with a decrease in maximum aggregate size. But the influence of specimen size on the values of f_{rn} and f_{rg} was small.

COV of W_{tp} for the middle size beams (7.6x15.2x38.1 cm) was smaller than that for the other size beams. W_{tp} was used to calculated J_c.

For the fiber reinforced concretes (BM-F1M3 and BM-F2M3), COV of P_p, f_{rn} and f_{rg} were not markedly different from those for plain concretes, but COV of D_p and W_{tp} were considerably higher than those for plain concretes.

The relations between the ratio D_p/D_{cp} and notch depth for plain concrete and fiber reinforced concrete are shown in Fig. 3.6. The relationships of plain concretes are expressed by an averaged value with both extreme values shown.

On the other hand, for a linear-elastic unnotched beam, the load-point displacement D, practical center-point displacement D_c (measured at a point 6 mm from the center line), and actual center-point displacement D_{cc} are given as:

$$D = 20\Phi L^2/216 \tag{3.7}$$

$$D_{cc} = 23\Phi L^2/216 \tag{3.8}$$

$$D_c = 1103\Phi L^2/10368 \quad \text{.....for L=45.7 cm} \tag{3.9}$$

$$= 310\Phi L^2/2916 \quad \text{.....for L=34.3 cm} \tag{3.10}$$

Hence,

$$D/D_{cc} = 20/23 = 0.8696$$

$$D/D_c = 0.8704 \quad \text{..... for L=45.7 cm}$$

$$= 0.8710 \quad \text{..... for L=34.3 cm}$$

If there is rotation due to the presence of a notch, θ_n:

$$D = 20\Phi L^2/216 + \theta_n L/4 \tag{3.11}$$

$$D_{cc} = 23\Phi L^2/216 + \theta_n L/6 \tag{3.12}$$

When $\Phi = 0$ and $\theta_n \neq 0$:

$$D/D_{cc} = 2/3 = 0.67$$

Therefore, the lower boundary of D/D_c is 0.67 and the upper boundary is 0.87. The ratio must fall between these values, which are marked in Fig. 3.6.

As seen from Fig. 3.6, the ratio D_p/D_{cp} decreases with an increase in notch depth. That is, Φ decreases and θ_n increases with an increase in notch depth.

The averaged value of D_p/D_{cp} for unnotched plain concrete beams was almost equal to the upper boundary. But the values for the unnotched fiber reinforced concrete beams were less than the upper boundary. For the fiber reinforced concretes, nonlinear deformation near the peak load level may cause the additional curvatures as illustrated in Fig. 3.7 and this decreases the value of D_p/D_{cp} of the unnotched beams.

For the notched beams, the ratio D_p/D_{cp} of the fiber reinforced concretes was lower than that of the plain concretes. This means that the rotation due to a notch, θ_n, in the fiber reinforced concretes was greater than that occuring in the plain concretes.

The relation between the ratio f_{rn}/f_r and the notch depth is given in Fig. 3.8. Though the ratio is not constant with

the change in notch depth, there was a tendency for the ratio to decrease with an increase in concrete strength and with a decrease in maximum aggregate size and fiber content. Two percent fiber reinforced concrete (BM-F2M3) was not notch -sensitive for an H/6-depth notch.

The net section modulus of rupture, f_{rn}, of the 2% fiber reinforced concrete (BM-F2M3) was about 20% higher than those of the plain concretes with almost the same compressive strength. But f_{rn} of the 1% fiber reinforced concrete (BM-F1M3) had not increased as much.

3.4 LOAD-DISPLACEMENT DIAGRAM

Properties of the load-displacement diagrams and their treatment are discussed in this section.

The load-displacement diagrams of the plain concrete H/3-notched beams (BM-P0M3) and the 1% fiber reinforced concrete beams (BM-F1M3) are shown in Figs. 3.9 and 3.10. As seen from these figures, the load-displacement diagrams obtained from the beams under the same test conditions were not identical. The scatter in the diagrams cannot be ignored. Therefore, representative diagrams must be used for comparing diagrams of different test conditions or calculating J_c. Five beam specimens were tested for each test condition. The representative diagram represents a graphical average of all the diagrams in a particular test condition group, as in Section 2.3.

The envelope curve can be considered identical to the normal load-displacement diagram. Therefore, the representative diagram was obtained from diagrams including the envelope curves.

The representative load-displacement diagrams of H/3-

notched beams from BM-P0M3 and BM-F1M3 series are shown in Figs. 3.11 and 3.12. These diagrams are simply called load -displacement diagrams. The load-point displacement at the peak load, D_p, of plain concretes tended to decrease as the notch depth decreased. The negative slope of the falling branch in the diagrams became gentler as the notch depth increased.

The modulus of elasticity, E, was computed from the initial slope up to the $P_p/3$ point on the load-displacement diagrams of the unnotched beams. E values for all series are given in Table 3.5. They were almost identical with the usual values which would be measured from compression tests with strain gages. In the diagrams for unnotched beams, the initial curves were nearly straight from the origin up to the point of about half the peak load. Consequently, in the calculation of J_{cr}, the calculated potential energy can be substituted for the measured energy of unnotched beams.

The load-displacement diagram of each series continues until the complete rupture point. Displacements at the complete rupture point, D_f, are also given in Table 3.5. D_f was about 20 times larger than D_p for plain concretes. D_f values for the fiber reinforced concretes (BM-F1M3 and BM-F2M3) were so great (over the capacity of the displacement measuring apparatus of about 7.5 mm), that D_f and the final portion in the diagrams had to be extrapolated. However, the error in W_{tf} due to this assumption is less than 10%.

The load-displacement diagrams were normalized by the peak load and the peak load point displacement, and are shown in Figs. 3.13, 3.14 and 3.15. These figures indicate that the load rapidly decreased after the peak load when the maximum aggregate size was small or the concrete strength was

high. Plain concretes lost their load carrying capacity more rapidly after the peak load than did fiber concretes. These trends can be explained by the crack arresting effects of the steel fiber and aggregate.

Figure 3.16 shows the relation between the ratio W_{tp}/W_{tf} in Table 3.4 and the maximum negative slope in the load -displacement diagrams. As the ratio W_{tp}/W_{tf} increased, the maximum negative slope increased. The behavior of the specimen after the peak load can be explained by the ratio W_{tp}/W_{tf}.

3.5 BEST TECHNIQUE FOR EVALUATING J_c

The B-method and R-method for evaluating J_c are compared and the influence on J_c of specimen size and notch depth is investigated in this section.

J_{cb} and J_{cr} under each test condition were measured by the B-method and R-method, respectively. The relation between the potential energy and the notch depth for evaluating J_{cb} is shown in Figs. 3.17 and 3.18. J_{cb}, J_{cr}, and the ratio J_{cb}/J_{cr} are given in Table 3.6. The averaged J_{cb} and J_{cr} for each test series and the ratio J_{cb}/J_{cr} are shown in Table 3.7. For all series, J_{cr} from H/3-notched beams and H/2-notched beams were almost equal. But J_{cr} values from H/6-notched beams were about 15% lower, except for the BM-F2M3 series. With an increase in the notch depth, J_{cb} tended to decrease and to approach the value of J_{cr}. For H/3-notched beams, J_{cb} was about 1.5 times larger than J_{cr}. J_{cb} was affected more by notch depth than J_{cr}. In terms of the notch depth effect, the R-method was superior to the B-method.

Generally speaking, the aggregate size in the concrete is large compared to the size of the notched beam specimen,

so it is desirable to have the critical section area as large as possible. Moreover, the ratio of the tensile strength to the specimen weight for concrete specimens is much smaller than that of metal specimens. Hence, special care is needed in handling the deeply notched beams. For these reasons, the notch depth of concrete beam specimens should be less than half of the specimen's depth.

As described above, values of J_{cr} from H/3-notched beams were almost equal to those from H/2-notched beams. And, as described in Section 3.3, COV of W_{tp} for H/3-notched beams was smallest. For these reasons, H/3-notch depth was most suitable for J_c evaluation by the R-method.

For standard tests of concrete properties like f_r and J_c, 7.5x7.5x30 cm beams may be the lower limit in specimen size with regard to the aggregate size, and 15x15x60 cm beams may be the upper limit with regard to the weight. One 15x15x60 cm concrete beam weighs about 32 kg, so that if the specimen is larger than that, special tools are required to handle it and it is difficult to test several specimens for each test condition. Therefore, the specimen size should be between these lower and upper limits.

Though this study includes only three specimen sizes (7.6x7.6x38.1 cm, 7.6x15.2x38.1 cm and 10.2x15.2x50.8 cm), the results indicated that J_{cr} was independent of specimen dimensions in such a small range of specimen sizes. The COV of W_{tp} for the 7.6x15.2x38.1 cm beams was smallest, so that 7.6x15.2x38.1 cm beams were more suitable for J_{cr} evaluation than the other size beams. Furthermore, to find the best testing conditions, additional information about the following factors is needed:

1) Rate of loading

2) Span-depth ratio, L/H
3) Notch thickness
4) Notch sharpness
5) Notching method
   Saw cut, cast in place with steel insert removed, cast in place with plexiglass insert remaining in place
6) Loading method
   Third point bending or center point bending
7) Specimen type
8) Relative stiffness of the test machine

3.6 OTHER FRACTURE TOUGHNESS PARAMETERS

The purpose of this section is to compare J_c with other fracture toughness parameters like S and G_c.

The nominal unit dissipated energy, S, critical stress intensity factor, K_c, and critical strain energy release rate, G_c, are also given in Tables 3.6 and 3.7. The ratios S/J_{cr} and G_c/J_{cr} are also shown in Table 3.7.

Table 3.7 indicates that S was about 4.5 times greater than J_{cr}. One of the reasons may be that the actual fracture surface was so rough due to crack arrests by aggregate and steel fiber, that the actual area was several times larger than the nominal net section area.

Though there was a tendency for S to be the largest for H/2-notched beams and the smallest for H/3-notched beams, the effect of the notch depth on S was relatively small.

The relationship between the concrete strength and the fracture toughness parameters, S and J_c, is shown in Figs. 3.19 and 3.20. As the concrete strength increased, J_c also increased but S was almost constant. It was observed that

the actual fracture surface flattened as the concrete strength increased. It seemed that as the concrete strength increased, the actual surface energy increased but the actual fracture surface area decreased, so that the total energy dissipation was not changed.

The relations between the steel fiber content and the fracture toughness parameters, J_c, S, and G_c, are shown in Fig. 3.21. For the steel fiber concrete, J_c and S were much larger than those of the plain concrete, but G_c was almost constant. Thus, J_c and S would be better parameters than G_c for the purpose of evaluating the effectiveness of steel fiber addition. S, especially, was more sensitive than J_c for a steel fiber content of 1%.

The relationship between the maximum aggregate size and the parameters S and J_c are given in Fig. 3.22. Both S and J_c increased with an increase in the maximum aggregate size.

As seen from Tables 3.6 and 3.7, G_c increased with an increase in the concrete strength and the maximum aggregate size. This trend was similar to the trend of J_c. But as previously reported [15], the effectiveness of steel fiber in concrete cannot be explained by means of G_c. G_c is calculated from the peak load and the initial slope on the load-displacement diagrams, so G_c cannot be applied to a material like steel fiber reinforced concrete, which shows large plasticity at high load level.

The relationship between the ratios f_{rn}/f_r and J_{cr}/f_r is shown in Fig. 3.23. The ratio f_{rn}/f_r is a parameter of notch-sensitiveness. There was a correlation between the ratios f_{rn}/f_r and J_{cr}/f_r. Therefore fracture toughness could be roughly evaluated by the notch-sensitiveness parameter, f_{rn}/f_r, without any displacement measurement during loading tests.

3.7 CONCLUSION

The best procedure to evaluate the most meaningful and reproducible value of J_c was investigated. J_c was compared with other fracture toughness parameters.

Twelve series of tests including concrete, mortar, and 1% and 2% fiber reinforced concretes were made. Three specimen sizes (7.6x7.6x38.1 cm, 7.6x15.2x38.1 cm, and 10.2x15.2x50.8 cm), three notch depths (H/6, H/3, and H/2), three maximum aggregate sizes (5 mm, 10 mm, and 20 mm), and three concrete strengths (compressive strengths of about 180 kg/cm^2, 320 kg/cm^2, and 440 kg/cm^2) were included in the study.

The results of this study can be summarized as follows:

(1) For all series, J_{cr} from both the H/3-notched beams and H/2-notched beams were almost equal. But the value of J_{cb} was influenced by notch depth. In the case of the H/3-notched beams, J_{cb} was about 1.5 times larger than J_{cr}. In terms of notch depth sensitivity, the R-method was superior to the B-method.

(2) The scatter of W_{tp} for the H/3-notched beams was smallest. J_{cr} was calculated from W_{tp}. Generally, shallowly notched concrete beams are easier to handle than deeply notched beams. Therefore, the H/3 notch depth was the most suitable one with which to evaluate J_c by the R-method.

(3) Though this investigation includes only three specimen sizes, the results indicated that J_{cr} is independent of specimen dimensions. The scatter of W_{tp} for 7.6x15.2x 38.1 cm beams was smallest. Therefore, the 7.6x15.2x 38.1 cm beams are more suitable for the evaluation of J_{cr}.

(4) The moduli of elasticity, E, which were computed from

the load-displacement diagrams of unnotched beams, were almost identical with the usual values which would be obtained from compression tests with strain gages. In the load-deflection diagrams for the unnotched beams, the initial curves were nearly straight from the origin to a point at about one-half of the peak load. Therefore, in the calculation of J_{cr}, the calculated potential energy can be substituted for the one measured in the unnotched beams.

(5) The nominal unit dissipated energy, S, was about 4.5 times greater than J_{cr}. One of the reasons may be that the actual fracture surface was so rough, due to the redirecting of cracks by the aggregate and steel fibers, that the actual area was several times larger than the nominal net section area.

(6) As the concrete strength increased, J_c also increased but S was almost constant. It was observed that the actual fracture surface approached a plane surface as the concrete strength increased. It seemed that with this increase in strength, the actual surface energy increased but the actual fracture surface area decreased, so that the total energy dissipation was not changed.

(7) J_c and S remarkably increased with an increase in the fiber content, but G_c was almost constant. Therefore, J_c and S are better parameters than G_c for evaluating the effectiveness of steel fiber addition. S, especially, is more sensitive than J_c for a small amount of steel fiber content.

(8) As the ratio W_{tp}/W_{tf} increased, the negative maximum slope of the load-deflection diagram increased. The behavior of the specimen after the peak load can be ex-

plained by the ratio W_{tp}/W_{tf}.

(9) The ratio f_{rn}/f_r is a parameter of notch-sensitiveness. There was a correlation between the ratios f_{rn}/f_r and J_{cr}/f_r. Therefore, fracture toughness could be evaluated roughly by the notch-sensitiveness parameter, f_{rn}/f_r, without any displacement measurement during loading tests.

Table 3.1. Test Conditions.

Series	Specimen Size mm	Type of Concrete	Steel Fiber Content % (volume)	Compressive Strength kg/cm^2	Maximum Aggregate Size mm
BS-POM3	76x76x381*	Plain	0	320	10
BM-POM3	76x152x381	Plain	0	320	10
BL-POM3	102x152x508	Plain	0	320	10
BS-POM6	76x76x381	Plain	0	320	20
BM-POM6	76x152x381	Plain	0	320	20
BL-POM6	102x152x508	Plain	0	320	20
BM-POH3	76x152x381	Plain	0	440	10
BM-POH6	76x152x381	Plain	0	440	20
BM-POL3	76x152x381	Plain	0	180	10
BM-MOMO	76x152x381	Mortar	0	320	10
BM-F1M3	76x152x381	Fiber	1	320	10
BM-F2M3	76x152x381	Fiber	2	320	10

*Height, width and length.

Table 3.2. Mix Proportions.

Mix	Water-Cement Ratio	Sand-Aggr. Ratio	Mix Materials, kg/m^3								Slump, cm	Air, %
						Gravel, mm			Admixture,			
			Water	Cement	Sand	5~10	10~20	Fiber	AEA	WR		
POM3	0.54	0.56	171	314	1016	804	-	-	-	-	11	4.2
POM6	0.47	0.43	138	291	839	126	983	-	-	-	10	2.7
POH3	0.51	0.55	179	354	976	796	-	-	-	-	11	3.3
POH6	0.47	0.43	139	294	847	127	993	-	-	-	10	2.5
POL3	0.72	0.57	181	253	1043	789	-	-	-	-	10	4.2
MOMO	0.53	-	209	391	1568	-	-	-	-	-	5.5	6.0
F1M3	0.47	0.50	151	322	857	857	-	78.3	0.30	0.74	12	6.4
F2M3	0.50	0.50	174	346	803	803	-	156	0.30	0.74	11.5	6.1

Table 3.3. Strength of Concrete.

Series	Compressive Strength f_c, kg/cm^2	Notch Depth a, cm	Peak Load p_p, kg	Modulus of Rupture f_r, kg/cm^2	Net Section Mod. of Rup. f_{rn}, kg/cm^2	Gross Section Mod. of Rup. f_{rg}, kg/cm^2	$\frac{f_{rn}}{f_r}$	$\frac{f_{rg}}{f_r}$
BS-POM3	314 (4, 4.2%)	0.0	663 (5*, 5.3%**)	50.5 (5, 5.4%)				
		1.27	398 (5, 2.7%)		43.0 (5, 2.9%)	30.0 (5, 3.0%)	0.852	0.593
		2.54	260 (5, 6.8%)		43.9 (5, 10.7%)	19.4 (5, 9.7%)	0.855	0.384
		3.81	158 (5, 8.0%)		44.6 (5, 5.2%)	11.6 (5, 5.5%)	0.884	0.230
BM-POM3	303 (3, 1.9%)	0.0	1343 (5, 4.5%)	50.3 (5, 4.3%)				
		1.27	792 (5, 4.3%)		42.0 (5, 4.7%)	29.3 (5, 4.5%)	0.835	0.582
		2.54	580 (5, 4.9%)		47.2 (5, 5.2%)	21.4 (5, 5.1%)	0.939	0.425
		3.81	331 (5, 2.8%)		47.0 (5, 1.0%)	12.2 (5, 1.4%)	0.934	0.242
BL-POM3	320 (4, 3.4%)	0.0	1735 (4, 1.8%)	49.0 (4, 0.9%)				
		1.69	1035 (5, 3.3%)		42.0 (5, 3.3%)	29.2 (5, 3.3%)	0.857	0.595
		3.39	684 (5, 3.2%)		42.2 (5, 2.0%)	19.0 (5, 1.9%)	0.861	0.387
		5.08	394 (5, 6.3%)		43.0 (5, 4.6%)	11.0 (5, 5.1%)	0.878	0.224
BS-POM6	322 (4, 2.8%)	0.0	701 (5, 8.4%)	52.2 (5, 8.2%)				
		1.27	428 (5, 11.5%)		46.8 (5, 11.3%)	32.5 (5, 11.3%)	0.900	0.623
		2.54	292 (5, 7.6%)		47.5 (5, 4.3%)	21.5 (5, 5.1%)	0.910	0.412
		3.81	169 (5, 7.6%)		50.0 (5, 8.2%)	12.7 (5, 7.7%)	0.958	0.243
BM-POM6	305 (3, 2.8%)	0.0	1292 (5, 2.9%)	47.1 (5, 1.7%)				
		1.27	893 (5, 5.1%)		47.2 (5, 5.4%)	33.0 (5, 5.3%)	1.003	0.701
		2.54	575 (5, 6.0%)		47.3 (5, 5.5%)	21.4 (5, 5.7%)	1.004	0.454
		3.81	307 (5, 2.7%)		43.9 (5, 3.0%)	11.3 (5, 2.8%)	0.931	0.240
BL-POM6	321 (4, 1.3%)	0.0	1745 (5, 2.0%)	48.7 (5, 1.8%)				
		1.69	1139 (5, 4.9%)		45.6 (5, 4.0%)	31.8 (5, 4.1%)	0.935	0.652
		3.39	751 (5, 7.6%)		45.3 (5, 7.0%)	20.6 (5, 7.2%)	0.931	0.423
		5.08	392 (5, 14.7%)		42.3 (5, 13.5%)	10.9 (5, 14.1%)	0.867	0.224

*Number of specimens. **Coefficient of variation.

Table 3.3. (continued)

Series	Compressive Strength f_c, kg/cm^2	Notch Depth a, cm	Peak Load p_p, kg	Modulus of Rupture f_r, kg/cm^2	Net Section Mod. of Rup. f_{rn}, kg/cm^2	Gross Section Mod. of Rup. f_{rg}, kg/cm^2	$\frac{f_{rn}}{f_r}$	$\frac{f_{rg}}{f_r}$
BM-POH3	447 (5, 5.7%)	0.0	1633 (5*, 3.9%**)	59.8 (5, 3.4%)				
		1.27	913 (5, 5.0%)		48.0 (5, 4.8%)	33.6 (5, 4.8%)	0.803	0.562
		2.54	592 (5, 5.2%)		48.9 (5, 4.6%)	20.1 (5, 4.8%)	0.817	0.369
		3.81	357 (5, 5.6%)		49.0 (5, 4.4%)	12.9 (5, 4.4%)	0.819	0.216
BM-POH6	439 (4, 3.9%)	0.0	1603 (5, 7.3%)	58.5 (5, 6.7%)				
		1.27	1050 (5, 5.2%)		55.0 (5, 4.1%)	38.5 (5, 4.2%)	0.940	0.657
		2.54	638 (5, 6.9%)		51.5 (5, 5.5%)	23.3 (5, 5.9%)	0.881	0.399
		3.81	374 (5, 5.5%)		51.8 (5, 5.0%)	13.6 (5, 5.3%)	0.886	0.232
BM-POL3	179 (4, 6.5%)	0.0	972 (5, 10.2%)	36.1 (5, 10.0%)				
		1.27	635 (5, 6.1%)		33.3 (5, 5.1%)	23.3 (5, 5.2%)	0.922	0.646
		2.54	399 (5, 5.1%)		32.8 (5, 5.3%)	14.8 (5, 5.2%)	0.907	0.411
		3.81	239 (5, 6.0%)		32.7 (5, 5.5%)	8.72(5, 6.9%)	0.905	0.241
BM-MOMO	317 (4, 2.9%)	0.0	1295 (5, 2.8%)	48.9 (5, 3.2%)				
		1.27	724 (5, 4.7%)		38.6 (5, 4.0%)	27.0 (5, 4.2%)	0.789	0.552
		2.54	480 (5, 2.9%)		40.4 (5, 3.5%)	18.1 (5, 3.1%)	0.825	0.371
		3.81	280 (5, 4.9%)		39.9 (5, 2.7%)	10.4 (5, 3.4%)	0.816	0.213
BM-F1M3	315 (4, 1.7%)	0.0	1361 (5, 8.3%)	49.6 (5, 6.8%)				
		1.27	894 (5, 11.0%)		47.1 (5, 12.1%)	33.0 (5, 11.9%)	0.950	0.665
		2.54	585 (5, 1.7%)		47.3 (5, 3.4%)	21.4 (5, 2.3%)	0.955	0.433
		3.81	361 (4, 14.1%)		51.7 (4, 14.5%)	13.4 (4, 14.2%)	1.044	0.271
BM-F2M3	312 (4, 1.8%)	0.0	1593 (5, 4.3%)	59.9 (5, 4.7%)				
		1.27	1388 (5, 16.4%)		73.6 (5, 16.8%)	51.6 (5, 16.7%)	1.229	0.862
		2.54	823 (5, 11.7%)		66.1 (5, 7.8%)	30.2 (5, 9.1%)	1.103	0.504
		3.81	413 (5, 14.7%)		60.1 (5, 12.0%)	15.5 (5, 13.3%)	1.004	0.258

*Number of specimens. **Coefficient of variation.

Table 3.4. Displacement and Energy.

Series	Notch Depth a, cm	Load-Point Displacement at Peak Load D_p, x10^{-3}cm	Center-Point Displacement at Peak Load D_{cp}, x10^{-3}cm	$\frac{D_p}{D_{cp}}$	Work Done at Peak Load W_{tp}, kg·cm	Dissipated Energy at Rupture W_{tf}, kg·cm	$\frac{W_{tp}}{W_{tf}}$
BS-POM3	0.0	5.51 (4*, 21.4%**)	6.68 (4)	0.825	2.25 (5, 14.8%)	-	-
	1.27	4.19 (5, 9.8%)	5.16 (5)	0.813	1.01 (5, 14.1%)	4.39 (3)	0.230
	2.54	4.22 (5, 13.2%)	5.21 (5)	0.810	0.684(5, 19.7%)	3.28 (5)	0.208
	3.81	4.17 (5, 4.9%)	5.46 (5)	0.763	0.432(5, 9.0%)	2.00 (5)	0.214
BM-POM3	0.0	5.18 (5, 6.6%)	5.79 (5)	0.895	4.02 (5, 6.0%)	-	-
	1.27	3.78 (5, 10.9%)	4.80 (5)	0.788	1.87 (5, 11.4%)	9.25 (3)	0.202
	2.54	3.71 (5, 11.1%)	4.60 (5)	0.807	1.38 (5, 9.3%)	8.01 (5)	0.173
	3.81	3.53 (5, 7.8%)	4.95 (5)	0.713	0.776(5, 7.4%)	5.02 (5)	0.155
BL-POM3	0.0	7.32 (4, 5.7%)	8.10 (4)	0.903	7.24 (5, 6.6%)	-	-
	1.69	4.70 (5, 15.3%)	5.74 (5)	0.819	2.91 (5, 14.1%)	12.0 (5)	0.241
	3.39	4.67 (5, 3.4%)	6.05 (5)	0.773	1.98 (5, 4.1%)	10.1 (4)	0.195
	5.08	4.83 (5, 7.4%)	6.20 (5)	0.779	1.24 (5, 12.8%)	6.15 (5)	0.201
BS-POM6	0.0	5.33 (5, 14.7%)	6.17 (5)	0.864	2.23 (5, 22.0%)	-	-
	1.27	3.78 (5, 21.6%)	4.85 (5)	0.780	1.00 (5, 34.0%)	4.86 (3)	0.206
	2.54	4.17 (5, 15.5%)	5.54 (5)	0.752	0.788(5, 24.1%)	4.22 (5)	0.187
	3.81	3.68 (5, 9.7%)	4.88 (5)	0.755	0.406(5, 17.6%)	2.83 (5)	0.143
BM-POM6	0.0	4.93 (5, 18.3%)	5.72 (5)	0.862	3.72 (5, 18.4%)	-	-
	1.27	4.45 (5, 17.3%)	5.64 (5)	0.788	2.44 (5, 16.5%)	14.4 (5)	0.170
	2.54	4.11 (5, 6.0%)	5.64 (5)	0.730	1.51 (5, 12.9%)	8.78 (5)	0.172
	3.81	3.78 (5, 14.1%)	5.36 (5)	0.706	0.785(5, 14.8%)	5.37 (5)	0.146
BL-POM6	0.0	6.81 (5, 7.7%)	7.82 (5)	0.870	6.96 (5, 9.8%)	-	-
	1.69	5.38 (5, 12.3%)	6.38 (5)	0.845	3.72 (5, 10.6%)	15.8 (5)	0.235
	3.39	4.45 (5, 8.3%)	5.72 (5)	0.778	2.12 (5, 13.9%)	12.9 (4)	0.165
	5.08	4.27 (5, 20.5%)	5.94 (5)	0.718	1.15 (5, 38.2%)	7.71 (5)	0.149

*Number of specimens. **Coefficient of variation.

Table 3.4. (continued)

Series	Notch Depth a, cm	Load-Point Displacement at Peak load D_p, x10^{-3}cm	Center-Point Displacement at Peak Load D_{cp}, x10^{-3}cm	$\frac{D_p}{D_{cp}}$	Work Done at Peak Load W_{tp}, kg·cm	Dissipated Energy at Rupture W_{tf}, kg·cm	$\frac{W_{tp}}{W_{tf}}$
BM-POH3	0.0	5.66 (5*, 9.9%**)	6.60 (5)	0.858	5.27 (5, 6.3%)	-	-
	1.27	4.27 (5, 8.1%)	5.54 (5)	0.771	2.42 (5, 14.3%)	9.14 (2)	0.265
	2.54	4.19 (5, 5.6%)	5.46 (5)	0.767	1.54 (5, 8.7%)	7.43 (4)	0.208
	3.81	3.81 (5, 5.1%)	5.44 (5)	0.701	0.914(5, 9.3%)	4.33 (5)	0.211
BM-POH6	0.0	5.77 (5, 8.9%)	6.60 (5)	0.873	5.42 (5, 17.3%)	-	-
	1.27	4.42 (5, 9.5%)	5.44 (5)	0.798	2.90 (5, 13.4%)	12.9 (4)	0.224
	2.54	4.11 (5, 14.4%)	5.44 (5)	0.757	1.73 (5, 21.0%)	9.12 (5)	0.189
	3.81	3.68 (5, 10.0%)	5.05 (5)	0.729	0.908(5, 8.7%)	6.14 (5)	0.148
BM-POL3	0.0	5.51 (5, 10.5%)	6.35 (5)	0.868	3.11 (5, 5.2%)	-	-
	1.27	3.96 (4, 11.6%)	5.23 (4)	0.756	1.57 (4, 10.0%)	10.0 (4)	0.145
	2.54	3.38 (5, 26.0%)	4.34 (5)	0.778	0.881(5, 18.8%)	7.34 (5)	0.120
	3.81	3.28 (5, 14.2%)	4.93 (5)	0.665	0.535(5, 17.9%)	4.31 (5)	0.124
BM-MOMO	0.0	5.87 (5, 7.6%)	6.63 (5)	0.885	4.35 (5, 12.6%)	-	-
	1.27	3.89 (5, 10.8%)	4.72 (5)	0.823	1.66 (5, 10.5%)	6.31 (5)	0.262
	2.54	3.66 (5, 8.6%)	4.67 (5)	0.783	1.09 (5, 7.8%)	5.39 (5)	0.203
	3.81	3.76 (5, 9.9%)	5.03 (5)	0.707	0.697(5, 13.1%)	3.41 (5)	0.204
BM-F1M3	0.0	9.73 (5, 33.9%)	12.0 (5)	0.808	9.23 (5, 38.6%)	-	-
	1.27	6.99 (5, 24.1%)	9.75 (5)	0.716	4.71 (5, 36.0%)	219 (5)	0.021
	2.54	9.55 (5, 30.1%)	13.5 (5)	0.709	4.33 (5, 40.8%)	219 (5)	0.020
	3.81	9.86 (4, 56.7%)	14.1 (4)	0.699	3.01 (4, 70.6%)	137 (4)	0.022
BM-F2M3	0.0	17.4 (5, 18.0%)	21.6 (5)	0.803	22.2 (5, 20.7%)	-	-
	1.27	22.4 (5, 28.9%)	28.1 (5)	0.794	25.5 (5, 44.6%)	368 (5)	0.069
	2.54	22.1 (5, 16.5%)	29.7 (5)	0.744	14.9 (5, 20.2%)	250 (5)	0.060
	3.81	24.5 (5, 25.8%)	33.1 (5)	0.740	8.89 (5, 35.2%)	125 (5)	0.071

*Number of specimens. **Coefficient of variation.

Table 3.5. Modulus of Elasticity and Complete Failure Points.

Series	Modulus of Elasticity E, $x10^3 kg/cm^2$	Notch Depth a, cm	Displacement at Rupture D_f, $x10^{-3} cm$	$\frac{D_f}{D_p}$
BS-P0M3	293	1.27	66.5	15.6
		2.54	66.3	15.5
		3.81	63.5	15.2
BM-P0M3	333	1.27	91.9	24.3
		2.54	87.6	23.6
		3.81	89.4	25.3
BL-P0M3	309	1.69	87.4	18.7
		3.39	87.9	18.8
		5.08	93.7	19.4
BS-P0M6	354	1.27	87.6	23.2
		2.54	76.2	18.3
		3.81	67.6	18.3
BM-P0M6	340	1.27	102.4	23.0
		2.54	92.7	22.5
		3.81	86.1	22.8
BL-P0M6	355	1.69	83.8	15.6
		3.39	99.3	22.3
		5.08	88.9	20.8
BM-P0H3	380	1.27	62.5	14.6
		2.54	63.5	15.2
		3.81	61.5	16.1
BM-P0H6	366	1.27	81.3	18.4
		2.54	87.4	21.2
		3.81	76.2	20.7
BM-P0L3	235	1.27	67.3	17.0
		2.54	76.2	22.6
		3.81	82.0	25.0
BM-M0M0	302	1.27	40.6	10.5
		2.54	43.7	11.9
		3.81	42.2	11.2
BM-F1M3	262	1.27	770	110.2
		2.54	859	89.9
		3.81	970	98.4
BM-F2M3	342	1.27	1102	49.3
		2.54	1212	54.8
		3.81	1189	48.5

Table 3.6. Fracture Toughness Parameters.

Series	Notch Depth a, cm	J_c		S, kg/m	K_c, $\times 10^{-3}$ kg·m$^{-3/2}$	G_c, kg/m	$\frac{J_{cb}}{J_{cr}}$
		J_{cb}, kg/m	J_{cr}, kg/m				
BS-P0M3	1.27	3.52	1.86	8.86	62.2	1.20	1.89
	2.54	3.04	2.21	8.22	62.8	1.21	1.37
	3.81	2.55	2.09	6.55	58.9	1.07	1.22
BM-P0M3	1.27	2.43	1.80	9.27	60.7	1.14	1.35
	2.54	2.52	2.05	9.93	69.7	1.50	1.23
	3.81	2.57	2.00	8.20	61.4	1.18	1.29
BL-P0M3	1.69	3.70	1.50	9.11	70.0	1.52	2.46
	3.39	3.34	2.14	9.43	71.2	1.43	1.56
	5.08	3.38	2.38	7.64	64.9	1.30	1.42
BS-P0M6	1.27	3.30	1.73	9.86	67.5	1.25	1.91
	2.54	3.43	2.63	10.5	70.1	1.36	1.31
	3.81	2.52	2.14	9.47	64.8	1.16	1.18
BM-P0M6	1.27	3.95	2.38	14.4	68.4	1.29	1.66
	2.54	3.36	2.50	11.0	69.3	1.32	1.34
	3.81	2.88	2.09	8.82	57.6	0.91	1.38
BL-P0M6	1.69	3.41	2.46	11.9	76.2	1.61	1.38
	3.39	2.93	2.29	11.9	77.2	1.64	1.28
	5.08	3.16	2.25	9.50	64.0	1.13	1.40
BM-P0H3	1.27	4.59	2.45	9.14	69.9	1.25	1.88
	2.54	3.46	2.61	9.34	71.5	1.30	1.33
	3.81	2.09	2.34	6.98	65.3	1.09	0.89
BM-P0H6	1.27	4.73	2.46	12.9	79.9	1.68	1.92
	2.54	3.82	2.64	11.3	75.9	1.52	1.45
	3.81	2.80	2.64	9.89	68.6	1.25	1.06
BM-P0L3	1.27	2.16	1.07	10.0	48.6	0.96	2.02
	2.54	1.63	1.29	9.18	48.2	0.96	1.26
	3.81	1.52	1.30	7.00	44.0	0.80	1.16
BM-M0M0	1.27	2.80	1.34	6.38	56.0	1.00	2.09
	2.54	2.34	1.70	6.84	58.9	1.11	1.38
	3.81	2.36	1.80	5.63	52.6	0.89	1.31
BM-F1M3	1.27	9.34	6.07	219.	68.5	1.73	1.54
	2.54	10.6	9.02	272.	69.9	1.80	1.17
	3.81	8.13	8.91	223.	67.8	1.70	0.91
BM-F2M3	1.27	50.5	38.7	371.	107.	3.23	1.31
	2.54	43.6	34.0	310.	98.2	2.73	1.28
	3.81	41.4	28.8	209.	78.4	1.75	1.44

Table 3.7. Averaged Fracture Toughness Parameters.

Series	J_c		S, kg/m	K_c, $\times 10^3$ kg·m$^{-3/2}$	G_c, kg/m	$\frac{J_{cb}}{J_{cr}}$	$\frac{S}{J_{cr}}$	$\frac{G_c}{J_{cr}}$
	J_{cb}, kg/m	J_{cr}, kg/m						
BS-POM3	3.04	2.05	7.88	61.3	1.16	1.48	3.83	0.57
BM-POM3	2.50	1.95	9.11	64.0	1.27	1.28	4.68	0.65
BL-POM3	3.46	2.00	8.73	68.7	1.46	1.73	4.37	0.73
BS-POM6	3.09	2.16	9.93	67.5	1.25	1.43	4.60	0.58
BM-POM6	3.39	2.32	11.4	65.1	1.18	1.46	4.91	0.51
BL-POM6	3.16	2.34	11.1	72.5	1.46	1.33	4.75	0.63
BM-POH3	3.38	2.46	8.48	68.9	1.21	1.37	3.44	0.49
BM-POH6	3.79	2.59	11.3	74.7	1.48	1.46	4.38	0.57
BM-POL3	1.77	1.21	8.73	47.0	0.91	1.46	7.19	0.74
BM-MOMO	2.50	1.61	6.29	55.8	1.00	1.55	3.91	0.62
BM-F1M3	9.34	8.00	238.	68.7	1.75	1.17	29.75	0.22
BM-F2M3	45.2	33.8	297.	94.5	2.57	1.34	8.78	0.08

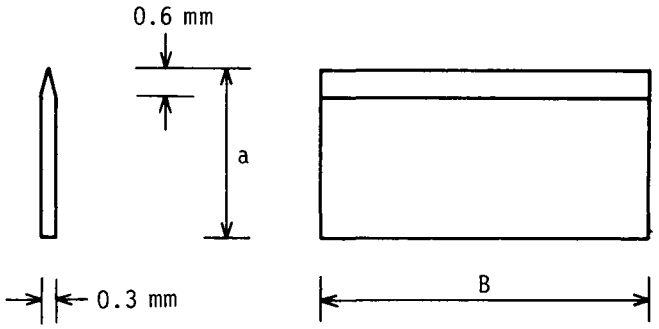

Fig. 3.1. Steel Plate for Cast-in Notch.

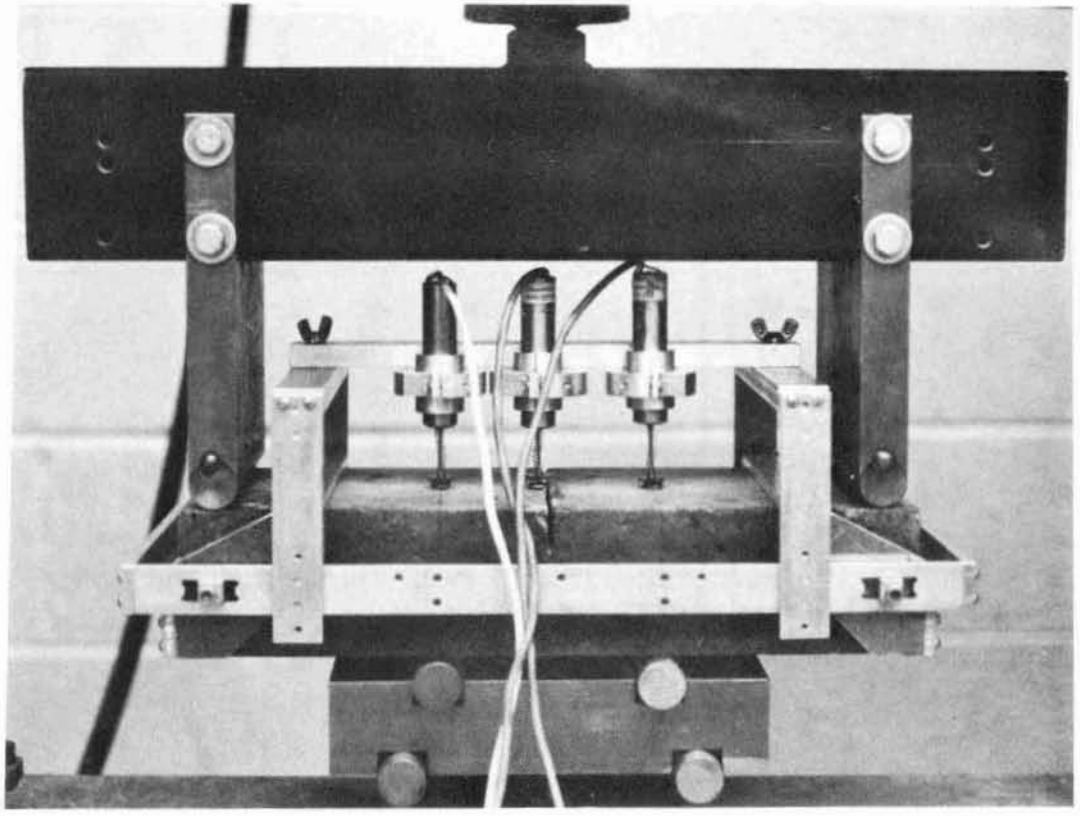

Fig. 3.2. Beam Test Setup.

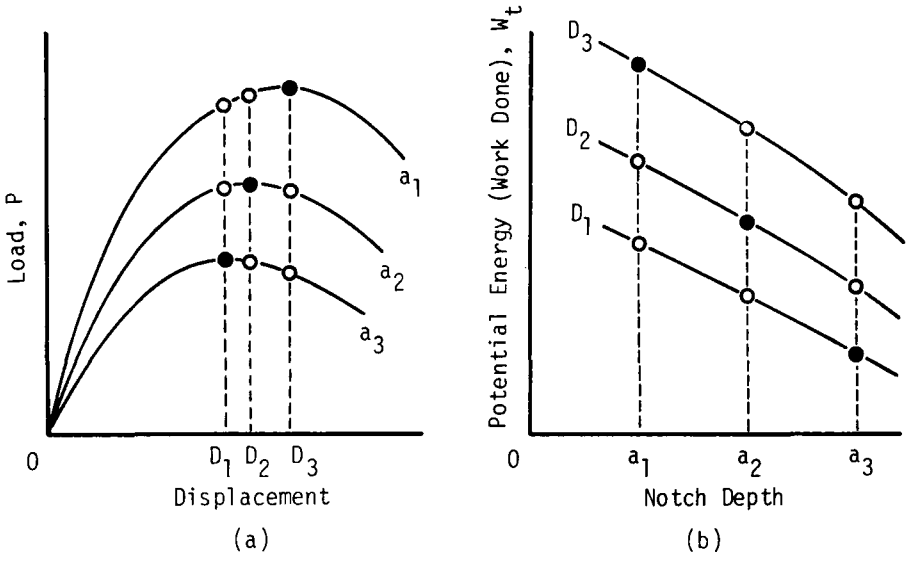

Fig. 3.3. Original B-method to Calculate J_{cb}.

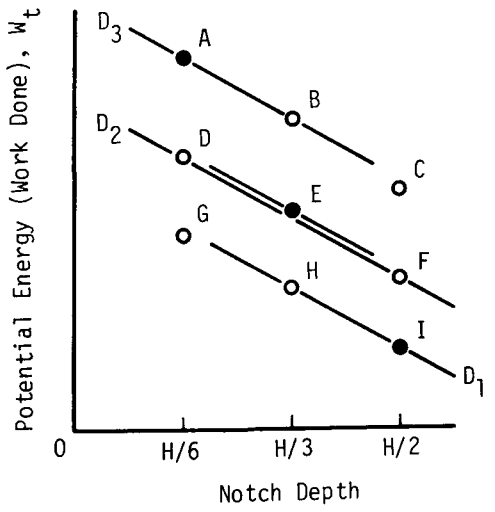

Fig. 3.4. Modified B-method.

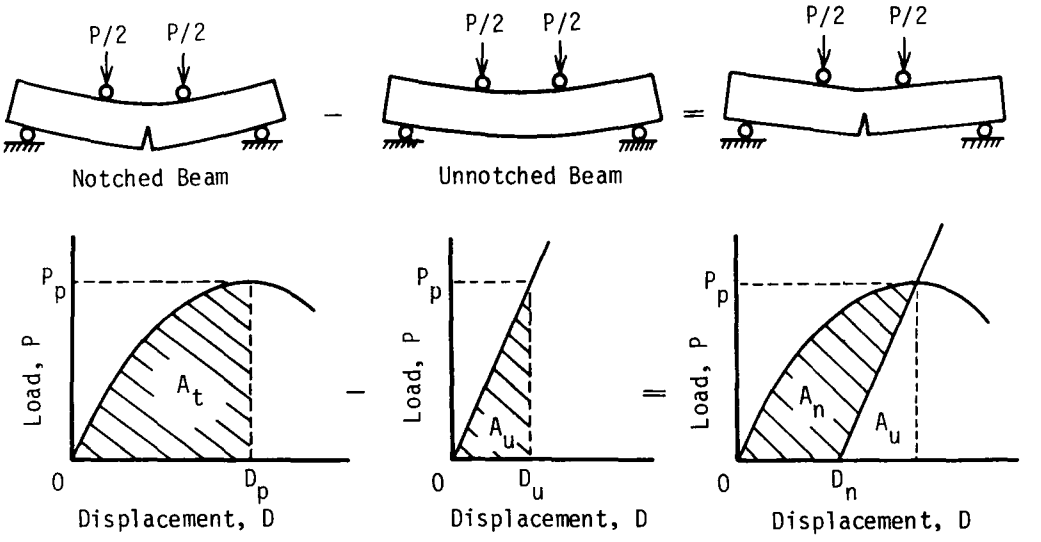

$$J_{cr} = 2\,(A_t - A_u)/\,Bb$$
$$= 2\,A_n\,/\,Bb$$

Fig. 3.5. R-method to Calculate J_{cr}.

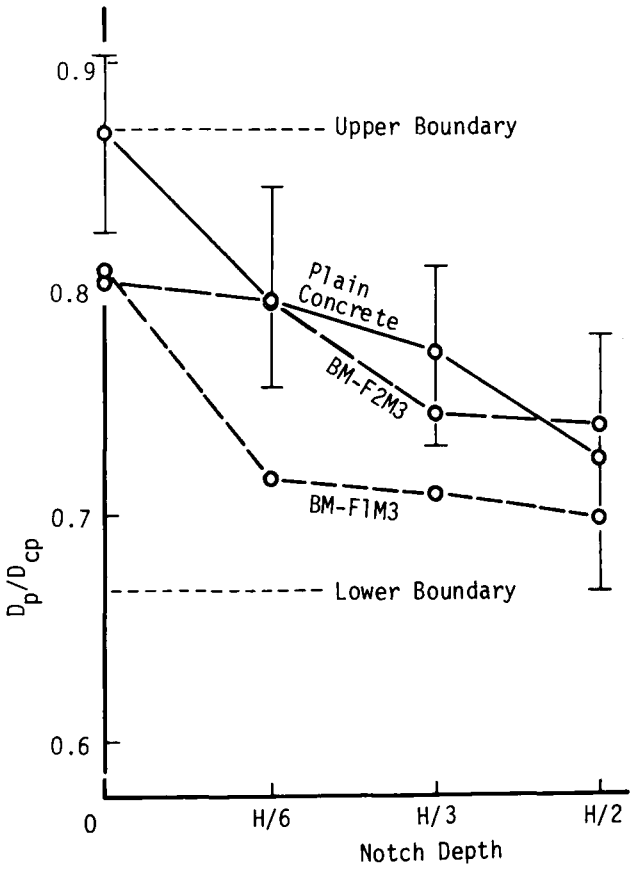

Fig. 3.6. Ratio D_p/D_{cp} and Notch Depth.

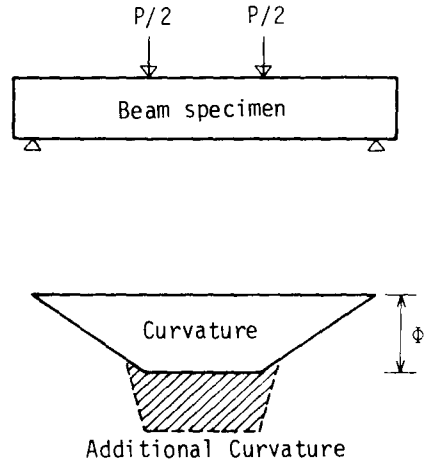

Fig. 3.7. Additional Curvature.

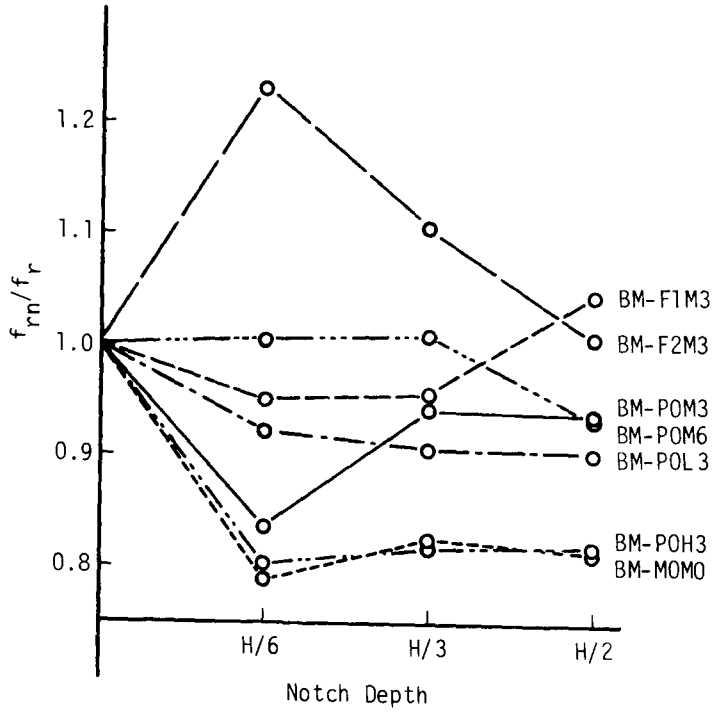

Fig. 3.8. Ratio f_{rn}/f_r and Notch Depth.

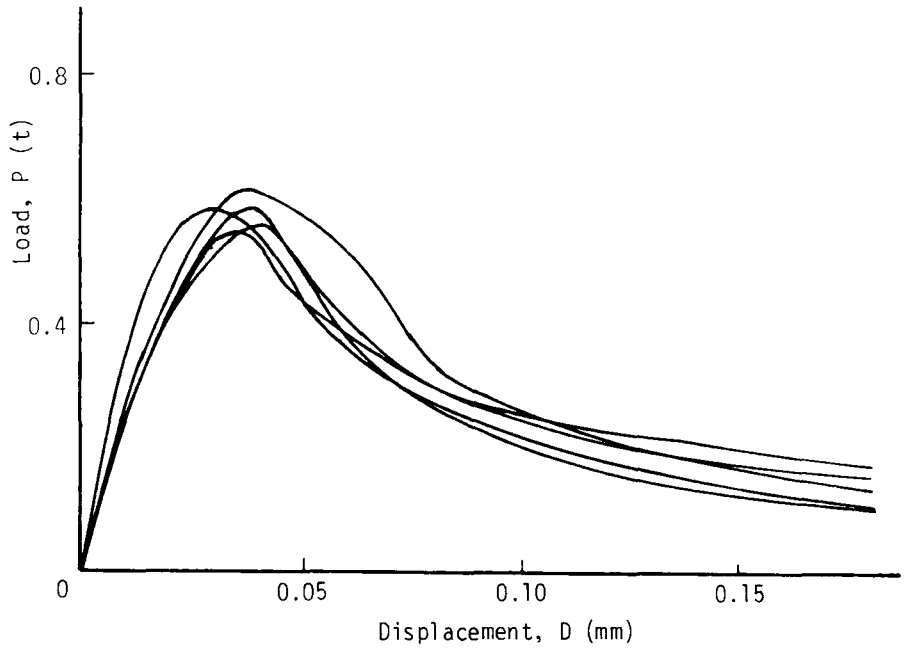

Fig. 3.9. Individual Load-Displacement Diagrams of BM-P0M3 Series (H/3-Notched Beams).

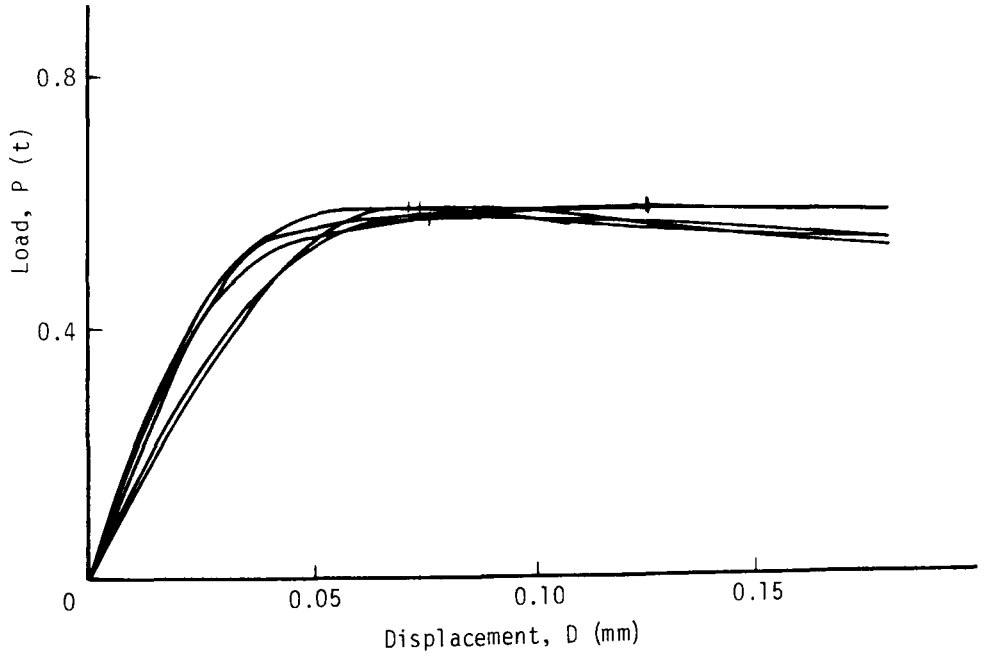

Fig. 3.10. Individual Load-Displacement Diagrams of BM-F1M3 Series (H/3-Notched Beams).

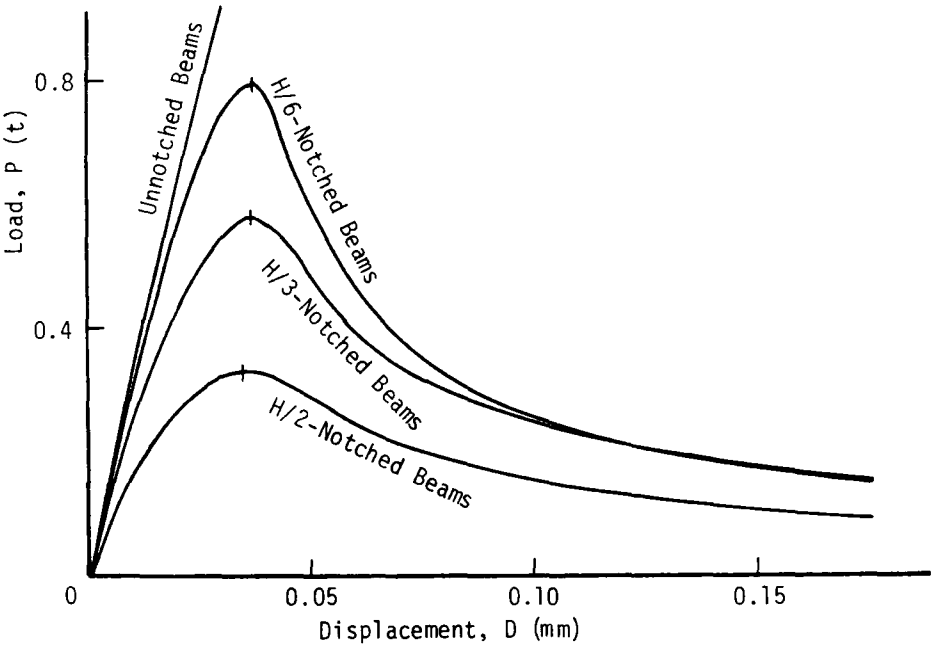

Fig. 3.11. Load-Displacement Diagrams of BM-POM3 Series.

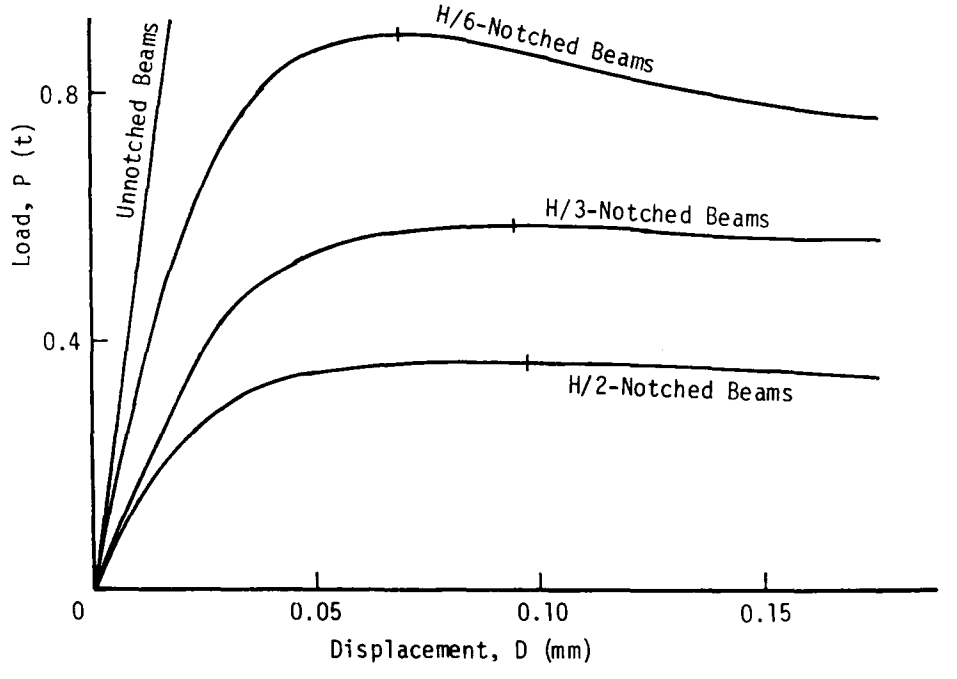

Fig. 3.12. Load-Displacement Diagrams of BM-FlM3 Series.

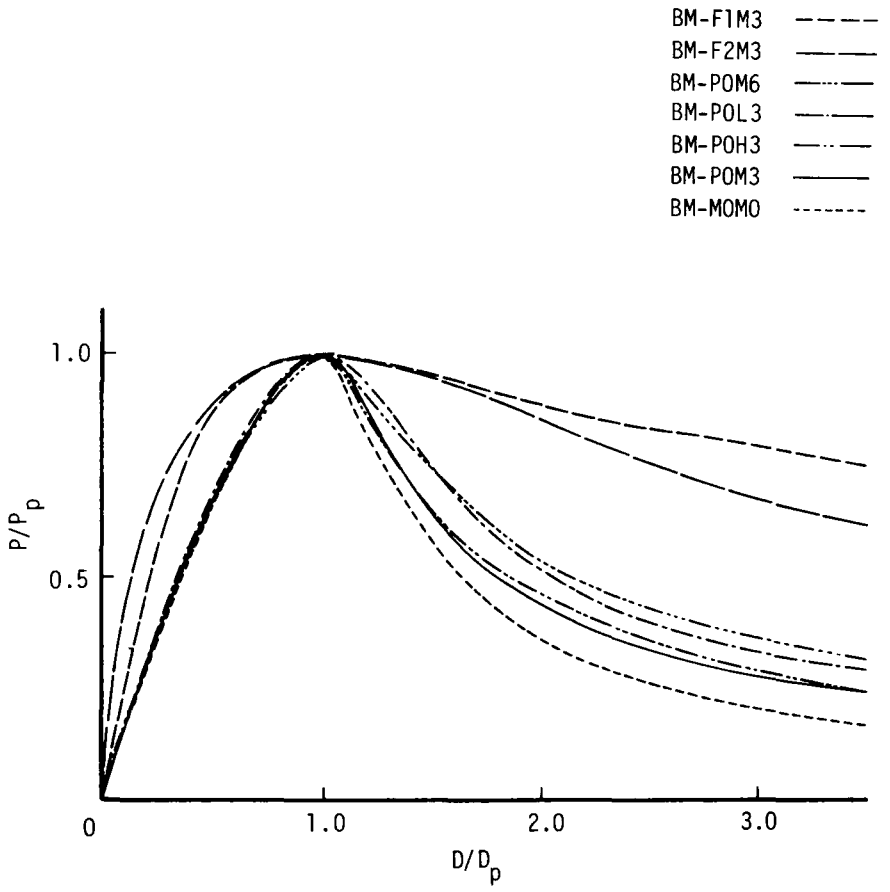

Fig. 3.13. Normalized Load-Displacement Diagrams (H/6-Notched Beams).

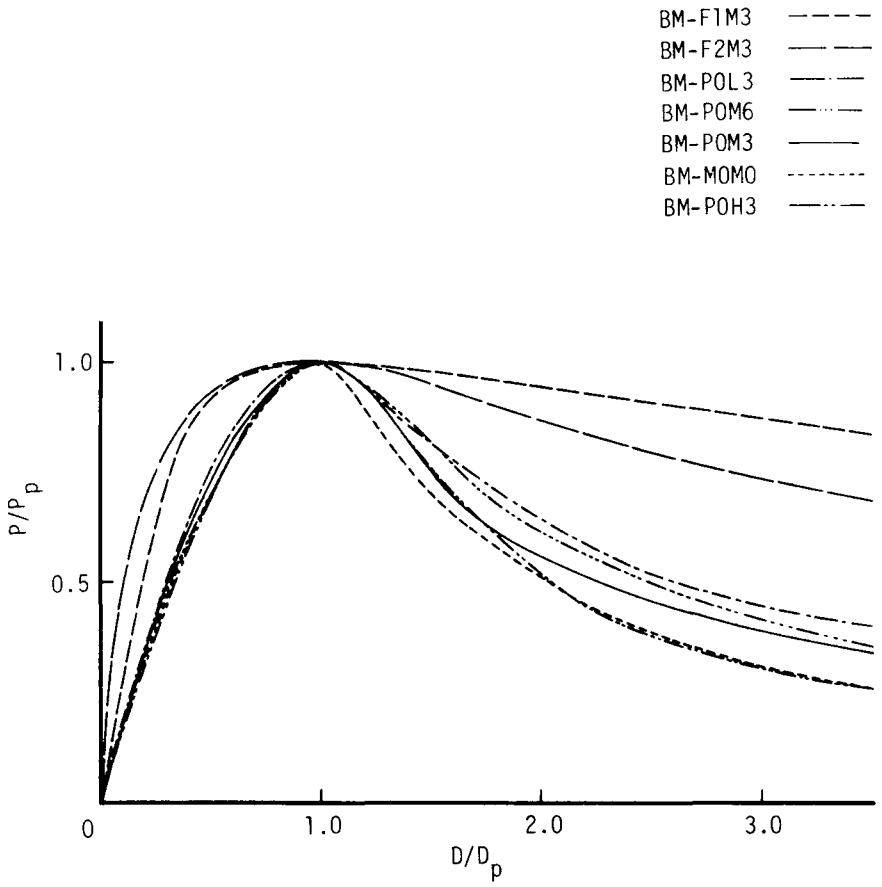

Fig. 3.14. Normalized Load-Displacement Diagrams (H/3-Notched Beams).

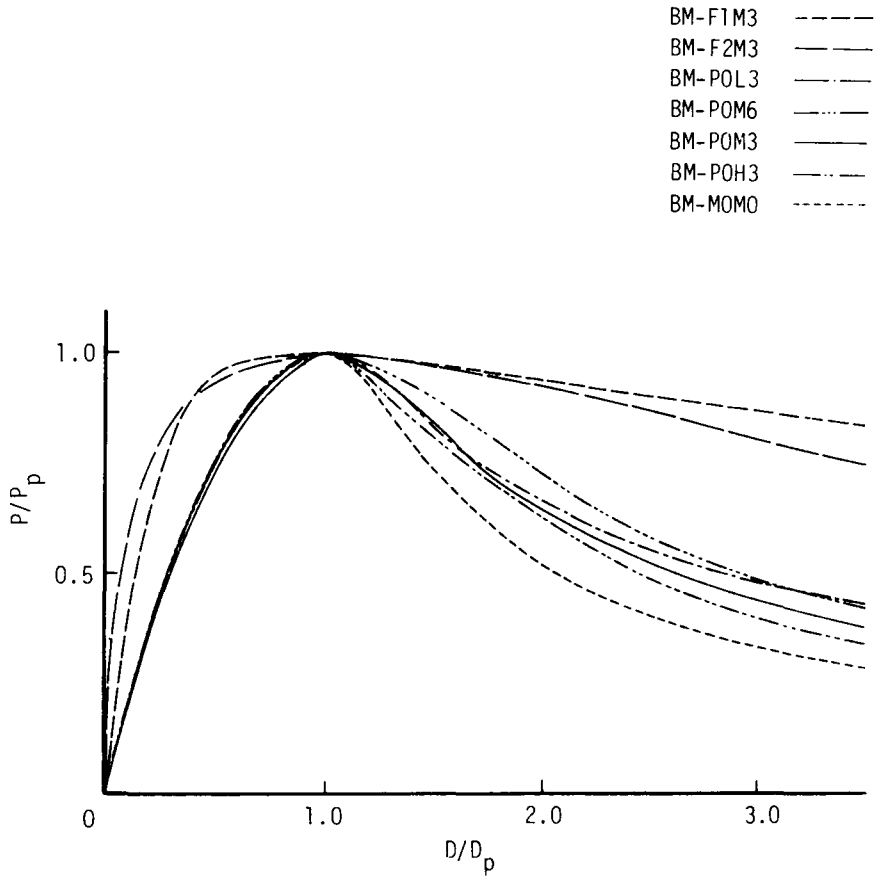

Fig. 3.15. Normalized Load-Displacement Diagrams (H/2-Notched Beams).

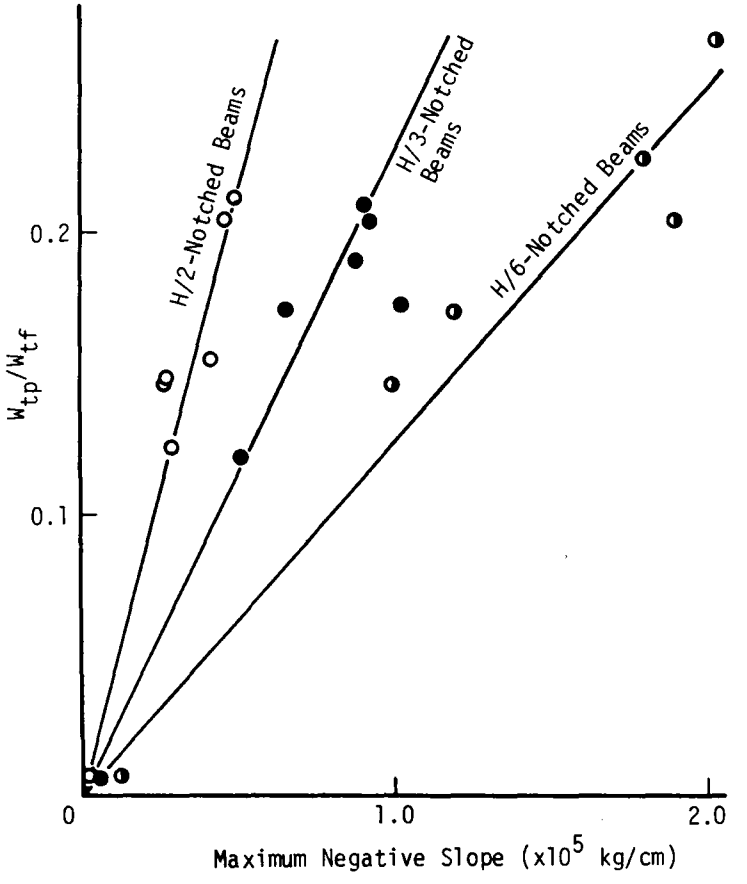

Fig. 3.16. Ratio W_{tp}/W_{tf} and Maximum Negative Slope.

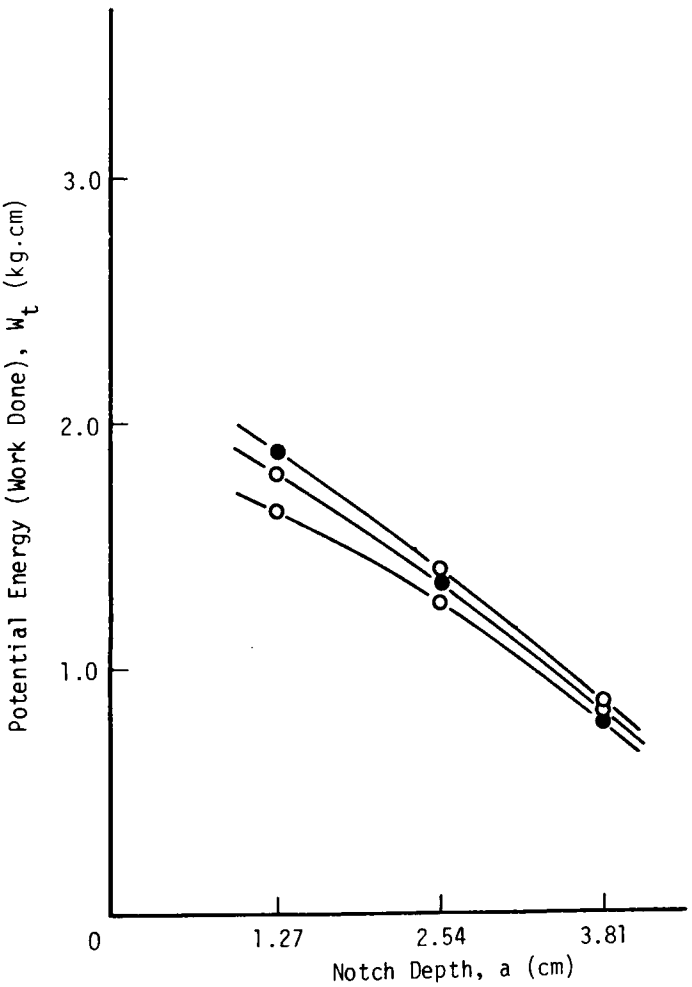

Fig. 3.17. Potential Energy and Notch Depth (BM-POM3 Series).

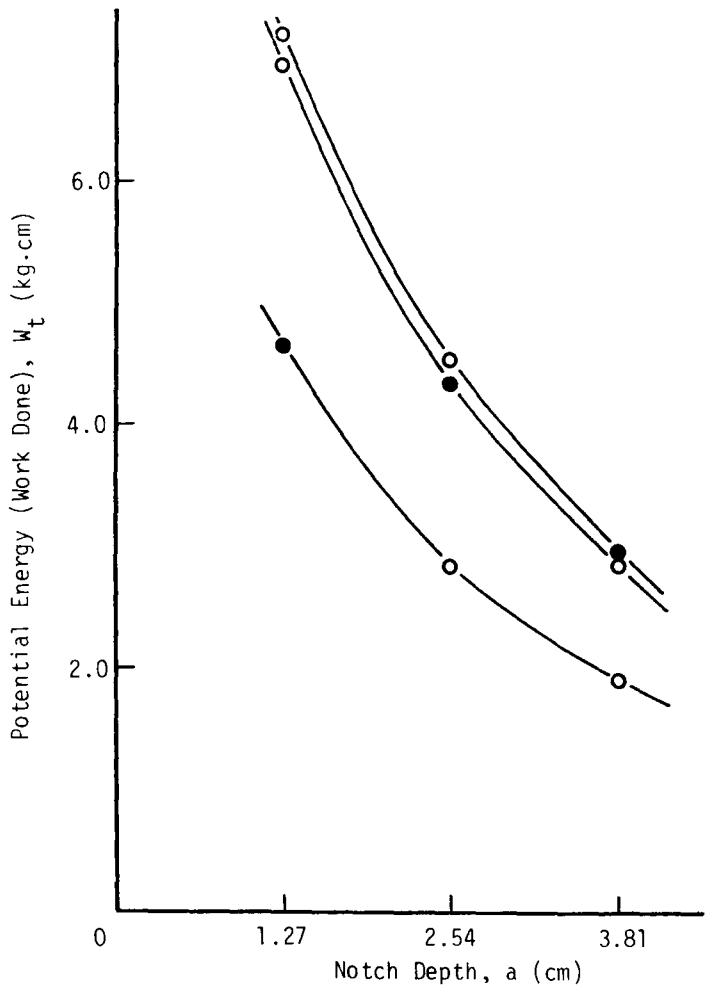

Fig. 3.18. Potential Energy and Notch Depth (BM-F1M3 Series).

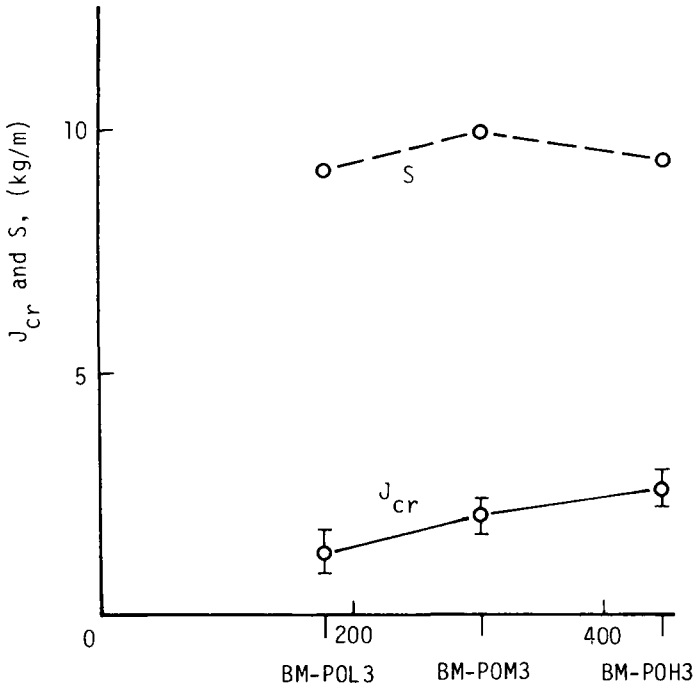

Fig. 3.19. Compressive Strength and Fracture Toughness Parameters.

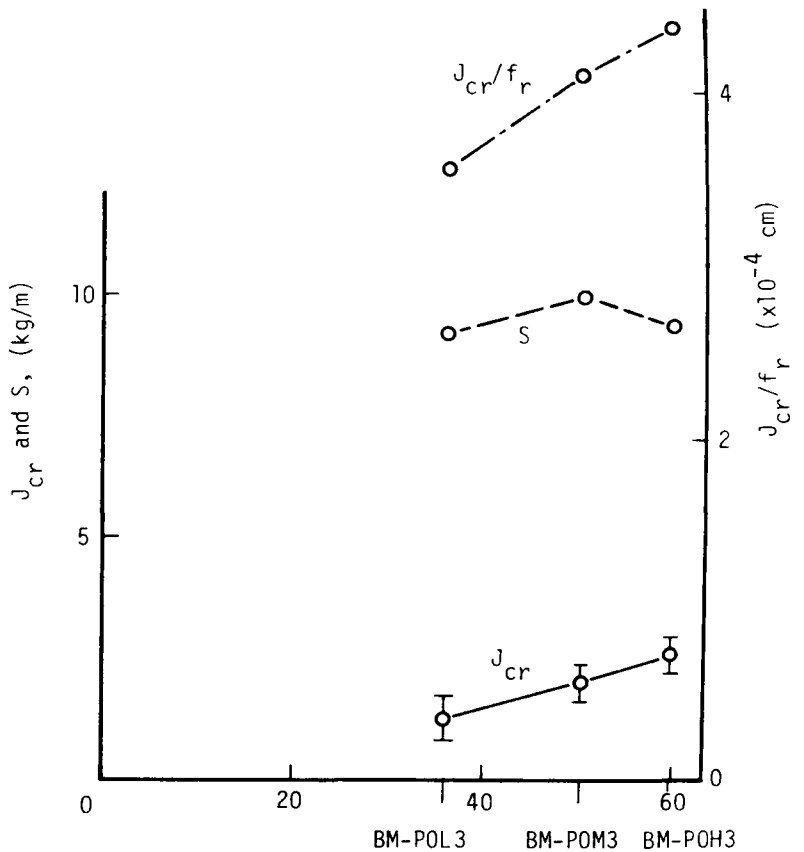

Fig. 3.20. Modulus of Rupture and Fracture Toughness Parameters.

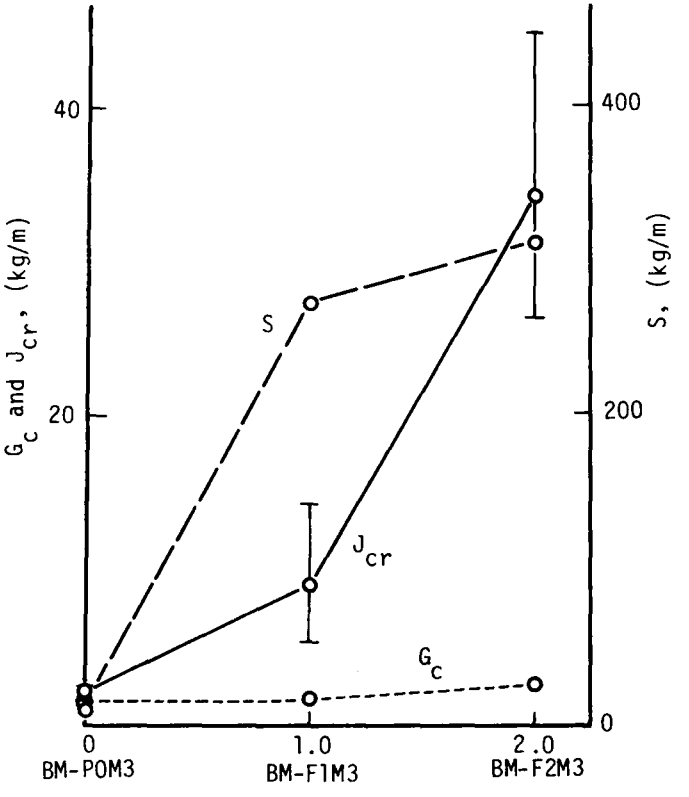

Fig. 3.21. Steel Fiber Content and Fracture Toughness Parameters.

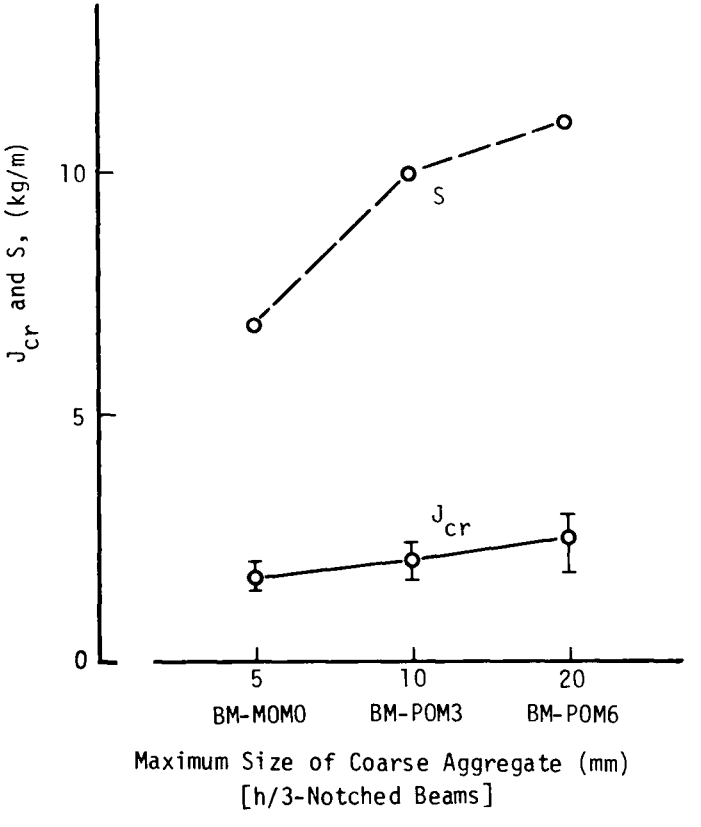

Fig. 3.22. Maximum Aggregate Size and Fracture Toughness Parameters.

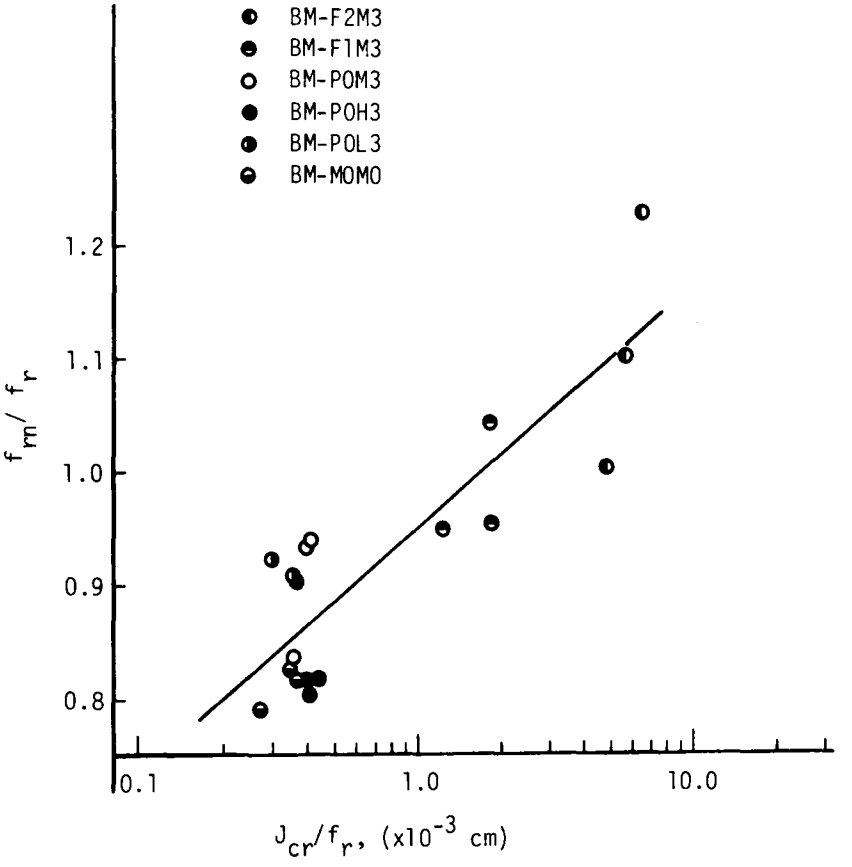

Fig. 3.23. Ratio f_{rn}/f_r and J_{cr}/f_r.

CHAPTER 4. FRACTURE PROCESS OF CONCRETE IN COMPRESSION

4.1 INTRODUCTION

The fracture process of concrete in compression was investigated in terms of the energy transformation concept.

The work done, W_t, and its transformations, W_r and W_i, were calculated. The two components of the dissipated energy, W_{icr} and W_{ifr}, were separated. W_{icr} and W_{ifr} are the energies which are consumed by crack formation and by viscous friction, respectively.

The effects of concrete quality, loading rate, moisture content, and specimen size, on the mechanical properties of concrete were examined from the view point of the energy approach.

The resistance ability to strength failure and the energy absorbing capacity of concrete in compression are also discussed. Generally, the falling branch of the load-displacement diagram in compression does not terminate. For this reason, the total dissipated energy was calculated by simplifying the diagram, as shown in Fig. 4.1 The points U and T correspond to two-thirds and one-third of the peak load, respectively. The total dissipated energy is represented by the marked area.

4.2 EXPERIMENTAL PROCEDURES

4.2.1 Test Program

The following five series of test were conducted:

(I) Energy-Displacement Relationship

(II) Effect of Concrete Qualities

(III) Effect of Loading Rate

(IV) Effect of Moisture Content

(V) Effect of Specimen Size

In Series (I), the method used to obtain the energy-displacement relationship is discussed and the properties of the relationship are described. In the succeeding series, those effects on the mechanical properties of concrete are investigated in terms of the energy transformation concept. The two components of the dissipated energy, W_{icr} and W_{ifr}, are calculated in Series (IV). Series (V) describes the fracture parameters for evaluating the fracture behavior of concrete in compression.

4.2.2 Materials and Mix Proportions

Nine kinds of concrete mixes were used and labeled [A] through [I]. The mix proportions of concrete and their relationship with the test series are tabulated in Table 4.1. The measured slump of each concrete is also given in Table 4.1. Ordinary Portland cement was used in all concrete mixes.

Concrete [A], which was used in Series (I), (III) and (IV), was made from Toyoura standard sand (specific gravity: 2.63, size of about 0.1 $\sim$ 0.3 mm) and crushed coarse aggregate (specific gravity: 2.64, maximum size: 15 mm).

In Series (II), two kinds of normal concrete [B] and [C], high-strength concrete [D], and lightweight concrete [E] were used. River sand (specific gravity: 2.60, fineness modulus: 3.01) and crushed coarse aggregate (maximum size: 20 mm) were used in the normal concretes and the high-strength concrete. A water-reducer (NL-1400) was added to the high-strength concrete. The lightweight concrete was made from lightweight coarse aggregate (specific gravity: 1.14, water absorption: 2.6%, and maximum size: 15 mm) and lightweight sand (specific gravity: 1.95, water absorption: 3.7%, and

fineness modulus: 2.95).

The normal concretes [F] and [G] in Series (V) were made from Toyoura sand and crushed coarse aggregate (maximum size: 15 mm). Toyoura sand and lightweight coarse aggregate were used in the lightweight concretes [H] and [I] in Series (V). In order to reduce the bond strength between the coarse aggregate and the mortar matrix, the aggregates of the concretes [G] and [I] were coated with a waterproof agent.

4.2.3 Fabrication of Specimens

Cylindrical specimens (ϕ10x20 cm) were used in Series (I) through (IV). Three sizes of prismatic specimens (height x length x width: 10x10x10 cm, 30x10x10 cm, and 50x10x10 cm) were subjected to the compression tests in Series (V). The curing duration, testing age, and compressive strength of the concrete are presented in Table 4.2. Specimens of all series were cured in 20°C water for more than three weeks after casting. Only the specimens of Series (IV) were stored in three different storage conditions for a period of 19 days after curing in order to change the moisture content in the concrete.

4.2.4 Loading and Displacement Measuring

As illustrated in Fig. 4.2, five types of loading were performed. The sustained loading and the repeated loading are shown in Fig. 4.2 (a) and (b), respectively. The loading condition in Fig. 4.2 (c) is obtained using a single process of loading and unloading. Point "P" in the figure is the unloading point. This diagram in Fig. 4.2 (c) is called the "single loading diagram" hereafter. Fig. 4.2 (d) shows the so-called GIR-diagram (gradually increased repeated load-displacement diagram), in which the process of loading and unloading is repeated with an increase in the maximum displace-

ment at unloading points. The dotted line indicates the envelope curve. Fig. 4.2 (e) shows the so-called CI-diagram (constantly increased load-displacement diagram), which is obtained under a constant displacement rate.

A stiff testing machine with a servo-controller was used in these experiments, as well as in the experiments in Chapter 2. The load-point displacement in this chapter is concerned with compressive deformation, which was measured by differential transformers attached to the specimens. The load-displacement diagrams were displayed on an X-Y recorder.

Complete load-displacement diagrams including the region after strength failure were obtained under a constant loading rate. The standard displacement rate for cylindrical specimens of 20 cm in height was 6.8×10^{-3} mm/sec., which was 34×10^{-6}/sec. in terms of the strain rate. In the case of repeated loading, loading was controlled in terms of the loading rate instead of the displacement rate. The standard rate was 0.4t/sec.

4.3 ENERGY-DISPLACEMENT RELATIONSHIP

As previously described in Section 2.4, the work done, W_t, and its transformed components, W_r and W_i, were calculated by measuring the areas on the load-displacement diagrams with a planimeter. The fracture process of concrete can be expressed in terms of the energy transformation concept by measuring these energies at each stage.

The following two methods for obtaining the energy -displacement relationship were compared:

(1) A-method

The energies were calculated from the single loading diagrams. The unloading points are shown in Fig.

4.3 (a). Four specimens were assigned for each unloading point. Thus, twenty eight specimens were tested by this method.

(2) B-method

The energies were calculated from the GIR-diagrams with seven loading repetitions as shown in Fig. 4.3 (b). Four specimens were used in this method.

Fig. 4.4 shows the relationship between the energies and the displacement using the A-method. Fig. 4.5 shows the same relationship using the B-method. In these figures, the energies W_t and W_r were normalized by W_{tp}, and the displacement D was normalized by D_p. W_{tp} and D_p are the values of W_t and D at the peak load point.

The energy-displacement relationships in Figs. 4.4 and 4.5 are almost identical to each other. Consequently, the energy-displacement relationship can be calculated from a lesser number of specimens by B-method than by A-method.

As seen from Figs. 4.4 and 4.5, the elastic strain energy, W_r, became maximum at the strength failure point (peak load point).

4.4 EFFECT OF CONCRETE QUALITIES

Fig. 4.6 shows the energy-displacement relationship by the B-method (described in Section 4.3) for four kinds of concrete; namely, normal concretes [B] and [C], high-strength concrete [D], and lightweight concrete [E].

The ratio W_r/W_{tp} at the peak load point for the high-strength concrete and the lightweight concrete was larger than that for the normal concretes. The energy ratio W_{rp}/W_{tp} may be affected by the difference in the mechanical properties of the coarse aggregate and the mortar matrix, for example,

the strength and the modulus of elasticity. Therefore, the energy ratio can be used as an index of the homogeniety of the concrete.

In the post-failure region, the ratio W_t/W_{tp} for the lightweight concrete and the high-strength concrete was smaller than that for the normal concrete. The ratio W_t/W_{tp} may be used as an index for the brittleness of concrete.

4.5 EFFECT OF LOADING RATE

The magnitude of the various energy components at peak load is considered to express the tendency toward energy change during the fracture process of concrete. Here, W_{tp}, W_{rp}, and W_{ip} are used to represent the energies W_t, W_r, and W_i respectively, at peak load.

The compressive strength of concrete, the energies W_{tp}, W_{rp}, W_{ip}, and the ratios, W_{rp}/W_{tp}, W_{ip}/W_{tp}, W_{rp}/W_{ip}, under the three kinds of loading rates are shown in Table 4.3. These values are all averages from four specimens. As the loading rate increased, the energy W_{ip} decreased while the energy W_{rp} and the ratios W_{rp}/W_{tp} and W_{rp}/W_{ip} increased. This result suggests that the increase in compressive strength under high loading rate is caused by a decrease in time -dependent deformation, resulting in greater elasticity in the concrete.

4.6 EFFECT OF MOISTURE CONTENT

The storage conditions for Series (IV), and the amount of the evaporated water per specimen are given in Table 4.4. Hereafter, the three groups are designated A-174, A-119, and A-0. The first letter in the name indicates the concrete mix. The succeeding numerals identify the amount of evaporated

water.

The energies and energy ratios at peak load for each group are shown in Table 4.5, with the compressive strength. With a decrease in the moisture content, the energy ratio W_{rc} was increased. This result means that the increase in compressive strength due to decreased moisture content was caused by greater elasticity in the concrete. The internal bond energy and the frictional resistance may increase due to drying.

Both repeated loading and sustained loading were employed in Series (IV). The maximum load P_{max} adopted in the loading corresponds to the predetermined displacement D_{m1} in the virgin load-displacement diagram. The respective loadings were continued until the total displacement reached another predetermined larger displacement D_{m2} (= D_{m1}+0.04 mm). As seen from Table 4.6, the number of loading repetitions and the duration of the sustained loading from D_{m1} to D_{m2} increased as the moisture content decreased. The rate of increase in the duration was larger than that in the number of repetitions. The relationship between the fatigue fracture process and the creep fracture process in the concrete was much affected by moisture content.

For each group, the relationship between the dissipated energy, W_i, for one specimen (volume: 1570 cm^3) and the number of loading repetitions is given in Table 4.7. Fig. 4.7 also shows an example of this relationship. In the figure, W_{i1} represents W_i at the first repetition. The dissipated energy reached maximum at the first repetition and then decreased rapidly and became almost constant.

By means of acoustic emission and direct observation of the internal cracking, it has been confirmed that most of the

internal cracking occurs during the first repetition [26,30].

Therefore, it is likely that the constant dissipated energy in Fig. 4.7 and Table 4.7 corresponds to the energy W_{ifr}, which is absorbed mainly by viscous friction in the internal structure of the concrete. Assuming that W_{ifr} is equal to W_i at the 8th repetition in Table 4.7, W_{icr} and W_{ifr} during the first repetition are calculated and shown in Table 4.8. The energy W_{icr}, which is absorbed by crack formation, and the ratio W_{ifr}/W_{icr} became smaller as the moisture content of the concrete decreased. This fact reveals that with a decrease in the moisture content in the concrete, the deformation due to the moisture moving under pressure decreases and the surface energy increases.

4.7 EFFECT OF SPECIMEN SIZE

Four concrete mixes and three specimen sizes were adopted in Series (V). Therefore, the specimens in Series (V) were divided into twelve groups. The first letter of the group name indicates the concrete mix, and the second pair of numerals indicates the specimen height, as in the following examples: F-10, G-30, etc. As described in Section 4.2.2, [F] and [G] were normal concretes, and [H] and [I] were lightweight concretes. The aggregates in [G] and [I] were coated with a waterproof agent.

Figs. 4.8 and 4.9 show the load-displacement diagrams of the twelve groups. The load-displacement diagram for each group was determined from the envelope curves of the four specimens.

The peak loads and the compressive displacements at the peak load points are given in Figs. 4.10 and 4.11, respectively. The peak loads for the 10 cm height specimens were about

20% greater than those for the other size specimens. There was no difference in the peak load between the 30 cm height specimens and the 50 cm height specimens. The displacement at the peak load points constantly increased with an increase in the specimen height. Thus, the nominal compressive strains at the peak load points were almost constant for all groups. This fact indicates that the internal fracture of the concrete was uniformly distributed within the specimens, at least until the strength failure point.

The maximum negative slopes on the load-displacement diagrams in Figs. 4.8 and 4.9 are shown in Fig. 4.12. The total dissipated energy at complete failure and the work done at strength failure for each group are presented in Fig. 4.13 and 4.14, respectively.

The maximum negative slope and the work done, W_{tp}, increased with an increase in the specimen height. When the specimen height is greater, a greater portion of the total dissipated energy is applied to the specimen before strength failure occurs. Consequently, the amount of additional work done on the specimen after strength failure is smaller, and thus, the maximum negative slope on the load-displacement diagram is steeper.

The total dissipated energy for the 30 cm height specimens and the 50 cm height specimens was almost the same, but was about half of that for the 10 cm height specimens. Because the internal fracture of the concrete after strength failure was concentrated in a local region, such as a shear failure band, the total dissipated energy was not affected by the specimen height. Therefore, the energy dissipating capacity of the concrete in compression can be represented by the dissipated energy per unit cross sectional area.

W_{ip} and W_{rp}, the dissipated energy and the elastic strain energy at the peak load, are also presented in Fig. 4.14. For the normal concretes, the dissipated energy W_{ip} was larger than the elastic strain energy W_{rp}. But, for the lightweight concretes, W_{ip} was smaller than W_{rp}. The higher the ratio W_{rp}/W_{tp}, the greater the maximum negative slope. The resistance ability to the strength failure in compression can be expressed by the critical work done per unit volume at the peak load point, because the compressive deformation before the peak load point was macroscopically uniform over the entire specimen.

The lightweight concretes had a larger maximum negative slope and a smaller total dissipated energy than the normal concretes. The total dissipated energy for the concretes with the coated coarse aggregates was smaller than that for the untreated concretes. The maximum negative slope for the lightweight concrete decreased due to the coating. Especially in the case of the lightweight concrete, the coating treatment much reduced the crack arresting ability of the coarse aggregate during the fracture process.

4.8 CONCLUSION

The results of this study on the fracture process of concrete in compression can be summarized as follows:

(1) In the fracture process of concrete in compression, the reversible strain energy became maximum at the strength failure point.

(2) The energy ratio W_{rp}/W_{tp} for the high-strength concrete and the lightweight concrete was larger than that for the normal concrete. The energy ratio may be used as an index of the homogeneity of the concrete.

(3) As the loading rate increased, the compressive strength and the energy ratio W_{rp}/W_{ip} increased. As the moisture content in the concrete decreased, the compressive strength and the energy ratio W_{rp}/W_{ip} increased. Therefore, the energy transformation concept can explain the increase in compressive strength due to high loading rate and low moisture content.

(4) With a decrease in moisture content, the energy W_{icr} (consumed by crack formation) increased and the energy W_{ifr} (consumed by viscous friction) decreased. The fact reveals that with a decrease in the moisture content of the concrete, deformation due to movement of moisture decreases, and the surface energy in the concrete increases.

(5) Since the compressive deformation before the peak load point is macroscopically uniform over the entire specimen, the ability to resist strength failure in compression can be expressed by the critical work done per unit volume at the peak load point.

(6) The total dissipated energy was not affected by the specimen height, because the internal fracture of the concrete after strength failure was concentrated in a local region, such as a shear failure band. Thus, the energy dissipating capacity of the concrete in compression may be represented by the dissipated energy per unit cross sectional area.

(7) When the specimen height is greater, a greater portion of the total dissipated energy is applied to the specimen before strength failure. Consequently, the amount of additional work done on the specimen after strength failure is smaller, and thus, the maximum negative slope is steeper.

Table 4.1. Mix Proportions.

Mix	Water-Cement Ratio	Sand-Aggr. Ratio	Mix Materials, kg/m^3						Slump cm	Test Series				
						Gravel, mm		Admixture						
			Water	Cement	Sand	5∿15	5∿20	WR		I	II	III	IV	V
A	0.64	0.40	216	343	698	1063	-	-	5	*	-	*	*	-
B	0.54	0.41	192	355	730	-	1092	-	11	-	*	-	-	-
C	0.43	0.39	192	446	666	-	1082	-	8	-	*	-	-	-
D	0.28	0.30	152	550	517	-	1254	5	6	-	*	-	-	-
E	0.50	0.39	180	360	537	607	-	-	6	-	*	-	-	-
F	0.63	0.40	220	350	683	1032	-	-	10	-	-	-	-	*
G	0.63	0.40	220	350	683	1032°	-	-	17	-	-	-	-	*
H	0.57	0.40	200	350	704	542	-	-	7	-	-	-	-	*
I	0.57	0.40	200	350	704	534°	-	-	8	-	-	-	-	*

° Coated with a waterproof agent.

Table 4.2. Test Conditions.

Mix	Curing Duration days	Testing Age days	Compressive strength f_c, kg/cm^2
A	21	about 40	about 350
B	21	28∿34	318
C	21	28∿34	420
D	21	28∿34	693
E	21	28∿34	294
F	27	38∿52	456
G	27	38∿52	439
H	27	38∿52	465
I	27	38∿52	445

Table 4.3. Effect of Loading Rate on Energy Components.

Displacement Rate x10^{-3} mm/sec.	Compressive Strength f_c, kg/cm^2	Energy, kg·cm			$\frac{W_{rp}}{W_{tp}}$	$\frac{W_{ip}}{W_{tp}}$	$\frac{W_{rp}}{W_{ip}}$
		W_{rp}	W_{ip}	W_{tp}			
34.	371	460	708	1168	0.39	0.61	0.65
6.8	341	449	775	1224	0.37	0.63	0.58
1.36	336	412	743	1155	0.36	0.64	0.56

Table 4.4. Storage Conditions and Evaporated Water.

Group	Relative Humidity %	Temperature °C	Storage Duration days	Evaporated Water g
A-174	25	70	19	174
A-119	80	70	19	119
A-0	in water	70	19	0

Table 4.5. Effect of Moisture Content.

Group	Compressive Strength f_c, kg/cm^2	Energy, kg·cm			$\frac{W_{rp}}{W_{tp}}$	$\frac{W_{ip}}{W_{tp}}$	$\frac{W_{rp}}{W_{ip}}$
		W_{rp}	W_{ip}	W_{tp}			
A-174	352	309	327	636	0.49	0.51	0.95
A-119	352	307	380	687	0.45	0.55	0.81
A-0	338	289	368	657	0.44	0.56	0.79

Table 4.6. Repeated Loading and Sustained Loading

Group	Predetermined Displacement D_{ml}, mm	Maximum Load P_{max}, t	$\frac{P_{max}}{P_p}$	Number of Loading Repetitions	Duration of Sustained Loading min.
A-174	0.245	22.7	0.82	12.6	23.5
A-119	0.235	22.8	0.83	8.2	6.2
A-0	0.237	22.1	0.83	4.3	1.4

Table 4.7. Dissipated Energy for Each Repetition.

Group	Dissipated Energy, W_i, kg·cm				
	1st	2nd	4th	8th	16th
A-174	122	43	35	34	31
A-119	121	43	35	33	33
A-0	128	58	50	50	-

Table 4.8. Components of Dissipated Energy at First Loading.

Group	Components of Dissipated Energy		Dissipated Energy W_i, kg·cm	$\frac{W_{ifr}}{W_{icr}}$
	W_{icr}, kg·cm	W_{ifr}, kg·cm		
A-174	88	34	122	0.38
A-119	88	33	121	0.37
A-0	78	50	128	0.63

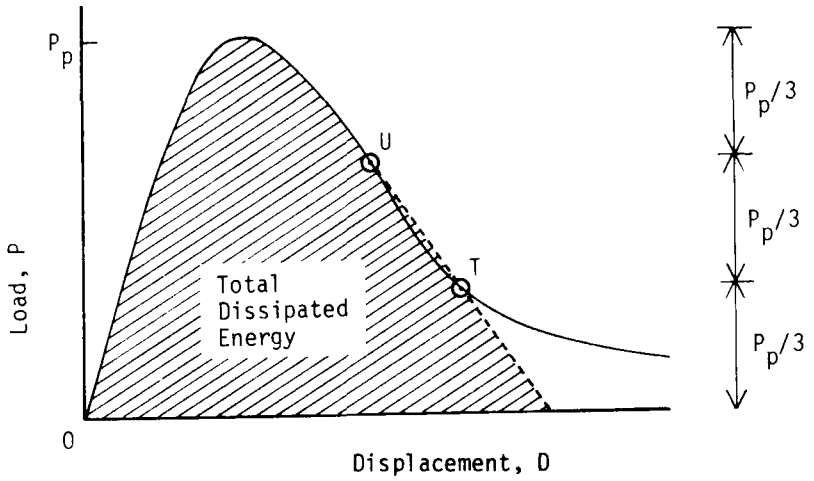

Fig. 4.1. Calculation of Total Dissipated Energy.

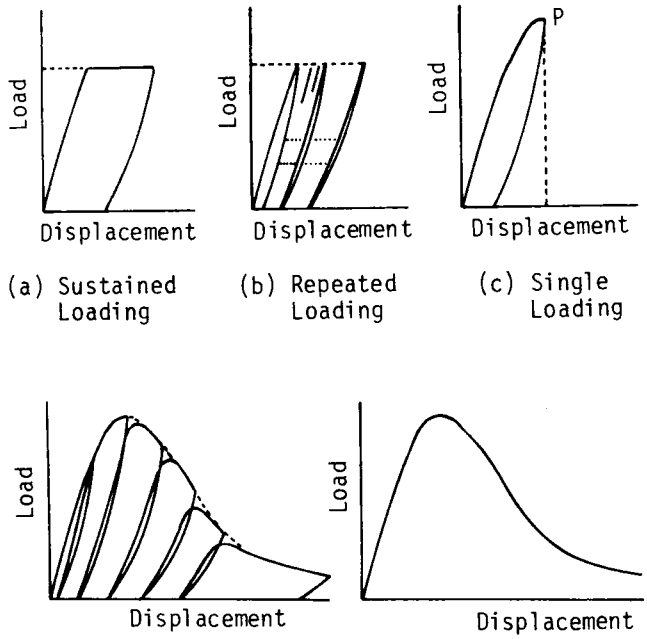

Fig. 4.2. Loading Types.

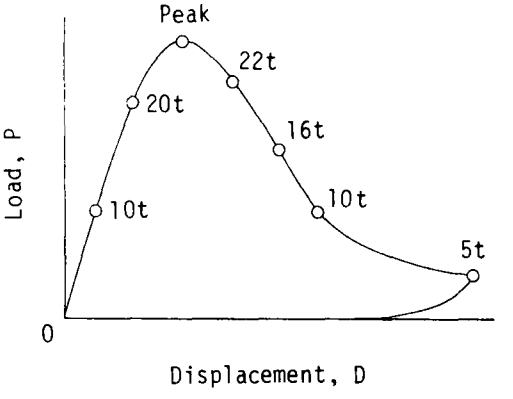

(a)

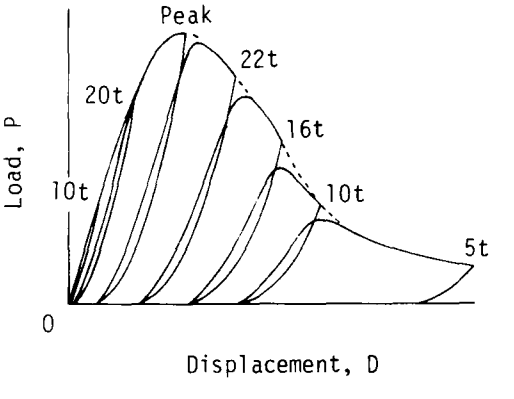

(b)

Fig. 4.3. Load at Unloading Points.

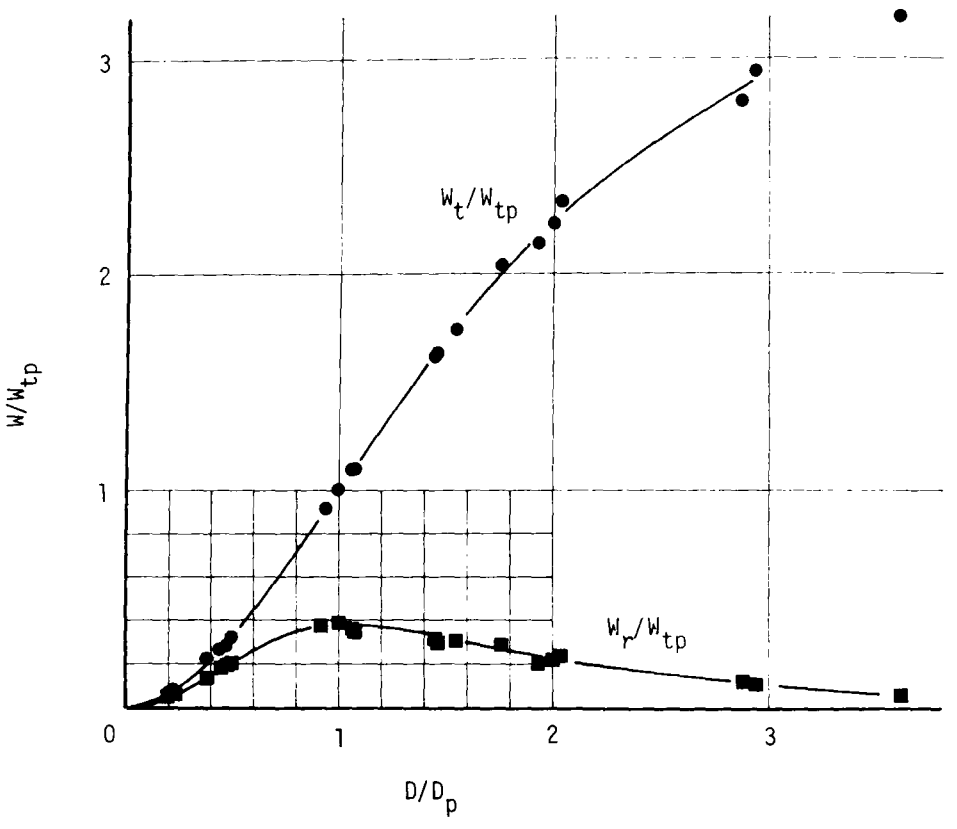

Fig. 4.4. Energy-Displacement Relationship by A-method.

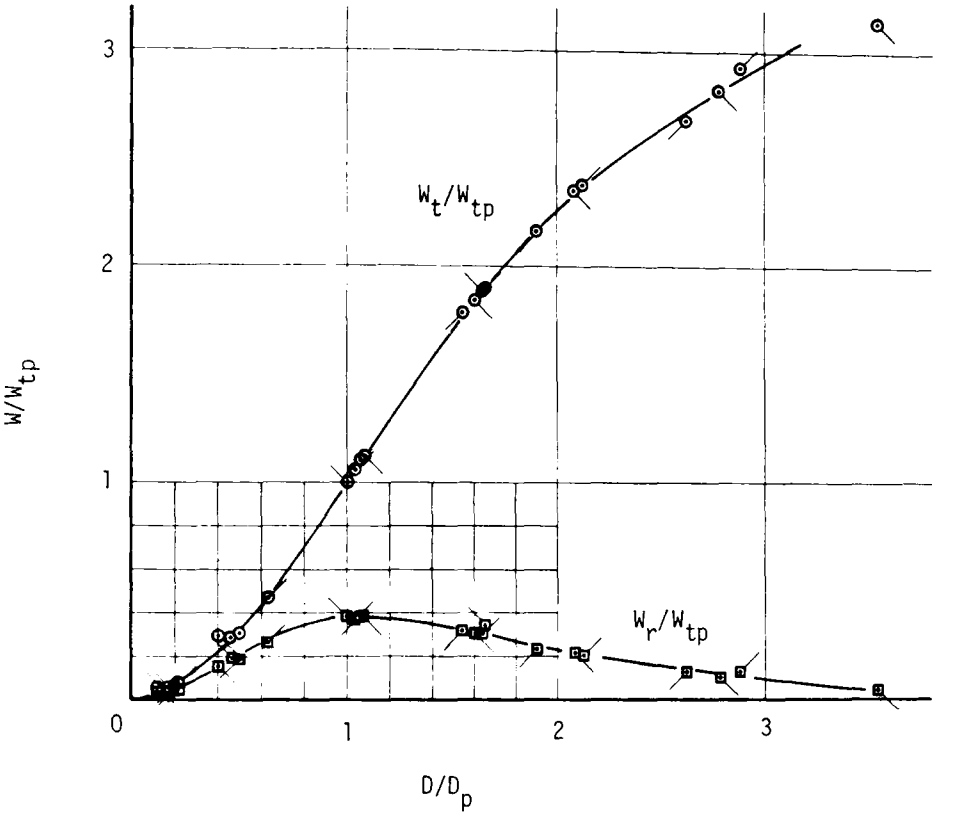

Fig. 4.5. Energy-Displacement Relationship by B-method.

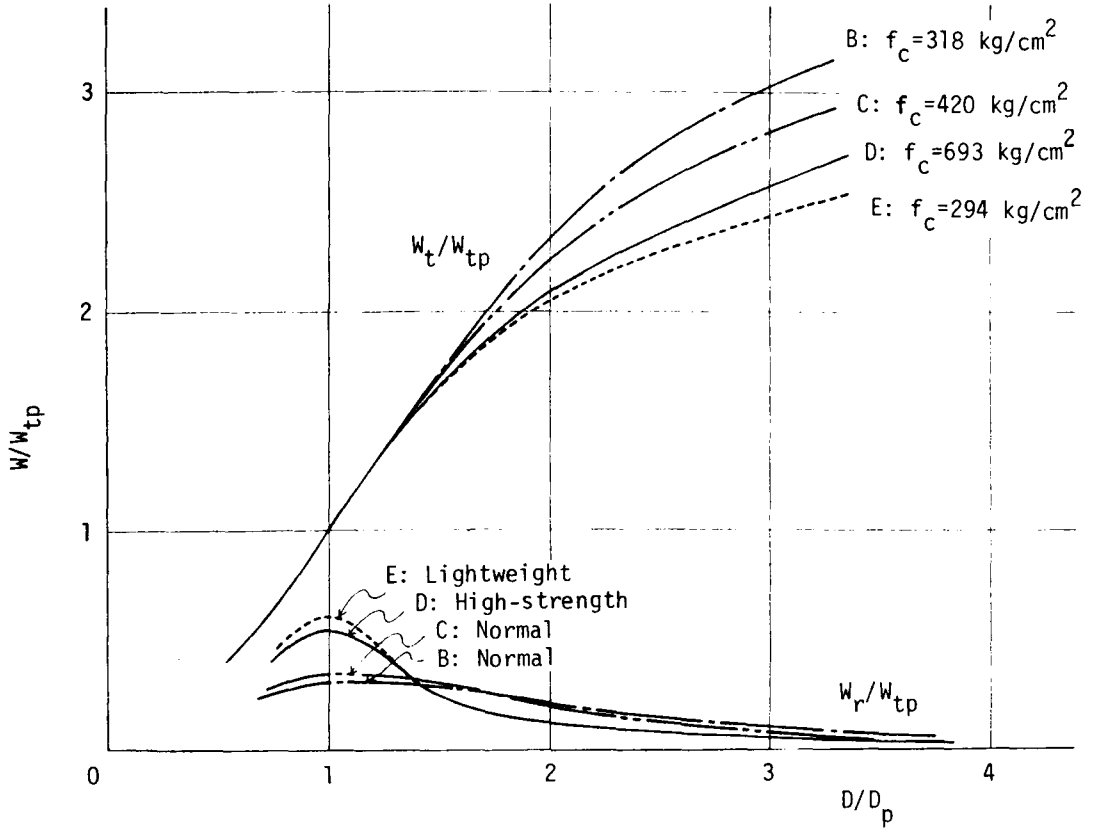

Fig. 4.6. Effect of Concrete Qualities on Energy-Displacement Relationships.

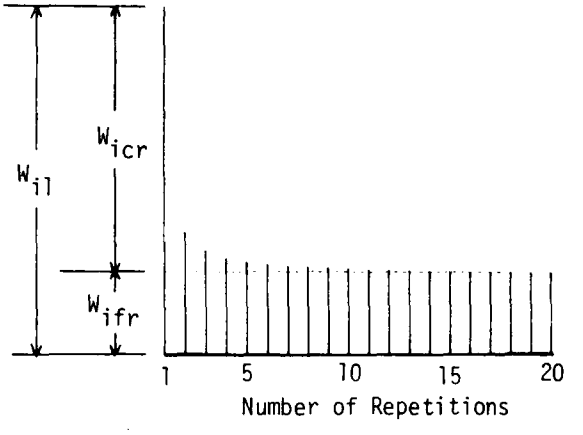

Fig. 4.7. Dissipated Energy and Load Repetition.

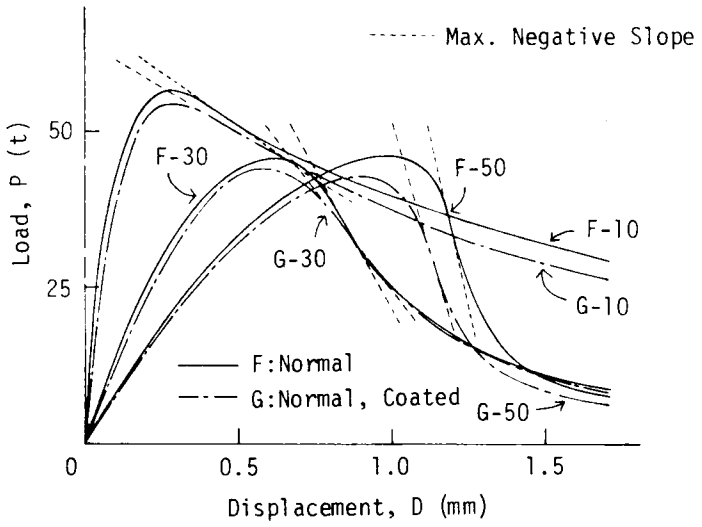

Fig. 4.8. Load-Displacement Diagrams of Normal Concretes.

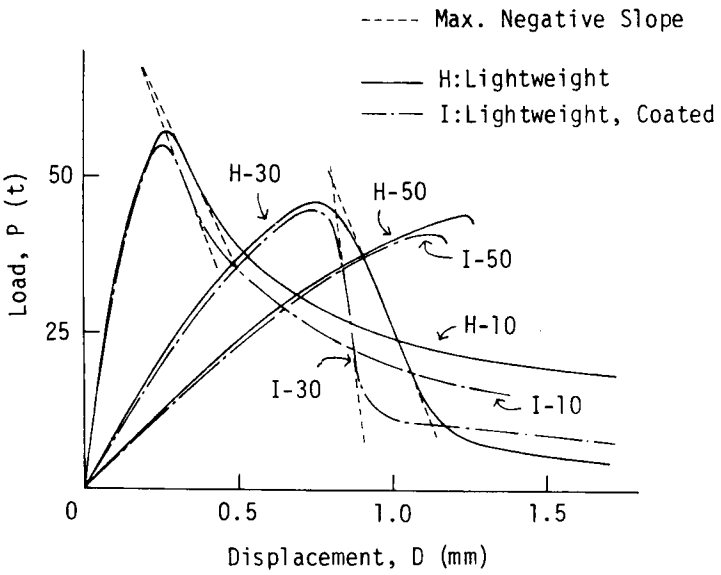

Fig. 4.9. Load-Displacement Diagrams of Lightweight Concretes.

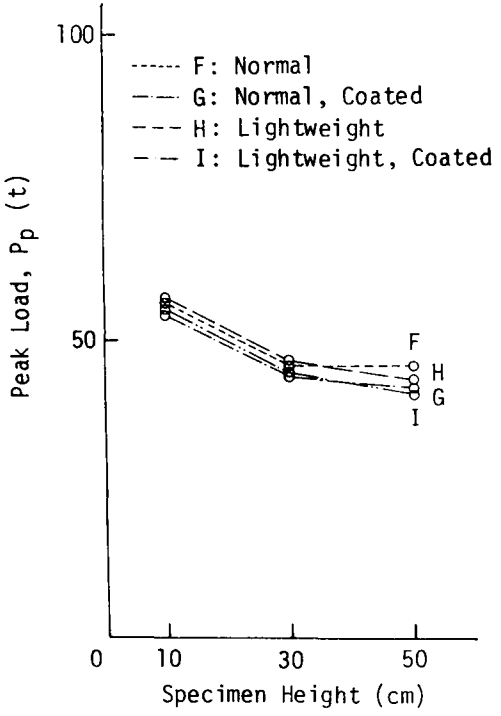

Fig. 4.10. Peak Load.

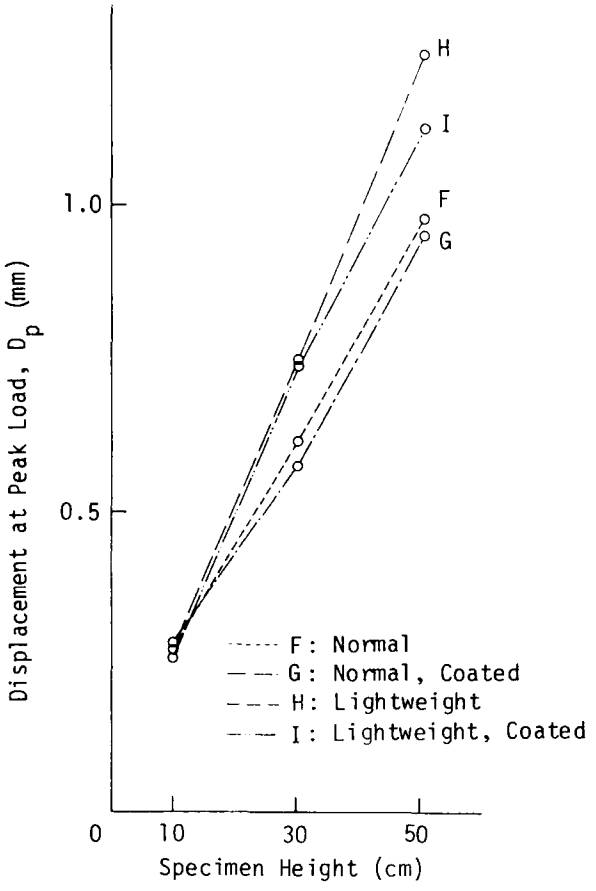

Fig. 4.11. Displacement at Peak Load Point.

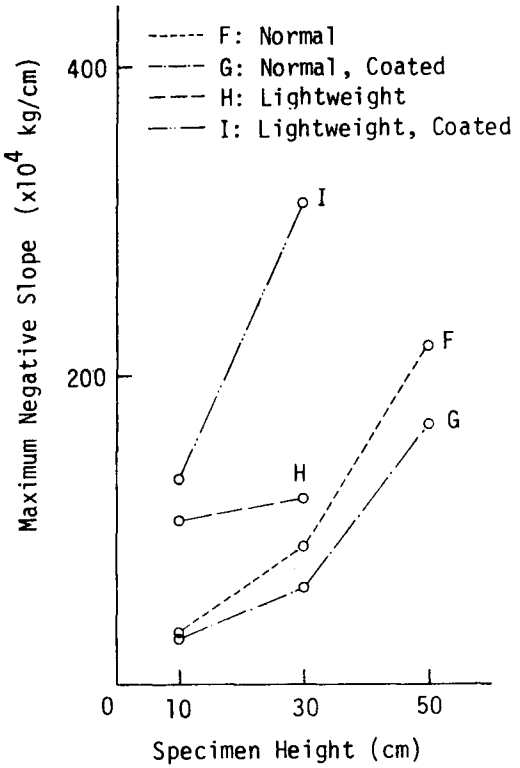

Fig. 4.12. Maximum Negative Slope.

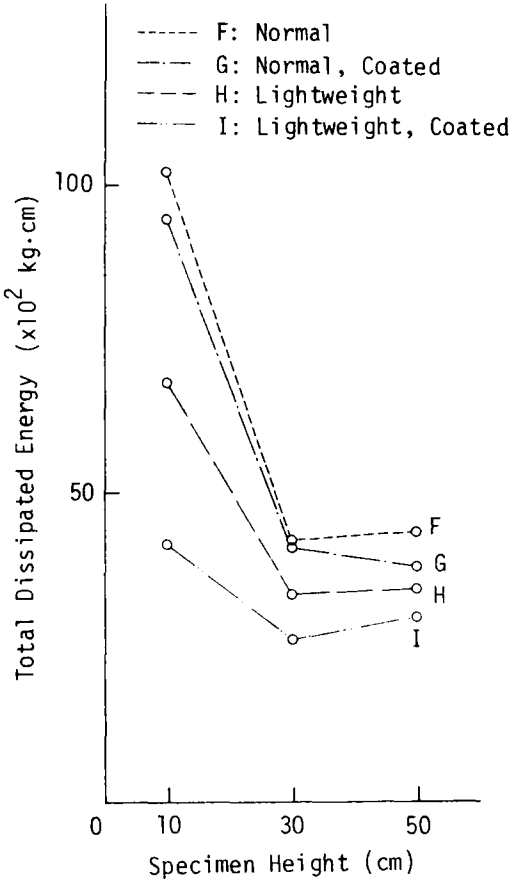

Fig. 4.13. Total Energy Dissipation.

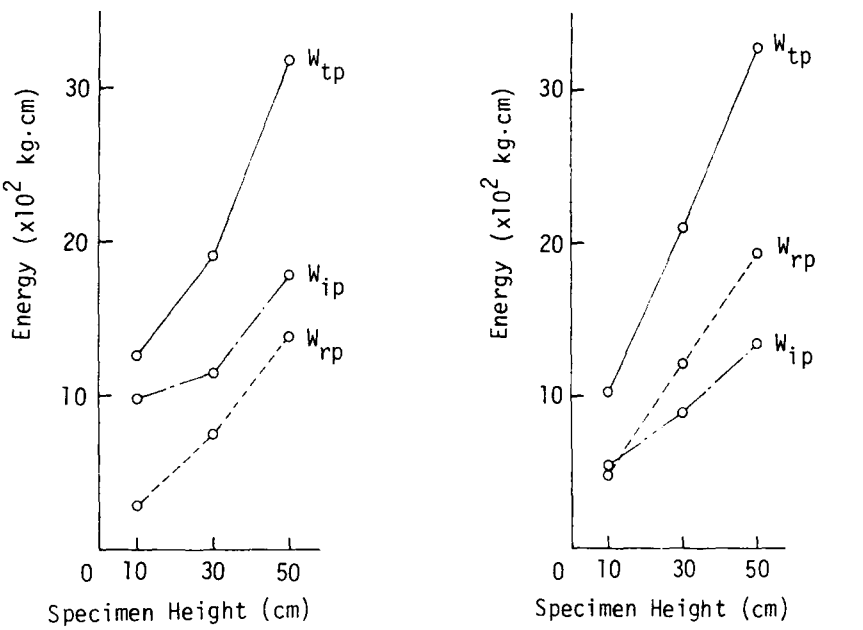

Fig. 4.14. Energies at Peak Load.

CHAPTER 5. FLEXURAL FAILURE PROCESS OF REINFORCED CONCRETE BEAMS

5.1 INTRODUCTION

If structures were ductile enough to absorb energy, their collapse during a major earthquake could be avoided and human life saved. Thus, ductility is one of the most important properties of members and structures.

In this chapter, energy dissipation in the flexural failure process of RC beams (reinforced concrete beams), which are considered to be composite members of concrete and steel bars, is related to ductile behavior. In the failure process of RC beams under flexure, the work done, W_t, to the beams due to externally applied loads is divided into W_r and W_i. W_r is the strain energy stored in the beams and W_i is the dissipated energy consumed in the beams. This dissipated energy, W_i, consists of two components, W_{ic} and W_{is}; W_{ic} is the energy dissipated in the concrete mainly as a surface energy and W_{is} is the energy dissipated in the plastic deformation of reinforcement after yield. A part of the strain energy in the beams may be transformed gradually into dissipated energy, W_i. From tests of RC beams with different reinforcement ratios, which were loaded beyond the peak load, the energies dissipated in the reinforcement and concrete were calculated, and the role of the reinforcement and concrete in the energy dissipation was considered. The dissipated energy was related to the displacement and fracture phenomena of the RC beams. The number of AE (Acoustic Emissions) generations during the failure process of the beams was counted, and then the relationship between the number of AE generations and the energy dissipation in the reinforcement and concrete was investigated.

The method of evaluating the plastic rotation capacity of RC beams based on measured plastic curvature and dissipated energy in the reinforcement was employed.

From the material presented in this chapter, some useful knowledge for evaluating the ductility and behavior of RC beams at the ultimate limit state was obtained.

5.2 EXPERIMENTAL PROCEDURES

5.2.1 Test Program and Fabrication of Beams

Three RC beams with different reinforcement ratios, 0.83%, 2.53% and 6.18%, were used in order to change the relation between the yield of the reinforcement and the crushing of concrete for the RC beams under flexure. The first reinforcement ratio, 0.83%, is nearly a balanced one in the working stress design. The third one, 6.18%, represents over-reinforcement even in the ultimate strength design. In this case, the crushing of concrete occurs without the yield of the reinforcement. The three RC beams were reinforced with three sizes of deformed reinforcing bars, 10 mm, 16 mm, and 25 mm in nominal diameter, respectively. Therefore, hereafter these beams are called a B10, B16 and B25.

The dimension of the beam specimens was 10x20x160 cm. As shown in Fig. 5.1, stirrups were used to prevent shear failure. The stirrups (6 mm diameter bars) were spaced so that the stress in the stirrups at the maximum shear load was less than the yield strength of the bars. The concrete cover for the reinforcement was 2.3 cm. The effective depth and the spacing of the stirrups for each beam are presented in Table 5.1. The machanical properties of the reinforcing bars are given in Table 5.2. The strain in

the reinforcing bars at yield was measured with plastic strain gages (gage length: 5 mm).

Concrete was made from normal Portland cement, crushed sandstone (specific gravity: 2.64, maximum size: 15 mm), and river sand (specific gravity: 2.61, fineness modulus: 3.0). The mix proportion of the concrete and the measured slump are given in Table 5.3.

All beam specimens were cast at the same time. After unmolding, they were cured in the testing room and loaded at the testing age of from 41 to 43 days. The average compressive strength of concrete, f_c, calculated from 7 cylindrical specimens (ϕ10x20 cm) was 316 kg/cm^2. The standard deviation was 12.1 kg/cm^2 and the coefficient of variation was 3.9%.

5.2.2 Loading and Measuring of Displacement

The RC beams were loaded at the span of 130 cm, as illustrated in Fig. 5.1, by using an Amsler type testing machine with 200t capacity. Several cycles of loading and unloading were carried out increasing the maximum load-point displacement with each repetition by a constant rate (approximately 5 mm/min.). The minimum load level after each unloading was between 0.2 t and 0.4 t.

The displacement (deflection) of the beams, the strain in the steel bars and concrete, and the number of AE generations were measured.

Five dial-gage type electric displacement meters were used to measure the displacement (deflection) of the beams. As shown in Fig. 5.2, the meters were fixed to a supporting bar, which was directly attached to the beams at two points over the loading span to eliminate error in the measured displacement due to seating of support points and deformation of the loading machine, etc. One of the attaching points was

rotatable and the other was rotatable and slidable. Two load cells placed in series were used. An X-Y recorder recorded the relation between the load-point displacement, which was detected with a displacement meter under one of the load-points, and the load, which was detected with one of the load cells. Hereafter, this relationship is called the load-displacement diagram. The out-puts from the other load cell and the displacement meter under the other load -point were printed on recording paper with a digital printer. The displacements measured at the two load-points were almost the same.

The change in the lengths between gage points, which were glued at 25.4 cm (10 in.) horizontal intervals at the same height on the side surface of the concrete as shown in Fig. 5.3, were measured with a Whittemore strain meter (least count: 0.025 mm, gage length: 25.4 cm) to determine the deformation of the reinforcing bars along the axis of the beams. When the deformation between marked points became greater than 1.3 mm due to cracking, a caliper (least count: 0.1 mm) was used to measure the deformation instead of the Whittemore strain meter. The change in the lengths between gage points, which were placed at 5.08 cm (2 in.) horizontal intervals in four lines and five columns as shown in Fig. 5.3, was measured with a 5.08 cm (2 in.) length Whittemore strain meter in order to find the position of the neutral axis and the strain distribution across the depth of the beams. The load-point displacement was kept constant during the measuring. The strain in the reinforcement was measured at the center of the moment span (constant moment region) and under the load-points with electric resistance strain gages (gage length: 5 mm) glued to the reinforcing bars. The strain in concrete was measured at

both the compression fiber (top surface) and the tension fiber (bottom surface) inside the moment span with electric resistance strain gages (gage length: 67 mm). The strains in concrete and steel were printed out with the digital printer.

The number of AE generations was counted with a pickup, which was attached at the center of the side surface of the beams. The AE's had a frequency of from 20 to 300 kHz, were amplfied to 60 dB, and were over 100mV. The details of the AE detecting method are reported in Reference [30].

5.2.3 Calculation of Energy

The work done, W_t, which is applied to the specimen by an external load, is transformed into reversible elastic strain energy, W_r, which is stored in the specimen, and into irreversible dissipated energy, W_i, which is absorbed in the specimen. In the study of this chapter, the dissipated energy W_i was divided into W_{ic} and W_{is}, and they were calculated. W_{ic} is the energy dissipated in the concrete as surface energy, and W_{is} is the energy dissipated at the yield of the steel. Each energy was calculated in the following way. The area OUQ defined by the loading curve OU and the displacement axis in Fig. 5.4 indicates the work done, W_t, applied to the beam up to the unloading point U in the load-displacement diagram. It can be formulated in terms of the externally applied load, P, and load-point displacement, D, as follows:

$$W_t = 2\int_0^Q \frac{P}{2}\, dD$$

$$= \int_0^Q PdD \qquad (5.1)$$

The dissipated energy W_i corresponding to the unloading point U, is calculated from the area OUR, which is defined by both the loading curve OU up to the point U, and the unloading curve UR. The reversible elastic strain energy W_r is given by the area RUQ under the unloading curve UR. In analyzing the data, the envelope curve connecting unloading points was used as the loading curve. These areas were measured with a planimeter.

As illustrated in Fig. 5.5, the dissipated energy at the yield of the reinforcement, W_{is}, was calculated from the product of P_{sy}, the yield load of the reinforcing bars, by D_{si}, the irrecoverable deformation measured along the beam axis at the position of the reinforcement after unloading. The work hardening of the reinforcing bars was not considered in this study. The details of the calculation of W_{is} are described in Section 5.4.

The dissipated energy in the concrete, W_{ic}, was calculated by subtracting W_{is}, the dissipated energy in the reinforcement, from W_i, the total dissipated energy in the beam. That is, $W_{ic} = W_i - W_{is}$. W_{ic} may include not only the energy dissipated as surface energy in compression and tension zones of the concrete but also the energy dissipated in the bond fracture between the reinforcing bars and concrete.

The width of the diagonal cracks at the shear spans of each beam after unloading was so small that the stirrups were considered not to have yielded. Thus, the effect of the stirrups on the dissipated energy could be considered negligible.

5.3 LOAD-DISPLACEMENT DIAGRAM OF RC BEAMS

The load-displacement diagrams of the RC beams, B10, B16 and B25, are given in Figs. 5.6, 5.7 and 5.8, which were

displayed on the X-Y recorder. In general, the load-displacement diagrams of RC beams in flexure are characterized by crack initiation, yield of reinforcement, strength failure (peak load), crushing of concrete in the compression zone, and post-failure region, etc. Since Figs. 5.6, 5.7 and 5.8 show the diagrams of the entire failure process of the RC beams in flexure, the points of crack initiation are not clear in these figures. The line after 3.4 cm in displacement in Fig. 5.6 of Beam B10 was plotted from the data printed out by the digital printer.

The initial points of yield of the reinforcement and of crushing in the concrete are marked in Figs. 5.6, 5.7 and 5.8. The initial point of steel yielding was defined as a critical point, where the strain in the reinforcing bars measured with strain gages began to increase suddenly. The critical strain was $2100 \sim 2200 \times 10^{-6}$. It was identical with the strain at beginning of yield in the tension test of the reinforcing bars. The beginning of crushing in the concrete was determined by observation with naked eye. The critical point coincided with the point where the compression strain, which was measured with the strain gages glued on the compression surface of the beams, deviated by about $1500 \sim 2500 \times 10^{-6}$ from the strain, which was calculated from the distribution of deformation measured with the Whittemore strain meter. As an example, Fig. 5.9 shows a comparision between the two kinds of compression strains of Beam B16: One was measured with the strain gage and the other was calculated from the distribution of deformation. It can be seen from Fig. 5.9 that the value of the compression strain measured with the strain gage was reliable only up to the value of $3500 \sim 4000 \times 10^{-6}$.

In the case of Beam B10 with the low reinforcement ratio, after the reinforcing bars reached the yield strength at a displacement of 0.30 cm, the beam displacement incresed greatly with a small increase in load until the onset of crushing in the concrete at a displacement of 2.40 cm. After the peak load point, the load-displacement relationship curved in a decline.

In the case of Beam B16, the reinforcement began to yield at a displacement of 0.48 cm, and then the concrete began to crush in compression at a displacement of 0.83 cm. After the onset of crushing, the rate of load decrease was accelerated with the progress of concrete failure.

In the case of Beam B25 with over-reinforcement, the reinforcing bars did not yield, and the displacement at the peak load was 0.65 cm. The load-displacement curve after compression failure was the steepest. The displacement at the onset of concrete crushing was 0.70 cm.

The effect of the reinforcement ratio on the ductility of each beam is described in Section 5.7.

The yield load of each beam, P_y, which was measured at the initiation of the yield of the reinforcement, the peak load, P_p, and the moments corresponding to each load are presented in Table 5.4. The yield moment of each beam, M_{yc}, was calculated from the following formula using f_{sy}, the yield strength of deformed reinforcing bars, and f_c, compression strength of concrete:

$$M_{yc} = pf_{sy} \left(1 - \frac{pf_{sy}}{2f_c}\right) Bd^2 \qquad (5.2)$$

where, p is the reinforcement ratio, B is the width of the beam, and d is the effective depth.

M_{yc} of Beam B25 was not calculated with the above formu-

la, since the reinforcement did not yield. The measured yield moments, M_{ym}, of Beams B10 and B16 are about 15% greater than the calculated yield moments, M_{yc}. It has been reported that small size model beams reinforced with deformed bars give this result [52]. One of the reasons may be that the strain in the reinforcement near the cracks in the concrete became large enough for work hardening, because of the higher bond strength of the deformed bars. The details of these reasons should be examined further. Since the purpose of this investigation is to roughly separate the dissipated energies in the concrete and in the steel during the failure process of RC beams in flexure, the effect of the work hardening of reinforcement on the calculation of the dissipated energy was not taken into consideration.

5.4 DEFORMATION AND ENERGY DISSIPATION IN CONCRETE AND REINFORCEMENT

Fig. 5.10 shows the relationship between the displacement (deflection) of the beams and the distribution of the tensile deformation, which was measured between the five sets of gage points on the concrete surface along the reinforcement. The tensile deformation along the reinforcement increased and was concentrated in the moment span as beam displacement increased. This fact means that large flexure cracks in the concrete as well as plastic deformation in the reinforcement were concentrated in the constant moment region. For Beam B25 with the large reinforcement ratio, the load-carrying capacity decreased rapidly after peak load as shown in Fig. 5.8. As a result, deformation in the shear spans remarkably recovered after the displacement corresponding to the peak load point.

Because of the local extension of reinforcement at cracked portions, the distribution of tensile deformation in the reinforcement may not exactly coincide with that of the concrete surface shown in Fig. 5.10. However, when the end anchorage of the reinforcement is sufficient, the total deformation of the reinforcement is considered to be equal to the total deformation of the concrete along the reinforcement. In this study, the total deformation of the reinforcement was measured on the concrete surface along the reinforcement. That is, the deformation was measured at five sections, which were marked with small plugs on the concrete surface at intervals of 25.4 cm (10 in.). Therefore, the total gage length was 127 cm within the beam span of 130 cm.

Figs. 5.11, 5.12, and 5.13 show the relationship between the beam displacement and the total deformation of reinforcement in Beams B10, B16, and B25. In these figures, the circle shows the deformation of the reinforcement at an unloading point. The black point shows the irrecoverable deformation at the minimum load after unloading, relating to the beam displacement at the previous unloading point.

In the case of Beam B10, the irrecoverable deformation increased rapidly and constantly with beam displacement after the yield of the reinforcement. The irrecoverable deformation just before the yield was 0.43 mm. This may include the elastic deformation due to the minimum load after unloading. Therefore, the irrecoverable deformation just before the yield was subtracted from the irrecoverable deformation at each unloading point, when the dissipated energy in the reinforcement, W_{is}, was calculated. W_{is} was calculated by multiplying the yield load of the reinforcements by the irrecoverable deformation, which is indicated by oblique

lines in Fig. 5.11.

Also for Beam B16, the irrecoverable deformation just before the yield was subtracted from the irrecoverable deformation at unloading points in the calculation of W_{is}. In the region above a beam displacement of 2 cm in Fig. 5.12, the load decreased remarkably and the load at the final unloading point was about one seventh of the peak load. Moreover, Fig. 5.10 (b) indicates that the elastic deformation might be almost completely recovered when the beam displacement is large. Therefore, the irrecoverable deformation without any subtraction was used in the calculation of W_{is} at the final unloading point. As seen from Fig. 5.12, there was a critical point after the peak load point where the total deformation of the reinforcement began to decrease. This point coincided with the point where the irrecoverable deformation of the reinforcement stopped increasing.

Although the total deformation of the reinforcement in Beam B25 at the peak load point was 0.96 mm, the total deformation at the final stage was nearly zero, because the reinforcement did not yield.

The elastic strain energy, W_r, the total dissipated energy, W_i, the energy dissipated in the reinforcement, W_{is}, and the energy dissipated in the concrete, W_{ic}, of each beam are related to the beam displacements at unloading points in Figs. 5.14, 5.15, and 5.16. The onsets of reinforcement yield and of concrete crushing are marked in these figures. The initial portions of Figs. 5.14, 5.15, and 5.16 are magnified into Figs. 5.17, 5.18, and 5.19, in order to clarify the character of the energy dissipation in the region of small beam displacement.

As seen from Figs. 5.14 and 5.17 related to Beam B10, the

increase in the total dissipated energy, W_i, after yield of the reinforcement was large. Especially the dissipated energy in the reinforcement, W_{is}, remarkably increased in proportion to the beam displacement after yield, and then W_{is} exceeded W_{ic}, the dissipated energy in the concrete, at a displacement of 0.6 cm, which was about twice the displacement at yield. W_{ic} existed from the beginning of loading, and constantly increased as the beam displacement increased. The elastic strain energy, W_r, increased with the beam displacement before the reinforcement began to yield, but after yield, W_r was almost constant at about 4×10^2 kg·cm.

It can be seen from Figs. 5.15 and 5.18 that W_{is} of Beam B16 increased after the yield of the reinforcement, as did Beam B10, but became constant at a displacement of 1.7 cm (which was four times larger than that at the initiation of yielding) due to the decreasing load. After this point, energy was dissipated only in the concrete. W_{ic} was always greater than W_{is}, and W_r decreased as the load-carrying capacity decreased.

The reinforcement of Beam B25 did not yield as shown in Figs. 5.16 and 5.19. Therefore, only the concrete contributed to energy dissipation. W_r was maximum at peak load just before the beginning of concrete crushing, and then decreased with a decrease in the load.

It can be seen from the comparison of Figs. 5.14 through 5.19 that an RC beam with high reinforcement ratio tends to have relatively large W_{ic} and small W_{is}. Before yield of the reinforcement, energy was consumed only in the concrete. The peak loads depending on the reinforcement ratios were so different that there was also a large difference in the total dissipated energies at the yielding of the reinforcement and

at the crushing of the concrete. But, when the beam displacement was sufficiently large, about 4 cm, and the load decreased, W_i was about 2×10^4 kg·cm for the three beams and did not depend on the reinforcement ratios.

Photographs of the failed beams are shown in Figs. 5.20, 5.21 and 5.22. In the case of Beam B10, the depth of concrete spalling due to compression failure was small even at the final stage, although both the irrecoverable crack width and deformation of the reinforcement were great. Beams B16 and B25 with large W_{ic} had a larger depth of concrete spalling due to compression failure than Beam B10 with small W_{ic}.

5.5 NEUTRAL AXIS AND CURVATURE

Fig. 5.23 shows the strain distribution in the moment span, which was measured using the gage points (2 in. spacing x 4 lines) on the side surface of the beam. The strain distributions in Fig. 5.23 were almost linear, so that the assumption of plain sections seemed to be satisfied. Only when the displacement of Beam B10 was great, was the strain distribution in the concrete not linear at the reinforcement level. The neutral axis positions calculated from Fig. 5.23 are related to the beam displacements in Figs. 5.24, 5.25, and 5.26. The open points in Figs. 5.24, 5.25, and 5.26 show the beam deflection where the strain distribution in Fig. 5.23 was measured.

The neutral axis of Beam B16 rose with beam displacement after yield of the reinforcement, and reached its maximum level at the beginning of crushing in the concrete. After that, spalling in the concrete in compression due to failure caused the neutral axis to descend toward the reinforcement

in order to maintain the balance of the moment.

In the case of Beam B10 with the low reinforcement ratio, the neutral axis rose immediately after yield of the reinforcement. The depth of the compression zone was so small that the change in position of the neutral axis and the depth of spalling were small, even when displacement was large.

Because Beam B25 was over-reinforced, the neutral axis was always below the center line of the cross-section. The depth of the compression zone increased and the neutral axis approached the reinforcing bars as beam displacement increased. The depth of concrete spalling was very large.

The location of the neutral axis was calculated from the distribution of the strain averaged over the area, including both cracked and uncracked portions. Therefore, the neutral axis in sections where cracking had occured might be higher (see Figs. 5.20, 5.21, and 5.22). The calculated compression strains at the outer extreme concrete fiber at the beginning of crushing were very large, about $5\times10^{-3} \sim 8\times10^{-3}$.

At the beginning of loading, beams had uniform flexural stiffness and behaved elastically. The displacement of the beams can be determined by elastic analysis. After the externally applied moment reached the flexural crack moment, the flexural stiffness decreased due to flexural cracks. The curvature, that is the rotation of the section, is assumed to be uniform over the moment span hereafter, though microscopically it would be uneven due to the flexural cracks.

The load-point displacement, D, consists of two components, D_1 due to rotation in the shear spans L_1, and D_2 due to the rotation in the moment span L_2. That is, $D = D_1 + D_2$. L_1 and L_2 are shown in Fig. 5.1.

When the beam in the shear spans is stiff, D_1 is equal

to zero and D_2 can be expressed as follows:

$$D_2 = D = \Phi L_1 L_2/2 \tag{5.3}$$

where, Φ is the averaged curvature in the moment span L_2. The curvature, Φ, was calculated from the distribution of the averaged strain in the moment span shown in Fig. 5.23.

When the flexural stiffness, EI, is uniform over the beam, elastic analysis gives the components of the displacement:

$$D_1 = PL_1^3/6EI = ML_1^2/3EI \tag{5.4}$$

$$D_2 = \Phi L_1 L_2/2 = ML_1 L_2/2EI \tag{5.5}$$

where, P is the applied load, and M is the moment in the moment span due to P. The shear span of the beam, L_1, was 50 cm, and the moment span, L_2, was 30 cm. Therefore,

$$D_1/D_2 = 2L_1/3L_2 = 10/9 \tag{5.6}$$

$$D_2 = 9D/19 \tag{5.7}$$

Fig. 5.27 shows the relation between the beam displacement and the measured curvature in the moment span. In this figure, the point of Peak load-2 for Beam B10 is not the actual peak load point; however, it is treated as the peak load hereafter, because Fig. 5.6 shows that it was not affected by loading rate and load repetitions. The difference between the load at this point and the measured peak load was small.

Line-A in Fig. 5.27 shows the case in which rotation of

the section is concentrated in the moment span and the displacement due to rotation in the shear spans is negligible. It is obtained from Equation (5.3):

$$\Phi = 2D/L_1L_2 \tag{5.8}$$

Line-B shows the case in which the flexural stiffness is uniform over the length of the beam. From Equations (5.4) and (5.7):

$$\Phi = 18D/19L_1L_2 \tag{5.9}$$

As seen from Fig. 5.27, the beams behaved elastically before yield of the reinforcement. After yield, as the beam displacement increased, the curvature of Beams B10 and B16 increased, the graph running parallel to Line-A, which indicates the curvature was concentrated in the moment span. That is, after yield of the reinforcement,the beam displacement mainly increased due to an increase in the curvature in the moment span.

5.6 ACOUSTIC EMISSION IN RC BEAMS

The relationship between the number of AE generations and the beam displacement is indicated in Figs. 5.14 through 5.19 by a dotted line.

In the case of Beam B10, the number of AE generations rapidly increased before yield of the reinforcement. When beam displacement exceeded 0.5 mm after the yield point, the rate of AE generations became slow. This tendency probably reflects the increase in the size and number of cracks in the concrete and of bond cracks between concrete and steel.

For Beam B25, the number of AE generations began to increase suddenly at the initiation of concrete crushing. It

seems that for the most part AE's are generated during the compression failure of concrete. When the beam displacement became large, AE's could not be measured because the pickup fell off due to the crushing of the concrete.

The number of AE generations was small at the beginning of loading, and then increased constantly until the yielding of the reinforcement in Beams B10 and B16, or until the crushing of the concrete in Beam B25. By comparing the number of AE generations with the dissipated energies, it can be seen that the shape of the curve of AE generations was similar to that of the energy dissipated in the concrete, W_{ic}. This fact suggests that most of the AE's were generated in the concrete. To verify this,not only the number of AE generations but also the mechanism of AE should be studied. The method of detecting crack source location by AE would be useful.

5.7 PLASTIC ROTATION CAPACITY

The change in curvature from the beginning of reinforcement yield to the observed crushing of concrete, or to the equivalent gage-measured strain in compression fiber (for example, 3000×10^{-6}), has been used to evaluate the plastic rotation capacity, the capacity of RC beams to act as a plastic hinge. Also the deflection of beams after yield has been used to evaluate this capacity [53]. Besides such a steel hinge effect, which is caused by the yield of the reinforcement, there is also a concrete hinge effect, which is caused by the crushing of the concrete in the compression zone. Because the capacity of the latter is small, only the steel hinge effect has been investigated.

As seen from Figs. 5.6 and 5.7, the load was almost constant between the yield point and the concrete crushing

point. As described above, the change in deflection or curvature, which is calculated from the strain distribution in Fig. 5.23, from the yield point of the reinforcement to the crushing point of the concrete can be used to evaluate the plastic rotation capacity of the beams. The dissipated energy during the above period may be directly related to the plastic rotation.

When the flexural yield moment, M_y, causes the plastic curvature, Φ_p, in the constant moment span, L_2, then the dissipated energy, W_i, due to plastic rotation is as follows:

$$W_i = \int_0^{L_2} M_y \Phi_p dx \qquad (5.10)$$

As described in Section 5.5, the curvature after the yield of the reinforcement was concentrated in the moment span, L_2. If the plastic curvature Φ_p can be assumed macroscopically uniform, the plastic curvature Φ_p and the dissipated energy W_i are related by the following equation:

$$\Phi_p = W_i / M_y L_2 \qquad (5.11)$$

The starting point of plastic rotation in the steel hinge effect is the starting point of yield in the reinforcement. The initiation of concrete crushing has been usually used as the end point. The point where the energy dissipation in the reinforcement stops could also be used as the end point of the steel hinging. Fig. 5.28 shows the relationship between reinforcement ratio and beam displacement at the onset of reinforcement yield, at the initiation of concrete crushing, and at the end of the steel hinge effect defined above. The relationship between the moment and the curvature

is given in Fig. 5.29. The definition of peak load in Fig. 5.29 is the same as that in Fig. 5.27. As seen from these Figures, the beam displacement and the curvature at the onset of reinforcement yield increased slightly as the reinforcement ratio increased. But the displacement and curvature at the initiation point of concrete crushing, or the end point of steel hinging, decreased drastically with increase in the reinforcement ratio. Consequently, the displacement or curvature resulting from plastic rotation decreased as the reinforcement ratio increased. Though the moment carrying capacity of Beam B10 with the low reinforcement ratio did not decrease between the concrete crushing point and the end of steel hinging, the moment carrying capacity of Beam B16 with the higher reinforcement ratio did decrease slightly.

Assuming the flexural moment carrying capacity after the reinforcement yield point was constant, the plastic curvature Φ_p was calculated by Equation (5.11) from the dissipated energy W_i for two different regions: One from the yield point of the reinforcement to the crushing point of the concrete (named as Region-1), and the other from the yield point of the reinforcement to the end point of the steel hinging (named as Region-2). The measured plastic curvature, Φ_{pm}, in Fig. 5.29 and the calculated curvature, Φ_{pc}, are presented in Table 5.5. The values of Φ_{pm} and Φ_{pc} seem to be in agreement with each ether, in spite of the rough assumption regarding the duration of the plastic hinge effect and the lack of accuracy in Fig. 5.29. It can be concluded that the plastic rotation capacity can be directly related to the energy dissipated during rotation. The plastic rotation capacity for Beam B10 was greater than that for Beam B16, and the capacity for Region-2 was twice that for Region-1.

It has been pointed out that the plastic rotation capacity is related to the final ratio of the neutral axis [53]. The results in Table 5.5 are marked in Fig. 5.30, which is a trial calculation of the above described relation by Koyanagi [54] made by assuming the stress-strain curves of both steel and concrete to be bi-linear. In Fig. 5.30, the plastic curvature is normalized in terms of rotation as: $\theta_p = \Phi_p d$, where d is the effective depth. The curvature calculated from the dissipated energy, and the measured plastic curvature for Region-1 seem to be almost in agreement with the results in Fig. 5.30. The plastic rotation capacity for Region-2, (which ends at the point where the energy dissipation in the reinforcement stops), is about twice that for Region-1. The meaning of this phenomenon should be investigated further with relation to the moment redistribution in actual structures and to the load carrying capacity. The dissipated energy for Region-2 may be the parameter of the energy dissipation due to plastic rotation in the steel hinge. Therefore, the dissipated energy would be a useful means to study the rotation capacity of the plastic hinge and the failure process of RC beams under flexure.

5.8 CONCLUSION

RC beams with three reinforcement ratios (0.83%, 2.25% and 6.18%) were tested to investigate the role of reinforcement and concrete in energy dissipation during the flexural failure process of the beams. The relationship between the plastic rotation capacity and the energy dissipation in the RC beams has been discussed in this chapter.

The following results were obtained:

(1) The work done on the RC beams by an external load, W_t,

was separated into the reversible strain energy, W_r, and the dissipated energy, W_i. The energy dissipated in the reinforcing bars during yield, W_{is}, was determined from the irrecoverable deformation of the reinforcement. The energy dissipated in the concrete, W_{ic}, was calculated by subtracting W_{is} from W_i. The quantitative results show that as the reinforcement ratio increased, the energy dissipated in the concrete increased and the energy dissipated in the reinforcement decreased.

(2) The neutral axis position was calculated from the concrete strain distribution in the moment span. In the case of the beam with the low reinforcement ratio, the neutral axis rose with an increase in flexural moment and then descended after concrete crushing. In general, the greater the reinforcement ratio, the lower the position of the axis. Especially in the case of the over-reinforced beam, the neutral axis approached the reinforcing bars. The RC beam with high reinforcement ratio tended to have relatively large W_{ic}. At the concrete crushing point, the concrete compression strain calculated from the strain distribution was larger than that measured by the strain gages, which were glued on the compression face.

(3) After the yield of the reinforcement, the energy dissipated in the reinforcing bars increased with the beam displacement, then stopped increasing at a certain displacement, after which the energy was dissipated only in the concrete.

(4) The results of the curvature calculation in the moment span show that the beams behaved elastically before the yield of the reinforcement. After yield, the curvature

concentrated in the moment span. In the case of the beam with the high reinforcement ratio, elastic recovery of the deformation was observed in the shear span after concrete crushing, because of the concentration of the curvature in the moment span.

(5) The relation between number of AE generations and beam displacement was similar to the relationship between dissipated energy (especially the energy dissipated in the concrete) and beam displacement.

(6) The plastic rotation capacity of the RC beams decreased as the reinforcement ratio or the final neutral axis ratio increased. Both the plastic curvature calculated from the dissipated energy, and the measured plastic curvature, were almost in agreement with the plastic curvature computed on the basis of the simplified assumption that the stress-strain relationship is bilinear for both concrete and reinforcement. The plastic curvature or the energy dissipation in the range from onset of reinforcement yielding to end of energy dissipation in the reinforcement would be a useful index to evaluate the plastic rotation capacity of the steel hinging. However, this method should be investigated more thoroughly.

Table 5.1. Effective Depth and Stirrup Spacing.

Beam	Stirrup Spacing cm	Effective Depth d, cm
B10	10.0	17.2
B16	10.0	16.9
B25	7.5	16.4

Table 5.2. Mechanical Properties of Reinforcing Bars.

Reinforcing Bar	Nominal Dimensions: Diameter mm	Nominal Dimensions: Cross-Sec. Area mm^2	Yield Load P_{sy}, t	Yield Strength f_{sy}, kg/mm^2	Peak Load P_p, t	Tensile Strength f_{su}, kg/mm^2
Def. Bar (D10)	9.53	0.713	2.69	37.7	3.97	55.7
Def. Bar (D16)	15.9	1.986	7.06	35.5	10.49	52.8
Def. Bar (D25)	25.4	5.067	23.0	45.4	32.7	64.5
Plain Bar	6.0	0.283	1.20	42.4	1.32	46.6

Table 5.3. Mix Proportion.

Water-Cement Ratio	Sand-Aggr. Ratio	Mix Materials, kg/m^3: Water	Cement	Sand	Gravel 5~15mm	Slump cm
0.68	0.42	192	283	770	1084	4

Table 5.4. Yield Moment and Peak Moment of Beams.

Beam	Yield Load P_y, t	Yield Moment M_{ym}, t·m	Peak Load P_p, t	Peak Moment M_p, t·m	Cal. Yield Moment M_{yc}, t·m	$\frac{M_{ym}}{M_{yc}}$
B10	4.1	1.03	4.6	1.15	0.88	1.17
B16	9.5	2.38	9.6	2.40	2.07	1.15
B25	-	-	16.3	4.08	-	-

Table 5.5. Dissipated Energy and Plastic Curvature.

Beam	Region	Dissipated Energy W_i, $x10^4$ kg·cm	Calculated Plas. Curv. ϕ_{pc}, $x10^{-3}$/cm	Measured Plas. Curv. ϕ_{pm}, $x10^{-3}$/cm
B10	1	0.86	2.8	2.3
	2	1.68	5.4	4.3*
B16	1	0.39	0.6	0.7
	2	1.16	1.6	1.1

* More than 4.3

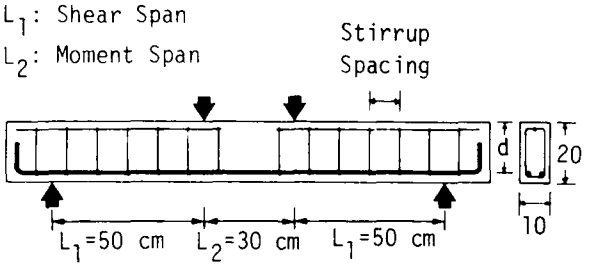

Fig. 5.1. Reinforcement in Beam.

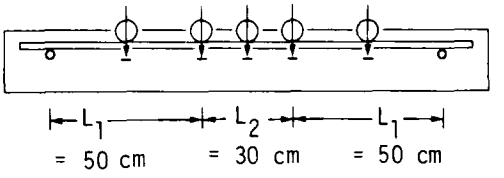

Fig. 5.2. Equipment for Measuring Deflection.

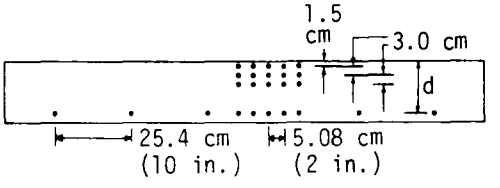

Fig. 5.3. Gage Points on Beam.

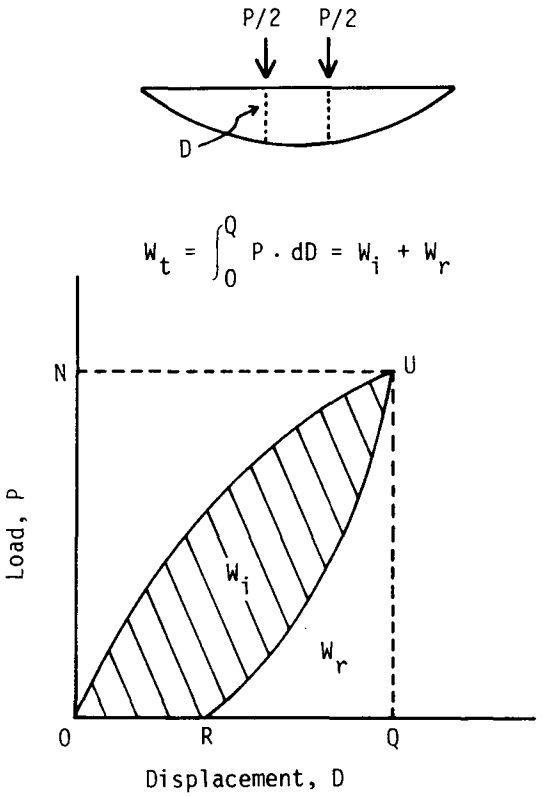

Fig. 5.4. Calculation of Energy.

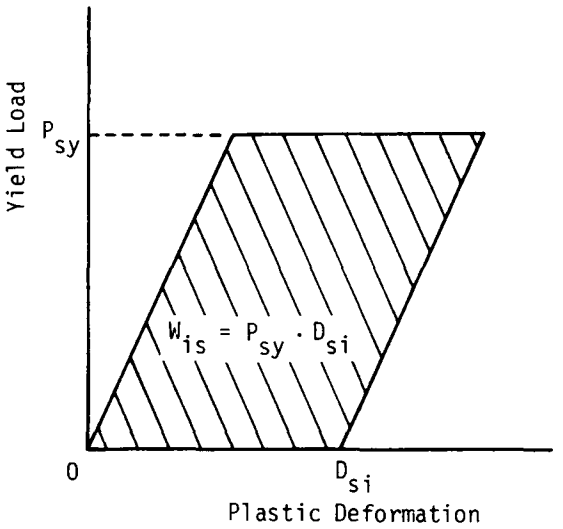

Fig. 5.5. Dissipated Energy in Steel.

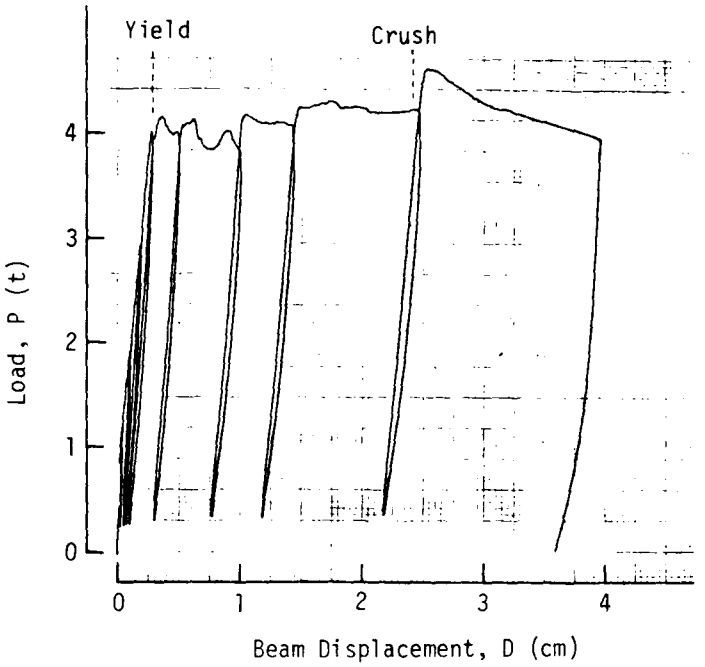

Fig. 5.6. Load-Displacement Diagram of Beam B10.

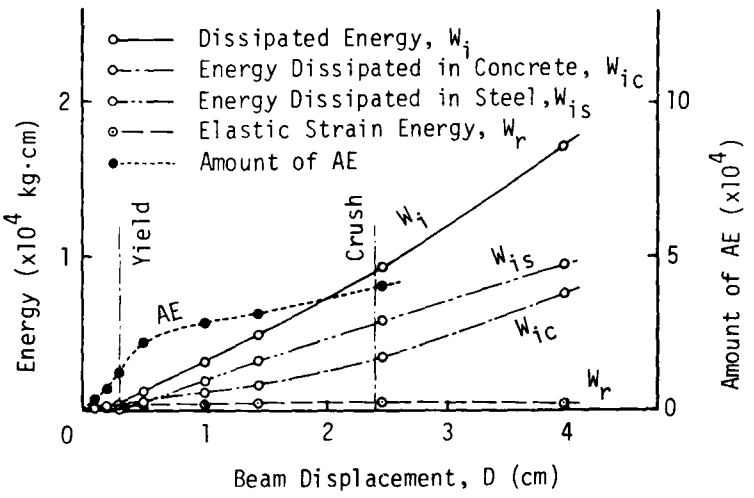

Fig. 5.14. Energy-Displacement Relationship of Beam B10.

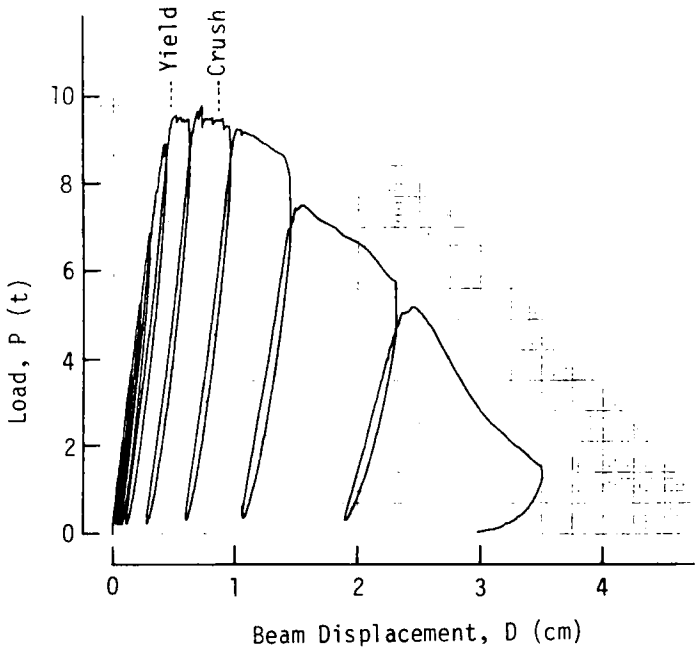

Fig. 5.7. Load-Displacement Diagram of Beam B16.

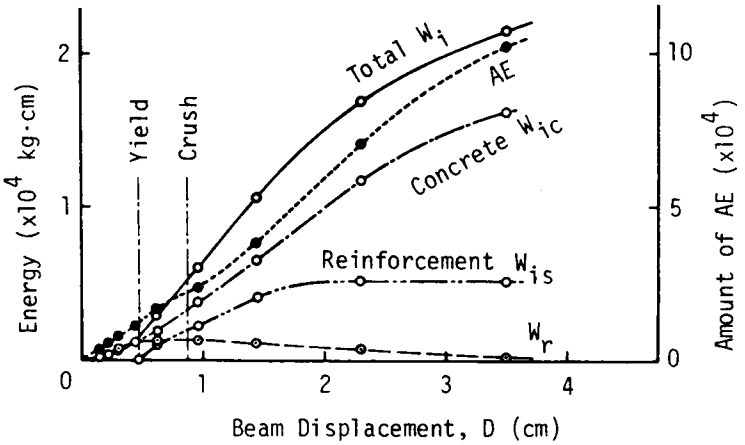

Fig. 5.15. Energy-Displacement Relationship of Beam B16.

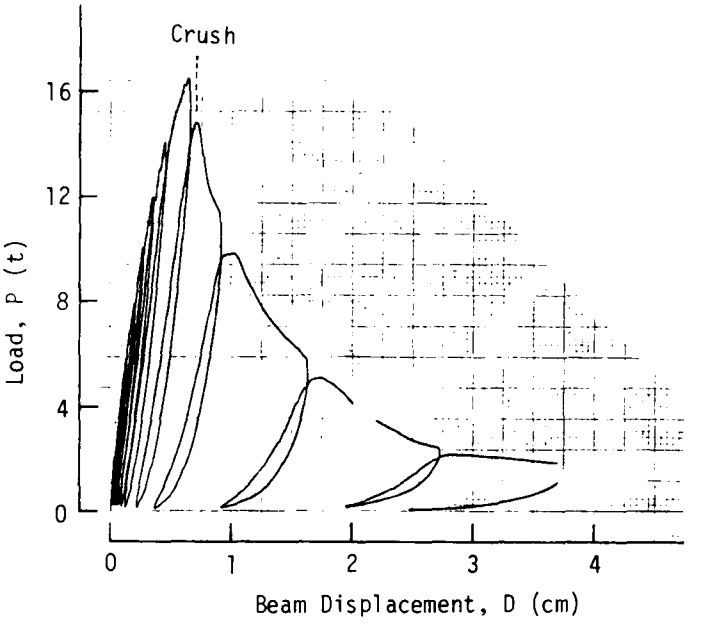

Fig. 5.8. Load-Displacement Diagram of Beam B25.

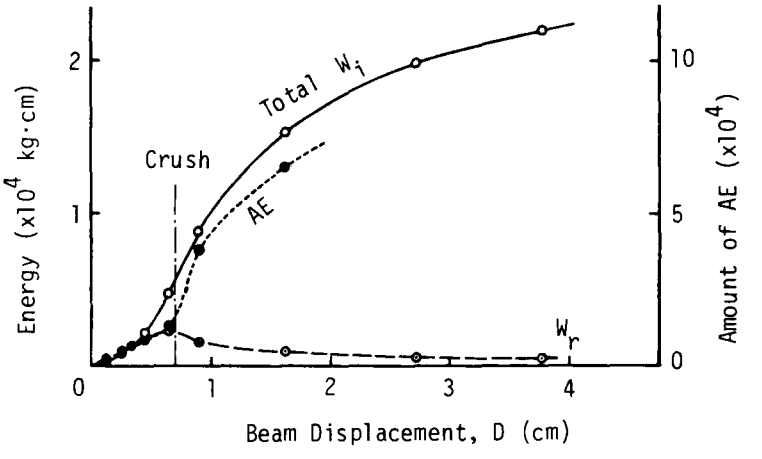

Fig. 5.16. Energy-Displacement Relationship of Beam B25.

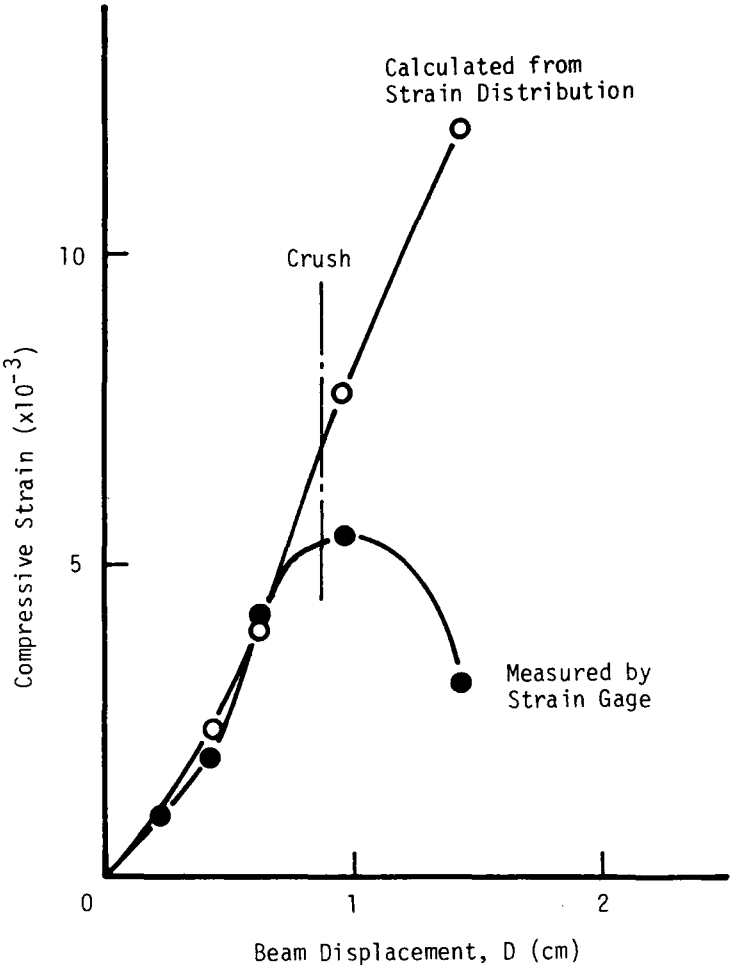

Fig. 5.9. Comparison of Compressive Strains.

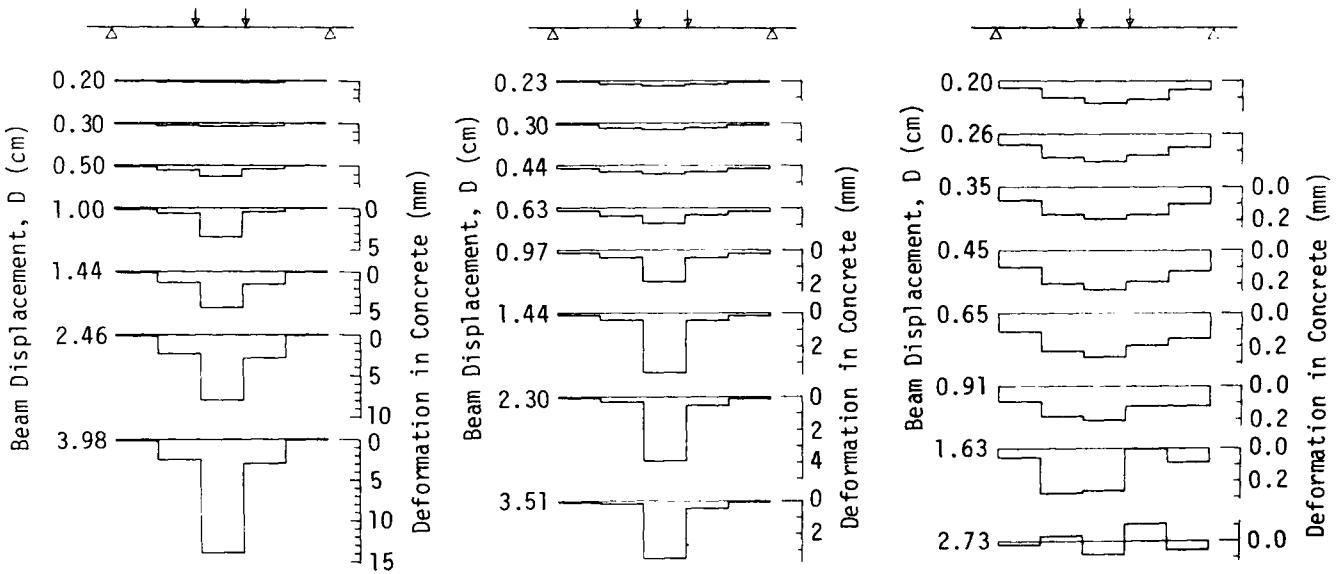

Fig. 5.10. Distribution of Tensile Deformation along Reinforcement.

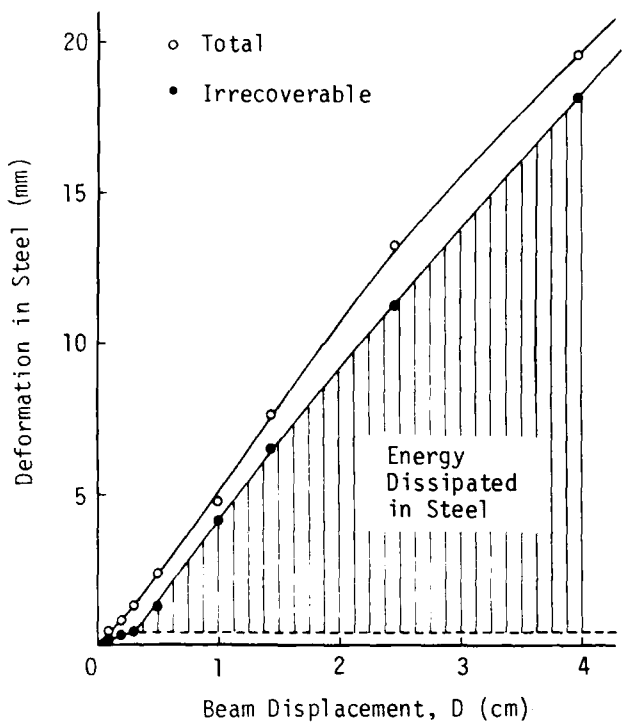

Fig. 5.11. Total Deformation of Reinforcement in Beam B10.

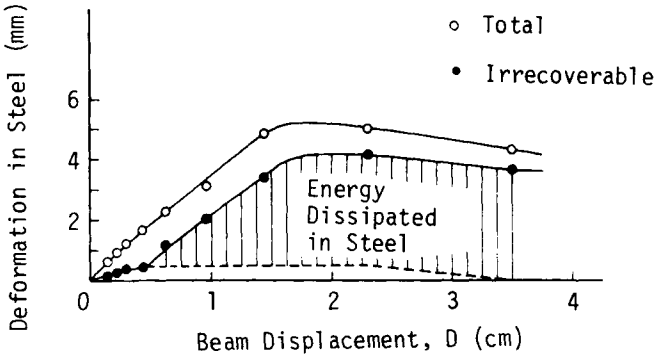

Fig. 5.12. Total Deformation of Reinforcement in Beam B16.

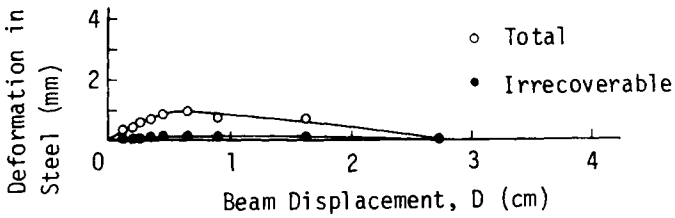

Fig. 5.13. Total Deformation of Reinforcement in Beam B25.

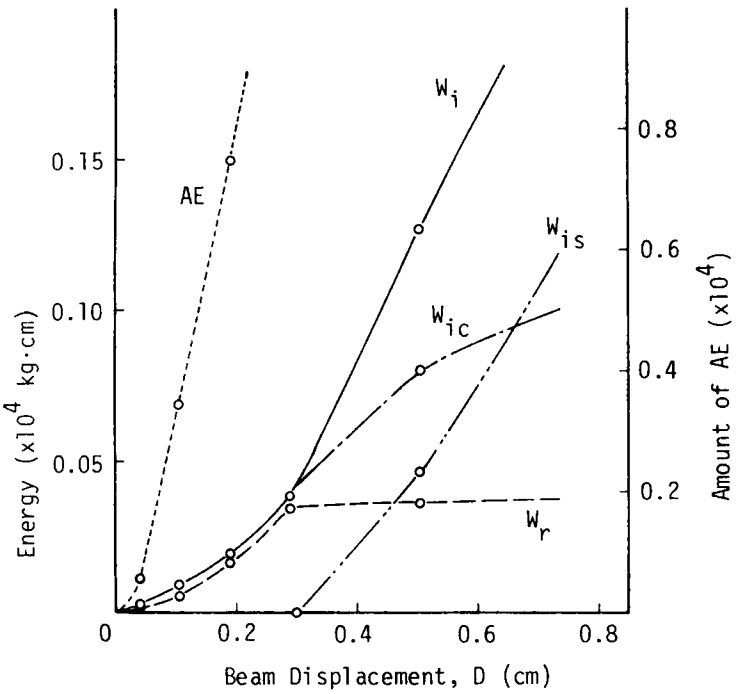

Fig. 5.17. Magnified Energy-Displacement Relationship of Beam B10.

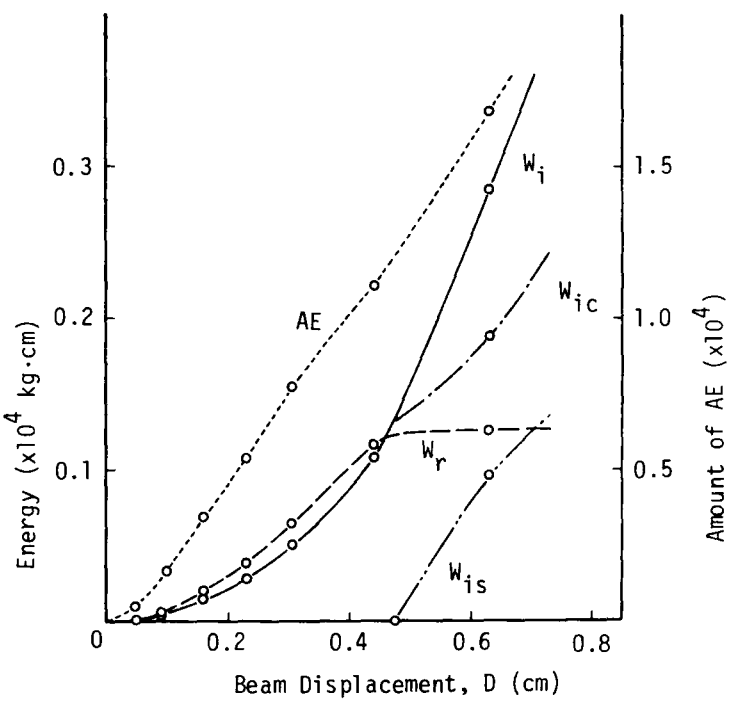

Fig. 5.18. Magnified Energy-Displacement Relationship of Beam B16.

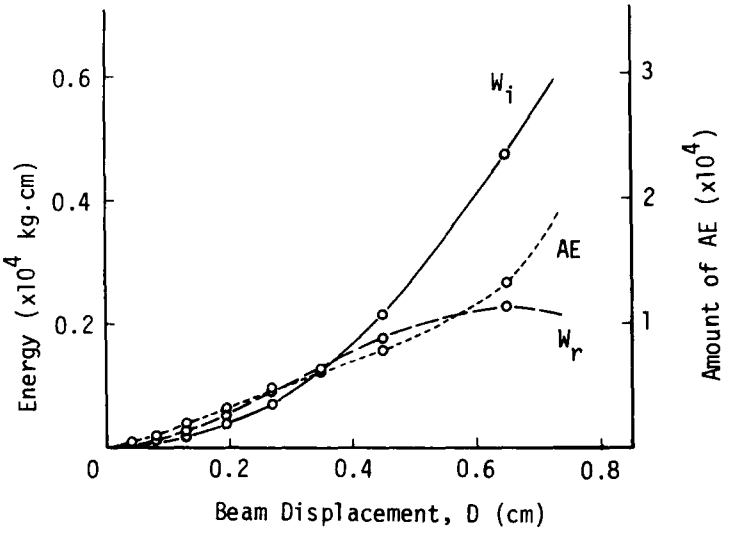

Fig. 5.19. Magnified Energy-Displacement Relationship of Beam B25.

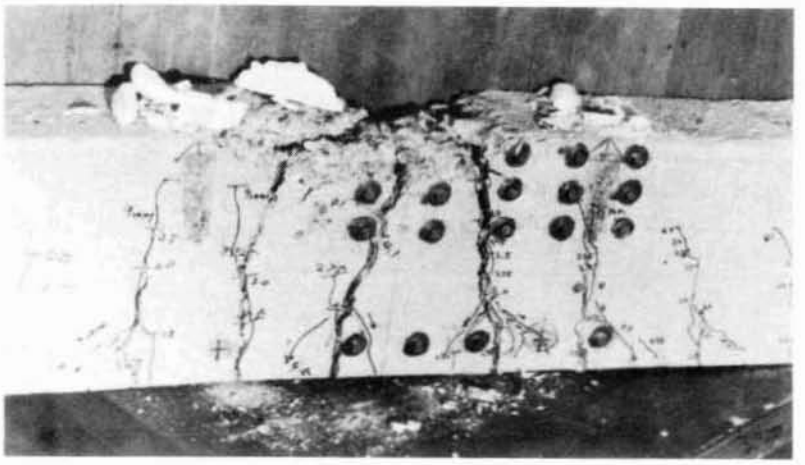

Fig. 5.20.
Beam B10.

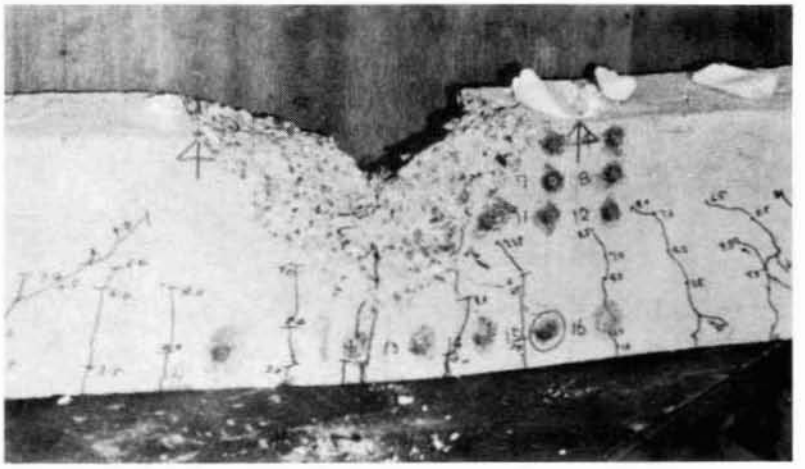

Fig. 5.21.
Beam B16.

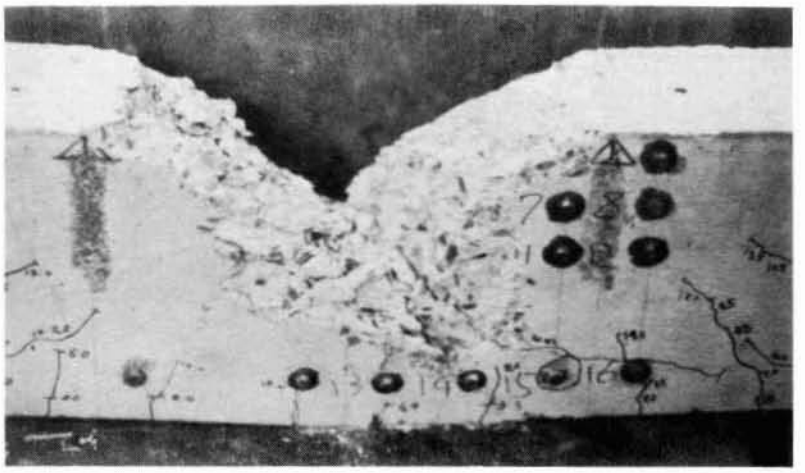

Fig. 5.22.
Beam B25.

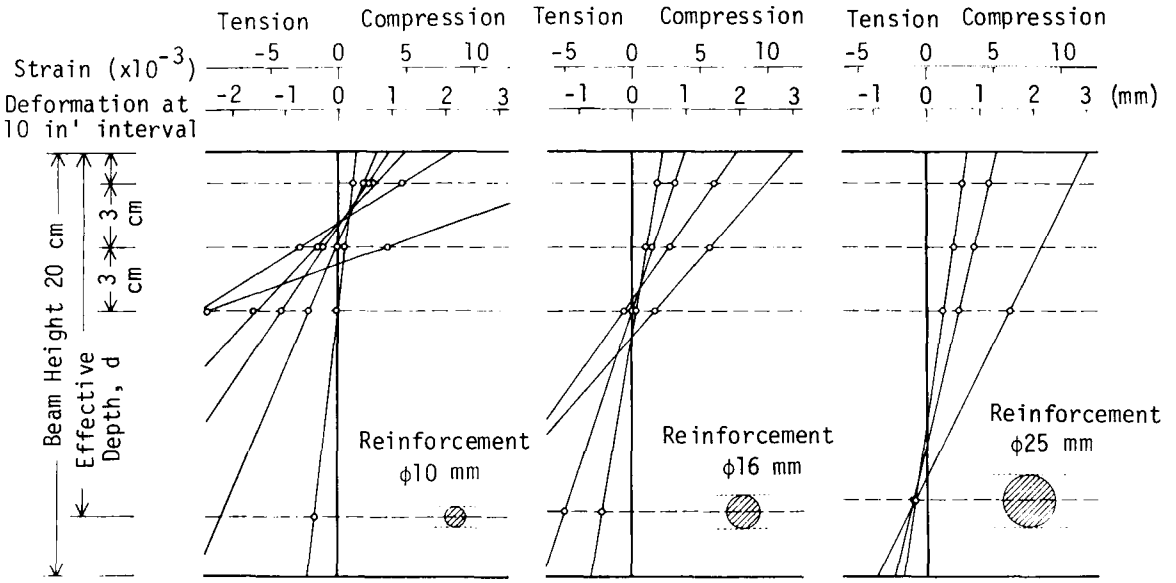

Fig. 5.23. Strain Distribution in Moment Span.

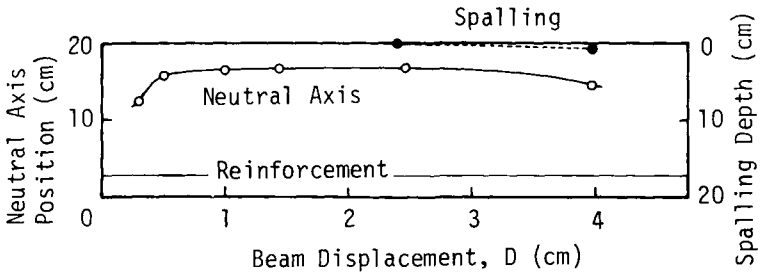

Fig. 5.24. Neutral Axis Position and Spalling of Beam B10.

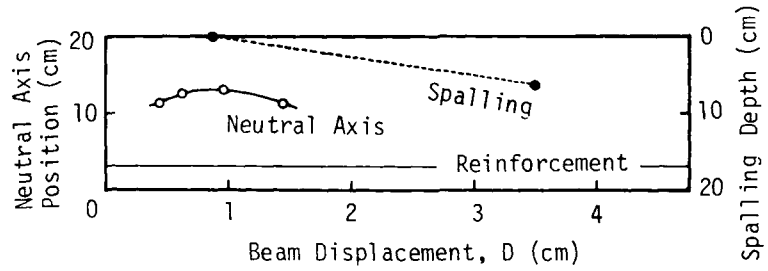

Fig. 5.25. Neutral Axis Position and Spalling of Beam B16.

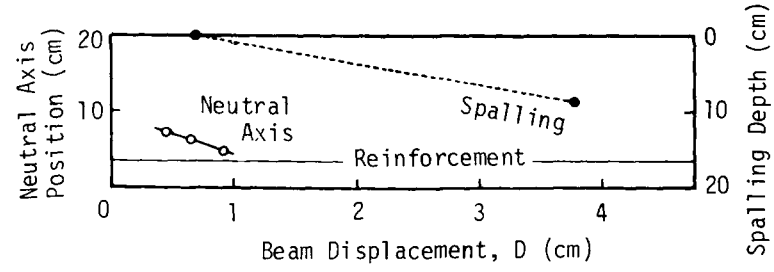

Fig. 5.26. Neutral Axis Position and Spalling of Beam B25.

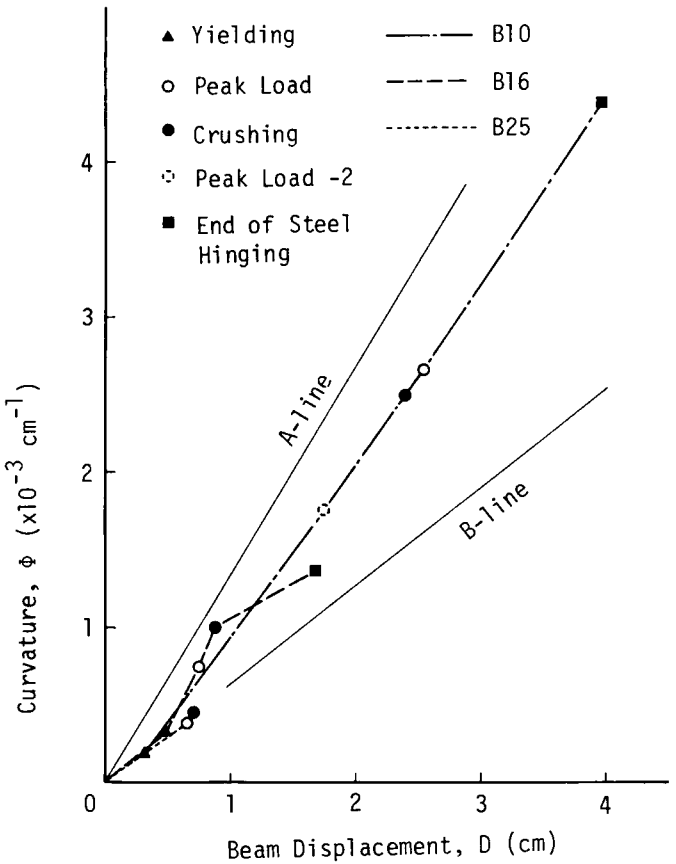

Fig. 5.27. Curvature and Beam Displacement.

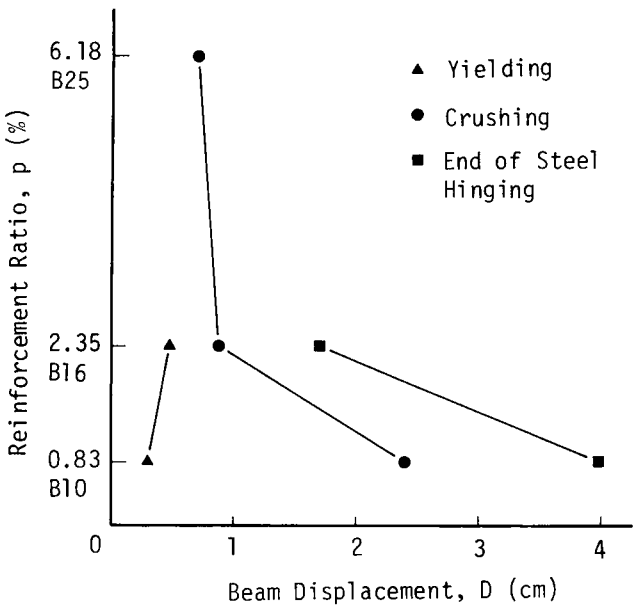

Fig. 5.28. Reinforcement Ratio and Beam Displacement.

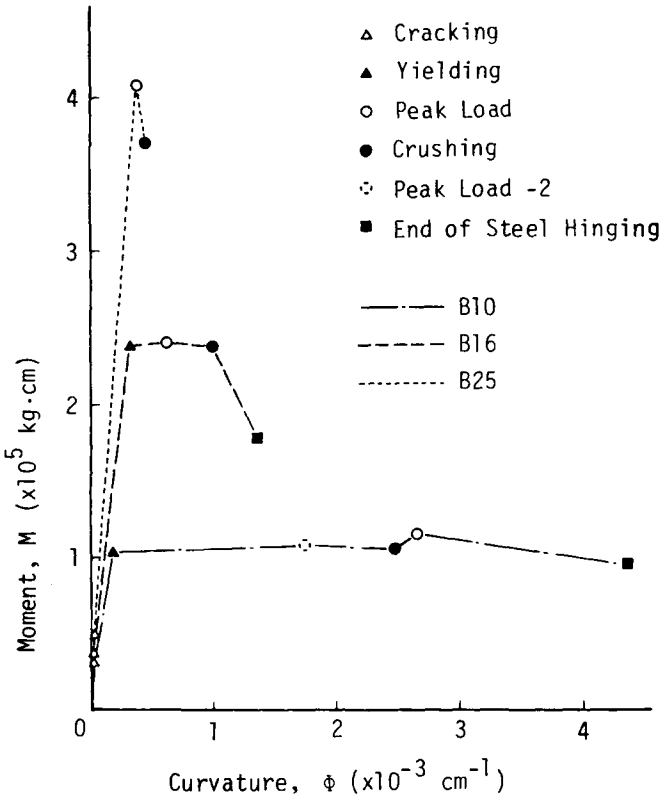

Fig. 5.29. Moment and Curvature.

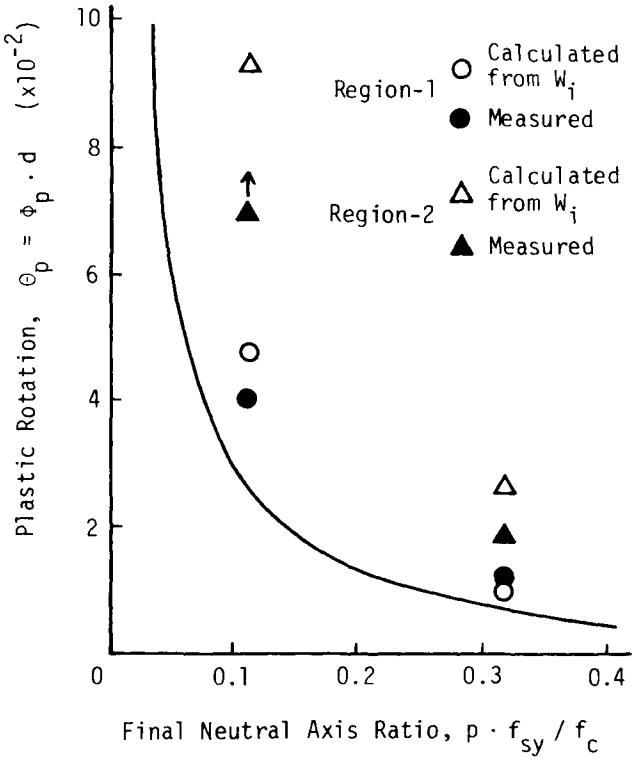

Fig. 5.30. Plastic Curvature and Final Neutral Axis Ratio.

CHAPTER 6. CONCLUSION

This investigation aims to propose and develop an energy approach for studying the failure process of concrete and concrete members.

In this thesis, the energy values calculated from load -displacement diagrams were used as parameters to indicate the change of internal structure in concrete and concrete members. The macroscopic failure process of the system was correlated to the changing process in the internal structure by using the energy transformation concept.

The energy transformation concept was applied to the flexural fracture process of concrete in Chapter 2. Then the concept was applied to the compressive fracture process of concrete in Chapter 4 and to the flexural failure process of RC beams in Chapter 5. Fracture toughness parameters were measured in Chapter 3 based on the results of Chapter 2.

The conclusions of each chapter are described at the end of that chapter. The main purposes and important results of each chapter are reviewed in this chapter. In addition, the advantages and problems of the energy approach to the failure process are discussed.

Chapter 2 describes the relationship between dissipated energy, crack length, and crack sources for concrete beams in flexure. The crack depth observed by dyeing the fracture surface was proportional to the dissipated energy, which was calculated from the load-displacement diagrams. Consequently, it seems obvious that the dissipated energy is an indicator of fracture, i.e. crack propagation, in concrete. Locations of crack sources obtained by AE detection coincided well with the observed fracture surface. This means that the dissipated

energy during the fracture was consumed in the neighborhood of the observed fracture surface. The main cracks in the flexural fracture process of concrete propagated remarkably after the peak load. This was supported by the experimental results of dissipated energy, dyed fracture surface, and AE detection.

Chapter 3 presents fracture toughness parameters of concrete calculated from beam specimens in flexure. The critical J-integral, J_c, was evaluated from the applied energy at the strength failure point. The unit dissipated energy, S, was evaluated from the total dissipated energy at complete rupture of the specimens. The unit dissipated energy, S, was about 4.5 times greater than the critical J-integral, J_c, for plain concrete. For the concrete containing 1% of steel fibers, J_c was 4 times greater than that of plain concrete, and S was 26 times greater, but K_c and G_c were almost constant for both plain and fiber reinforced concrete. Therefore, S, and to a lesser extent J_c, would be a better parameter than K_c or G_c for evaluating the effectiveness of steel fiber addition. The best procedure to evaluate the most meaningful and reproducible value of J_c was investigated. The most easily reproducible values of J_c were obtained from one-third depth notched beams by the R-method (explained in Section 3.2). J_c is considered to represent the ability to resist strength failure in flexure, and S the energy absorbing capacity in flexure.

In Chapter 4, the energy transformation concept was applied to the compressive fracture process of concrete, which seems more complicated than the flexural fracture process. The dissipated energy was divided into two components, W_{icr} and W_{ifr}. W_{icr} is the energy dissipated by

crack formation and W_{ifr} is the energy consumed by viscous friction and other types of dissipation. The effects of moisture content and loading rate on the mechanical behavior of concrete were examined. The energy transformation concept explains that the increase in compressive strength under a high loading rate is caused by the decrease of time-dependent deformation, also that the increase in compressive strength due to the decreased moisture content is caused by an increase in internal bond energy and frictional resistance. When concrete specimens are loaded repeatedly in high compression, the energy W_{icr} at the first repetition becomes larger as the moisture content of the concrete decreases. When the upper load limit in the repeated loading was about 90% of the compressive strength, the ratio of W_{icr} to W_i at the first repetition ranged from 0.54 to 0.80. This ratio depended on the moisture content in the concrete. The resistance ability to the strength failure and the energy absorbing capacity of concrete in compression were also discussed.

In Chapter 5, energy dissipation in the flexural failure process of reinforced concrete beams (RC beams) was related to ductile behavior. The role of the reinforcement and the concrete in energy dissipation was determined. As the reinforcement ratio increased, the energy dissipated in concrete, W_{ic}, increased and the energy dissipated in the reinforcement, W_{is}, decreased. After yield of the reinforcement, W_{is} increased with beam displacement. But W_{is} stopped increasing at a certain point, after which energy was dissipated only in the concrete. The results suggested that the plastic curvature or the energy dissipation between the initiation of reinforcement yielding and the end of energy

dissipation in the reinforcement would be a useful index to evaluate the plastic rotation capacity of the steel hinging.

In addition, it is hoped that the following investigations will be carried out to complete the work of this thesis. W_{icr} and W_{ifr} should be determined for other stages in the compressive fracture process and also for the flexural fracture process of concrete. The effect of specimen size on the capacity to resist strength failure and on the energy absorbing capacity in compression should be investigated. In order to make the investigation in Chapter 5 more conclusive, the critical point, where W_{is} stops increasing, should be examined using a greater variety of reinforcement ratios and a larger number of specimens. To ascertain the validity of using the J-integral method for fiber reinforced concrete, the initiation point of the main crack in the concrete must be observed by crack dyeing or AE detection.

As described above, some interesting knowledge of the failure phenomena of concrete and RC beams was obtained by using this energy approach. The merits of this approach are given as follows:

(a) The energies are calculated not from the stress-strain relationship but from the load-displacement relationship of a given system.
(b) The calculated energies quantitatively indicate the internal change within the system.
(c) There is no restriction on specimen size.
(d) This method is applicable to the failure of RC members as well as the fracture of concrete specimens.

In order to calculate reliable energy values, the

load-point displacement should be measured as exactly as possible. Attention should be paid to the seating effects at the supporting points and any deformation in the loading equipment. The displacement meter should also be easy to handle.

It is rather difficult to measure the displacement distribution corresponding to the distributed load. In such a case, the energy approach may need some modification.

In the future, if failure phenomena become well understood by further studies, it will be possible to more accurately predict not only the strength but also the location and manner of possible failures in a structure.

LIST OF REFERENCES

1. Dantu, P., "Etude des contraintes dans les milieux hétérogènes. Application au beton," Annales de l'institut Technique du Bâtiment et des Travaux Publics, 11-121, 1958.1 (55-77).
2. Griffith, A. A., "The phenomena of Rupture and Flow in Solids," Phil. Trans. Roy. Soc. London, A.221, 1921 (163-198).
3. Inglis, C. E., "Stresses in a Plate due to the Presence of Cracks and Sharp Corners," Trans. Inst. Naval Architects, London, V. LV, 1913 (219-230).
4. Westergaard, M. M., "Bearing Pressures and Cracks," Jour. Appl. Mech., 66, 1939 (A49-A53).
5. Irwin, G. R., "Analysis of Stress and Strain Near the End of Crack Traversing a Plate," Jour. Appl. Mech., 24, 1957 (361-364).
6. Paris, C. P. and Sih, G. C., "Stress Analysis of Cracks," Fracture Toughness Testing and Its Applications, STP 381, ASTM, 1965.
7. Orowan, E., "Fundamentals of Brittle Behavior in Metals," Massachusetts Institute of Technology Symposium, June 1950, John-Wiley, 1950.
8. Rice, J. R., "A Path Independent Integral and the Approximate Analysis of Strain Concentration by Notches and Cracks," Jour. Appl. Mech., 35, 1968.6 (379-386).
9. Begley, J. A. and Landes, J. D., "The J-integral as a Fracture Criterion," Fracture Toughness, STP 514, ASTM, 1972 (1-20).
10. Rice, J. R., Paris, P. C. and Merkle, J. G., "Some Further Aspects of J-integral Analysis and Estimates," Progress

in Flaw Growth and Fracture Toughness Testing, STP 536, ASTM, 1973 (231-245).

11. Kaplan, M. F., "Crack Propagation and the Fracture of Concrete," Jour. ACI, 58-5, 1961.11 (591-610).
12. Moavenzadeh, F. and Kuguel, R., "Fracture of Concrete," Jour. Materials, 1969 (497-519).
13. Kobayashi, A. S., "Experimental Techniques in Fracture Mechanics," SESA Monograph No. 1, SESA, 1973.
14. Kesler, C. E., Naus, D. J. and Lott, J. L., "Fracture Mechanics - Its Applicability to Concrete," Mechanical Behavior of Materials, 4, SMSJ, 1972 (113-124).
15. Mindess, S., Lawrence, F. V. and Kesler, C. E., "The J-integral as Fracture Criterion for Fiber Reinforced Concrete," Cem. and Con. Res., 7, 1977 (731-742).
16. Halvorsen, G. T., "Toughness of Portland Cement Concrete," Doctoral Thesis, Department of Civil Engineering, University of Illinois at Urbana-Champaign, 1979.
17. Kenny, P. and Campbell, J. D., "Fracture Toughness, an Examination of the Concept in Predicting the Failure of Materials," Progress in Mat. Sci., 13-3 (Ed. Chalmers, B. and Hume-Rothery, W.) Pergamon Press 1967.
18. Koyanagi, W., "Fracture of Concrete," Concrete Library, No.34, JSCE, 1972.10 (93-111) [in Japanese].
19. Hsu, T. T. C., Slate, F. O., Sturman, G. M. and Winter, G., "Microcracking of Plain Concrete and the Shape of the Stress-Strain Curve," Jour. ACI, 60-2, 1963.2 (209-224).
20. Robinson, G. S., "Methods of Detecting the Formation and Propagation of Microcracks in Concrete," The Structure of Concrete, Cem. and Con. Ass. 1968 (131-145).
21. Slate, F. O. and Olsefski, S., "X-rays for Study of

Internal Structure and Microcracking of Concrete," Jour. ACI, 60-5, 1963.5 (575-588).

22. Niwa, Y., Kobayashi, S., Koyanagi, W. and Nakagawa, K., "On Macro-Cracks and Strength Retention of Concrete Subjected to Three Axial Compression Load," Con. Jour. JANACC, 7-12, 1969.12 (24-31) [in Japanese].
23. Krishnaswamy, K. T., "Strength and Microcracking of Plain Concrete under Triaxial Compression," Jour. ACI, 65-10, 1968.10 (856-862).
24. Niwa, Y., Koyanagi, W. and Nakagawa, K., "Failure Processes of Concrete under Triaxial Compressive Stress," Proc. JSCE, No.185, 1971.1 (31-41) [in Japanese].
25. Kato, K., "Microcracks and Physical Properties of Plain Concrete," Proc. JSCE, No.188, 1971.4 (61-72) [in Japanese].
26. Koyanagi, W., Mentani, Y., Rokugo, K. and Kusakabe, F., "Development of Internal Submicrocracking of Concrete under Repeated and Sustained Loading," Review of the Twenty-eighth General Meeting, CAJ, 1974.5 (207-210) [in Japanese].
27. Rüsch, H., "Physikalische Fragen der Betonprüfung," Zement-Kalk-Gips, 12-1, 1959.1 (1-9).
28. Yokomichi, H., Ikeda, K. and Matsuoka, K., "Propagation of Elastic Waves at Cracking in Concrete," Cem. and Con., CAJ, No.212, 1964.10 (2-6) [in Japanese].
29. Yokomichi, H., Takata, Y. and Kakuta, Y., "Process of Crack Propagation in Concrete Beams," Review of the Twentieth General Meeting, CAJ, 1966.5 (402-405) [in Japanese].
30. Niwa, Y., Kobayashi, S. and Otsu, M., "Studies of Acoustic Emissions in Concrete Structures," Proc. JSCE, No.261, 1977.5 (101-112) [in Japanese].

31. Niwa, Y., Kobayashi, S. and Otsu, M., "Studies of Source Location by Acoustic Emission," Proc. JSCE, No. 276, 1978.8 (135-147) [in Japanese].
32. Knill, J. L., Franklin, J. A. and Malone, A. W., "A Study of Acoustic Emission from Stressed Rock," Int. Jour. Rock Mech. Min. Sci., 5, 1968.11 (87-121).
33. Nwokoye, D. N., "Prediction and Assessment of Concrete Properties from Pulse-velocity Tests," Mag. Con. Res., 25-82, 1973.3 (39-46).
34. Jones, R., "A method of Studying the Formation of Cracks in a Material Subjected to Stress," British Jour. Appl. Physics, 3-7, 1952.7 (229-232).
35. Jones, R. and Kaplan, M. F., "The Effect of Course Aggregate on the Mode of Failure of Concrete in Compression and Flexure," Mag. Con. Res., 9-26, 1957.8 (89-94).
36. Shar, S. P. and Chandra, S., "Critical Stress, Volume Change, and Microcracking of Concrete," Jour. ACI, 65-9, 1968.9 (770-781).
37. Niwa, Y. and Nakagawa, K., "On the Behavior of Concrete Mortar under Hydrostatic Pressure," Proc. JSCE, No. 185, 1971.1 (43-50) [in Japanese].
38. Spooner, D. C. and Dougill, J. W., "A Quantitative Assessment of Damage Sustained in Concrete during Compressive Loading," Mag. Con. Res., 27-92, 1975.9 (151-160).
39. Spooner, D. C., Pomeroy, C. D. and Dougill, J. W., "Damage and Energy Dissipation in Cement Pastes in Compression," Mag. Con. Res., 28-94, 1976.3 (21-29).
40. Ashbee, R. A., Heritage, C. A. R. and Jordan, R. W., "The Expanded Hysteresis Loop Method for Measuring the Damping Properties of Concrete," Mag. Con. Res., 28-96, 1976.9 (148-169).

41. Testa, R. B. and Stubbs. N., "Concrete Failure Related to Constituent Properties," Proc. ASCE, 102-EM3, 1976.6 (515-529).
42. Phipps, M. E., "The Strain Capacity of Compression-zone Concrete Subjected to Short-term Loading," Mag. Con. Res., 28-95, 1976.6 (85-100).
43. Okada, K., Koyanagi, W. and Rokugo, K., "Energy Approach to the Fracture Process of Concrete in Compression Related to Its Water Content," Proc. JSCE, No.248, 1976.4 (129-136) [in Japanese].
44. Okada, K., Koyanagi, W. and Rokugo, K., "Fracture Process of Concrete in Compression," Proc. 2nd Int. Conf. Mech. Behav., Boston, 1976.8 (1358-1362).
45. Okada, K., Koyanagi, W. and Rokugo, K., "Energy Approach to the Fracture Process of Concrete in Flexure," Proc. JSCE, No.285, 1979.5 (109-119) [in Japanese].
46. Okada, K., Koyanagi, W. and Rokugo, K., "A Study on the Energy Dissipation in Flexural Failure Process of Reinforced Concrete Beams," Submitted to Proc. JSCE [in Japanese].
47. Nishimatsu, Y., Matsuki, K. and Koizumi, S., "The Failure Process of Rock in Compression," Jour. SMSJ, 23-248, 1974.5 (374-379) [in Japanese].
48. Kaiser. J., "Knowledge and Research on Noise Measurements during the Tensile Stressing of Metals," Arkiv. fur Eisenhuttenwesen, 24-43, 1953.
49. Niwa, Y., Koyanagi, W. and Kobayashi, S., "Failure Criterion of Lightweight Concrete Subjected to Triaxial Compression," Trans. JSCE, No.143, 1967.7 (28-35) [in Japanese].
50. Kobayashi, S. and Koyanagi, W., "Failure Criterion of

Concrete Subjected to Multi-Axial Compression," Jour. SMSJ, 16-170, 1967.11 (897-902) [in Japanese].

51. Zaverl, F. Jr., "The Influence of Specimen Dimensions on a J_m Fracture Toughness Test," Report No.394, Department of Theoretical and Applied Mechanics, University of Illinois at Urbana-Champaign, 1974.

52. Mattock, A. H., Kriz, L. B. and Hognestad, E., "Rectangular Concrete Stress Distribution in Ultimate Strength Design," Jour. ACI, 32-8, 1961.2 (875-928).

53. Yamada, M., "Drehfähigkeit Plastischer Gelenke in Stahlbeton Balken," Beton ud. Stahlbau, 27-4, 1958.4 (85-91).

54. Koyanagi, W., "Plastic Hinging in Concrete Members," Con. Jour. JCI, 15-5, 1977.5 (1-10) [in Japanese].

ACI: American Concrete Institute
ASCE: The American Society of Civil Engineers
ASTM: American Society for Testing and Materials
CAJ: The Cement Association of Japan
JANACC: Japan National Council on Concrete
JSCE: The Japan Society of Civil Engineers
SESA: Society for Experimental Stress Analysis
SMSJ: The Society of Materials Science, Japan